DESIGN AND THEORETICAL STUDY OF WURTZITE III-N DEEP ULTRAVIOLET EDGE EMITTING LASER DIODES

A Ph.D Dissertation
Presented to
The Academic Faculty

by

Md. Mahbub Satter

In Partial Fulfillment
of the Requirements for the Degree
Doctor of Philosophy in the
School of Electrical and Computer Engineering

Georgia Institute of Technology
December 2014

Copyright © 2014 by Md. Mahbub Satter

DESIGN AND THEORETICAL STUDY OF WURTZITE III-N DEEP ULTRAVIOLET EDGE EMITTING LASER DIODES

Approved by:

Dr. Douglas P. Yoder, Advisor
School of Electrical and Computer Engineering
Georgia Institute of Technology

Dr. John A. Buck
School of Electrical and Computer Engineering
Georgia Institute of Technology

Dr. Russell D. Dupuis
School of Electrical and Computer Engineering
Georgia Institute of Technology

Dr. Eric M. Vogel
School of Materials Science and Engineering
Georgia Institute of Technology

Dr. Shyh-Chiang Shen
School of Electrical and Computer Engineering
Georgia Institute of Technology

Date Approved: October 08, 2014

To my family

ACKNOWLEDGEMENTS

First of all, I would like to say that I am grateful to my adviser Professor Douglas Yoder for hiring me as a graduate research assistant and giving me the opportunity to study at Georgia Institute of Technology, one of the premier engineering schools in the US. I would like to thank him for giving me the opportunity to work in the exciting field of computational electronics and photonics. This PhD research would not have come this far without his guidance, encouragement and support. I would like to express my gratitude to my doctoral examination committee members Professor Russell Dupuis, Professor Shyh-Chiang Shen, Professor John Buck and Professor Eric Vogel for taking time out of their busy schedule to review my dissertation draft and providing valuable comments and suggestions.

I am grateful to the Defense Advanced Research Projects Agency (DARPA) for sponsoring my Ph.D. research and special thanks to Professor Dupuis and Professor Shen for the opportunity to collaborate on the Compact Mid-Ultraviolet Technology (CMUVT) project. I would like to extend my appreciation to the colleagues and fellow graduate students in the Advanced Materials and Devices Group (AMDG) and Semiconductor Research Laboratory (SRL) especially to Professor Jae-Hyun Ryou, Dr. Zachary Lochner, Dr. Jeomoh Kim, Yuh-Shiuan Liu (Kevin), Xiaohang Li and Tsung-Ting Kao (Louis) for all the technical discussions and cooperation. Thank you for being such wonderful team players.

When I first came to the US back in Fall 2009 to start my Ph.D., I got a lot of support from a number of generous people who helped me to settle in and get up to the speed. Thanks to Dr. Sriraaman Sridharan, Dr. Fahad Mohammed, Benjamin Connors, Dr. Shayok Mukhopadhyay, Udit Gupta, Xiufeng Yang and Zhenhua Xie for all the help.

I really enjoyed all the social and cultural activities organized by Bangladesh Student Association at Georgia Tech (GTBSA). Thank you for all the good memories.

Finally, I would like to thank my parents and all other family members for their love, encouragement and continued support. I am indebted to my beloved wife, Munmun Islam, for her inspiration and support through all these years of my graduate life. I applaud her for getting an MS in ECE from Georgia Tech despite all the challenges.

TABLE OF CONTENTS

LIST OF TABLES

Page

LIST OF FIGURES

Page

LIST OF ABBREVIATIONS

CW	Continuous wave
DUV	Deep ultraviolet
EBL	Electron blocking layer
FCA	Free carrier absorption
HH	Heavy-hole
LCI	Lateral current injection
LD	Laser diode
LED	Light-emitting diode
MQW	Multiple quantum well
PL	Photoluminescence
QCSE	Quantum-confined Stark effect
QW	Quantum well
QWB	Quantum well barrier
SPSL	Short-period superlattices
SQW	Single quantum well
SRH	Shockley-Read-Hall
TE	Transverse electric
TM	Transverse magnetic
UV	Ultraviolet

SUMMARY

Designs for deep ultraviolet (DUV) edge emitting laser diodes (LDs) based on the wurtzite III-nitride (III-N) material system are presented. A combination of proprietary and commercial advanced semiconductor LD simulation software is used to study the operation of III-N based DUV LDs theoretically. Critical factors limiting device performance are identified based on an extensive literature survey. A comprehensive design parameter space is investigated thoroughly with the help of advanced scripting capabilities. Several design strategies are proposed to eliminate the critical problems completely or partially.

A DUV LD design is proposed based exclusively on AlInN active layers grown epitaxially on bulk AlN substrates. AlInN offers a promising alternative to AlGaN for the realization of LDs and LEDs operating in the DUV regime. The proposed AlInN-based design also features a tapered electron blocking layer (EBL) instead of a homogeneous one. Homogeneous EBL layers induce a parasitic inversion layer sheet charge at the spacer/EBL interface and therefore, degrade the optical gain. Tapered EBLs redistribute the interfacial polarization charge volumetrically throughout the entire EBL thickness via compositional grading, and eliminate the parasitic inversion layer charge.

At present, it may be difficult to grow AlInN epitaxially with superior crystalline quality because of the disparity in the optimum growth temperature between AlN and InN. But the issue does not appear to be fundamental. As a consequence, AlGaN based DUV LD designs are explored also. Polarization charge matching is proposed to improve electron and hole wavefunction overlap within the active region. Numerical simulation predicts significant improvement in threshold current and slope efficiency as quaternary AlInGaN barriers are chosen judiciously to minimize net polarization charge at the barrier/well interfaces. Although the strategy of polarization charge matching has already

been proposed in the literature to enhance performance of visible wavelength LEDs and LDs, the proposed design presents the first demonstration that polarization charge matching is also feasible for DUV LDs operating at sub-300 nm wavelengths.

A lateral current injection (LCI) LD design is proposed featuring polarization-charge-matched barriers and regrown Ohmic contacts to avoid a group of issues related to the highly inefficient p-type doping of wide bandgap III-N materials in vertical injection designs. The proposed design partially decouples the problem of electrical injection from that of optical confinement. Numerical simulations reveal that regrown Ohmic contacts not only eliminate artificial blocking layers for lateral charge transport, but prevent the leakage of carriers from the active region. The idea of an LCI LD design is not new, rather it has been proposed in the literature in the 90s to be used as longer wavelength active sources in optoelectronic integrated circuits using GaInAsP/InP and related material systems. Nevertheless, the proposed design is the first theoretical demonstration that this concept can be applied to DUV LDs based on III-N material system.

To solve the problem of hole transport in vertical injection designs, a DUV LD design based exclusively on AlGaN material system is presented, featuring an inverse-tapered p-waveguide layer instead of an EBL. Spatial balancing of the lasing mode to minimize optical loss in the p-Ohmic metallization is achieved through the use of a narrow bandgap yet transparent n-waveguide layer. Several EBL designs are investigated, and compared with conventionally-tapered EBL design. Through judicious volumetric redistribution of fixed negative polarization charge, inverse tapering may be exploited to achieve nearly flat valence band profiles free from barriers to hole injection into the active region, in contrast to conventional designs. Furthermore, proper selection of quantum well barrier and spacer compositions are demonstrated to reduce electron leakage from the active region. Numerical simulations demonstrate that the inverse tapered strategy is a viable solution for efficient hole injection in vertical injection DUV LDs operating at shorter wavelengths (< 290 nm).

CHAPTER 1

INTRODUCTION

1.1 Motivation and Objective

The motivation for this Ph.D. research comes from the consumer and military demand to explore alternatives to large, toxic, low-efficiency gas lasers and mercury lamps as deep ultraviolet (DUV) light emitters for a number of potential applications. The objective of this research is to design DUV edge emitting laser diodes (LDs) based on the wurtzite III-N material system. A combination of proprietary and commercial advanced semiconductor LD simulation software will be used to study the operation of III-N based DUV LDs theoretically. Critical factors limiting device performance will be identified, elucidated and strategies will be proposed for design optimization. This is not a simulation tool development dissertation. Rather, principles of semiconductor physics, photonics, quantum mechanics, as well as insight into numerical techniques and algorithms will be used to generate robust designs that will not only be able to circumvent all the critical issues, but also be feasible with the current growth technology.

1.2 Organization

The dissertation is organized as follows: A brief description of the critical issues associated with the design of DUV LDs is reviewed in Chapter 2 along with a brief assessment of the efforts made by other researchers to date to solve them. Chapter 3 describes briefly the simulation model used in the dissertation. An AlInN based DUV LD design is presented in Chapter 4 featuring a tapered EBL design to suppress the parasitic inversion layer charge. Chapter 5 explores the idea of polarization charge matching for an AlGaN based DUV LD design, followed by a sensitivity analysis for the systematically

selected charge-matched quaternary compositions. Chapter 6 introduces an AlGaN based lateral current injection DUV LD design that partially decouples the problem of electrical injection from that of optical confinement. In Chapter 7, the potential energy barrier associated with conventionally tapered EBL designs is identified as a significant impediment to efficient hole injection. An inverse tapered p-waveguide layer has been proposed as an alternative to the EBL along with an asymmetric waveguide design to achieve superior hole injection and to minimize the optical absorption loss, respectively. Finally, the dissertation concludes in Chapter 8 with a summary of the research conducted and a discussion of the possible future design strategies.

1.3 III-nitride Based UV Light Emitters

UV light emitters are very important for a number of applications including bio-agent detection [1], water and air purification [2], dermatology [3], high-density optical storage [4], critical communications [5], currency screening [6], and photolithography [7]. Recently, UV LDs and light-emitting diodes (LEDs) have attracted considerable interest as promising alternatives to large, toxic, low-efficiency gas lasers and mercury lamps. The UV spectrum is typically divided into four bands: UV-AI (340-400 nm), UV-AII (320-340 nm), UV-B (280-320 nm), and UV-C (< 280 nm). From a theoretical viewpoint, UV LDs and LEDs based on group-III-nitrides (III-Ns) may emit light at wavelengths in the entire UV-A and -B bands as well as penetrating deep into the UV-C band [8]. Moreover, III-N materials (AlN, GaN and InN and their related ternaries and quaternaries) have some appealing features, such as wide bandgap, high electron saturation drift velocity, high electric field strength, high thermal conductivity, and the ability to form pseudomorphic heterostructure. Until now, AlGaN and AlInGaN based UV LEDs have made significant progress [9-20]. Operation of III-N LEDs has already been demonstrated at the shortest possible wavelength of 210 nm [21]. Apart from the

demonstration of optically pumped stimulated emission in the deep ultraviolet (DUV) range [22-24], the promise of III-N LDs remains largely unfulfilled. Several groups have reported near-UV LDs based on the AlInGaN material system, grown on sapphire or GaN substrates [25-28]. Reported emission wavelengths span a range between 350 to 366 nm. At the time of this writing, 336 nm is the shortest emission wavelength reported for III-N LDs [29]. Unfortunately, the performance of UV LDs grown on GaN substrates is still inferior to their longer wavelength counterparts operating in the visible spectrum.

Several practical issues complicate the design of an epitaxial structure for DUV LDs and place limitations on realizable device performance matrices. Prevalent UV LD designs based on GaN substrates may not ultimately be successful for short wavelength emission in the UV-C band because of the requirement for extremely high Al mole fraction (> 40%) in the active region [8]. Although bulk AlN substrates are one of the most favorable candidates for the growth of UV LDs to emit in the UV-B and -C bands, availability of high quality AlN substrates is at present limited. Spontaneous and piezoelectric polarization charges of wurtzite III-N materials are well-known to induce large built-in electric fields inside the active region that cause a spatial separation of electron and hole wavefunctions within quantum-wells (QWs) and lower the electroluminescence efficiency [30]. Conventional LD designs employing homogeneous electron blocking layers (EBLs) suffer optical gain degradation attributable to a parasitic inversion layer charge, which forms as a result of the polarization charge associated with homogeneous EBLs [30]. They also introduce undesired hole blocking layers in the p-side and limit hole injection into the active region by inefficient thermionic emission [31]. The low conductivity of p-type wide bandgap III-N materials is one of the most critical design bottlenecks. The situation worsens approaching shorter wavelengths because of the higher activation energy of Mg dopants. Apart from greater Joule heating in the p-type layers, unscreened polarization charge at the waveguide/ EBL interface may give rise to an artificial hole blocking layer, exacerbating the problem of hole injection.

Although narrow bandgap III-N materials exhibit superior p-type conductivity, their use as p-waveguide layers may shift the optical mode profile toward the p-type layers. This strategy tends to reduce optical confinement factor and introduce optical absorption loss in the p-type layers and in the highly lossy Ohmic metallization for p-contact. These p-type conductivity considerations make it very difficult to design optical waveguides that maintain the optical mode profile centered on the active region. A deeper understanding of all the critical issues associated with the III-N based DUV LD designs may provide solutions to these challenges, enabling the design of optimized epitaxial structures that would be feasible with current growth technology.

CHAPTER 2

OVERVIEW OF THE CRITICAL ISSUES COMPLICATING DUV LD DESIGNS

There are several challenges that need to be overcome to realize practical LDs operating in the UV-B and -C bands. This chapter briefly explains the origin and consequences of these issues. Literature is reviewed also in the context of these problems. Though a set of these issues may also exist in the longer wavelength designs (near-UV and visible spectrum), some problems are specific to the DUV wavelength designs only. Various design strategies are proposed in the literature to solve these problems.

2.1 GaN Based Template

Several groups have reported near-UV LDs based on the AlInGaN material system, grown on sapphire or GaN substrates [25-28]. The performance of UV LDs grown on GaN substrates is still inferior to their longer-wavelength counterparts because of the lattice mismatch between AlGaN alloys used in the active region and GaN. For a given $Al_xGa_{1-x}N$ composition having an equilibrium lattice constant $a(x)$, the basal strain $\eta(x)$ for the epitaxial layer grown pseudomorphically on a GaN substrate is defined by the equation (2.1):

$$\eta(x) = \frac{a^{GaN} - a(x)}{a(x)} \tag{2.1}$$

In the case of AlGaN, extended defects are formed in the epitaxial layers due to biaxial tensile strain, a problem which is aggravated at higher aluminum (Al) mole fraction. Defects inside the active regions are known to degrade electroluminescence efficiency by

non-radiative recombination processes [32]. The dominant non-radiative recombination processes are thought to be Shockley-Read-Hall (SRH) and Auger recombination. The rate of SRH recombination can be expressed [33] by the equation (2.2):

$$R_{net}^{SRH} = \frac{np - n_i^2}{\tau_p(n+n_1)+\tau_n(p+p_1)} \tag{2.2}$$

where n and p are the concentrations of electrons and holes respectively, n_i is the intrinsic carrier concentration, τ_n and τ_p are electron and hole lifetimes respectively (depend on trap densities), n_1 and p_1 are parameters that introduce the effects of the trap energy levels. The Auger recombination rate can be modeled [33] by the equation (2.3):

$$R_{net}^{AU} = \left(c_n^{AU} n + c_p^{AU} p\right)(np - n_i^2) \tag{2.3}$$

Here, c_n^{AU} and c_p^{AU} are capture coefficients for electron and hole respectively. High defect density will lower SRH lifetimes. Different growth strategies are reported to reduce the density of defects. Schematic illustrations for two such strategies are shown in Figure 2.1. The density of threading dislocations induced by lattice mismatch may be reduced using grooved AlGaN/AlN underlying layers [34]. LDs have also been reported with indium (In)-free AlGaN active layers emitting in the UV-AII band [29], in which hetero-facet-controlled epitaxial lateral overgrowth has been employed. Notwithstanding the limited improvements achieved via special growth techniques, UV LD designs on GaN substrates may not ultimately be successful for short wavelength emission in the UV-C band due to various technological limitations, not least of which is the requirement for extremely high (> 40%) Al mole fraction in the active region [8]. Figure 2.2 shows the compositional dependence of the bandgap equivalent emission wavelength for the ternary AlGaN alloys along with the bandgap energy and a-axis lattice constant.

The growth of AlGaN active layers on a crack-free, thick, high-quality, high-Al-content AlGaN underlying layer is a precondition for satisfactory yield, reliability and performance [34]. It will be very difficult to ensure high-quality growth if sapphire or GaN substrates are employed. Although bulk AlN substrates are one of the most favorable candidates for the growth of UV LDs to emit in the UV-B and -C bands, availability of high-quality AlN substrates is at present limited [35]. CrystAl-N, Hexatech, and Nitride Crystals are the names of a few companies shipping AlN substrates

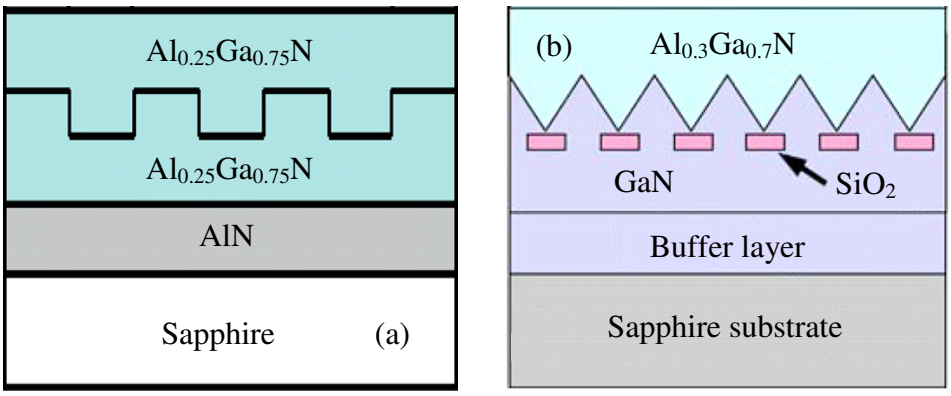

Figure 2.1: Different growth strategies are reported to reduce the defect density in epitaxially grown III-N layers. (a) Grooved AlGaN/AlN underlying layers [34] and (b) AlGaN layer grown using hetero-facet-controlled epitaxial lateral overgrowth method [29].

on a commercial basis. Compared to today's readily available sapphire or GaN substrates, AlN substrates are very expensive also. AlN based templates grown on foreign substrates such as Si [36], SiC [37], and sapphire [38] have also been reported. These templates usually have higher dislocation density, high surface roughness, and may require expensive growth techniques to compensate for the thermal expansion coefficient and lattice mismatch between the template and the foreign substrate.

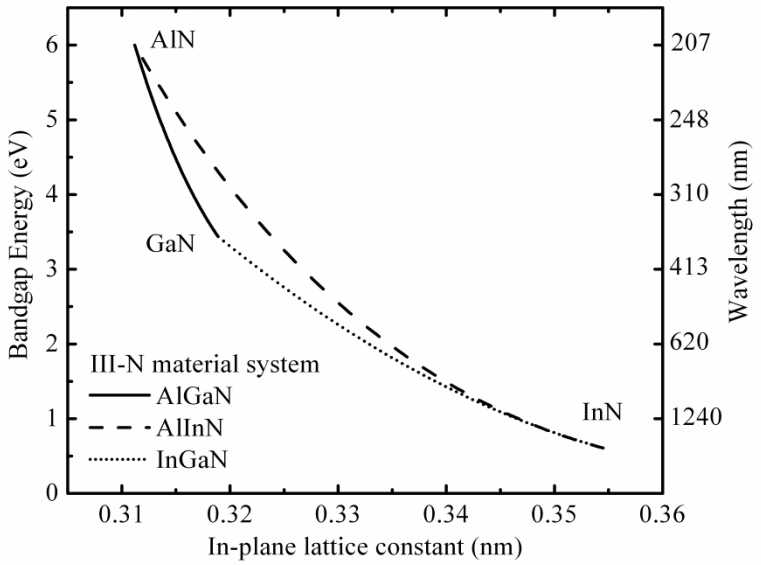

Figure 2.2: Lattice constant, bandgap energy and its equivalent emission wavelength for ternary AlGaN compositions [8].

2.2 Spontaneous and Piezoelectric Polarization Charge

The polar nature of wurtzite III-N materials introduces polarization charges at the interface of heterojunctions [8]. Both spontaneous and piezoelectric polarization charges contribute to the total interface polarization charge. Spontaneous polarization charge arises from the asymmetric bonding in the equilibrium wurtzite crystal structure. Lattice mismatch strain induces the piezoelectric part of the polarization charge. Table 2.1 lists the spontaneous and piezoelectric polarization charges of AlN, GaN and InN. Though high electron mobility transistors utilize the polar nature of III-N materials to achieve high drive current, polarization charges usually degrade the overall performance of III-N LDs and LEDs. Net interface polarization charge is well-known to induce large built-in electric field inside the active regions. This built-in electric field reduces the overlap

between electron and hole wavefunctions within the QWs and degrades electroluminescence efficiency.

Table 2.1: Spontaneous (P_{sp}) and Piezoelectric (P_{pz}) polarization charges of binary III-N materials [8]. Polar *c*-axis growth is assumed.

Material	Polarization Charge	
	P_{sp} (Cm^{-2})	P_{pz} (Cm^{-2})
AlN	-0.0898	$-1.808\eta + 5.624\eta^2$ for $\eta < 0$ $-1.808\eta - 7.888\eta^2$ for $\eta > 0$
GaN	-0.0339	$-0.918\eta + 9.541\eta^2$
InN	-0.0413	$-1.373\eta + 7.559\eta^2$

* η = basal strain.

So far, different methods have been proposed to improve the wavefunction overlap, and to eliminate completely or partially the related quantum-confined Stark effect (QCSE) [30]. Heavily doped quantum-well barriers (QWBs) have been proposed to facilitate the screening of polarization charge by free charge carriers [39]. Unfortunately, this strategy may increase the free carrier absorption (FCA) losses significantly [40]. The FCA loss, L_{FCA} can be expressed by the equation (2.4):

$$L_{FCA} = \iint (\alpha_n n + \alpha_p p)|\Psi|^2 dxdy \qquad (2.4)$$

where Ψ is the optical field, α_n and α_p are the FCA loss coefficients for electrons and holes respectively. To minimize QCSE and improve electron and hole wavefunction overlap, growth of non-polar and semi-polar epitaxial structures has been proposed and

demonstrated [41, 42]. Growth of III-N epitaxial structures on non-polar or semi-polar planes may incur poor crystalline quality [40], and may not be a cost-effective solution [43] to suppress wavefunction separation and QCSE. Several studies have reported a reduction in electron-hole wavefunction separation within QWs using modified electrostatic potential profiles [44]. Among the suggested approaches are an embedded wide bandgap delta-layer [45], a narrow bandgap delta-layer [46], a staggered QW profile [47], and graded QW profile [48], to name just a few. Implementation of these strategies may be difficult in the sub-nanometer range because of technological limitations. One easy way to reduce QCSE and the spatial separation of wavefunctions is to decrease the mole composition contrast between the QW and QWB [49, 50]. However, this approach limits QW depth in the conduction and valence bands, and may suffer from poor internal quantum efficiency because of inefficient capture of injected carriers. The net capture rate for electrons injected into the QW can be approximated [51] by the equation (2.5):

$$R_{Cap} = \left(1 - e^{\left(\frac{\mu_{2D} - \mu_{3D}}{k_B T}\right)}\right)\left(1 - \frac{n_{2D}}{N_{2D}}\right)\frac{n_{3D}}{\tau} \tag{2.5}$$

where $\mu_{2D(3D)}$ is the chemical potential for electrons in the bound states (continuum states), $n_{2D(3D)}$ is the bound (continuum) electron density, N_{2D} is the summation of all the bound states within the QW per unit volume, τ is the capture time representing carrier-carrier and carrier-optical phonon scattering processes, k_B is the Boltzmann constant, and T is the temperature. For deeper QWs, N_{2D} becomes greater than n_{2D} significantly. Thinner QWs [52, 53] may improve the spatial overlap between captured quasi-bound electron and hole populations, but only at the cost of a reduction in capture efficiency and a reduction in optical confinement factor. For ridge-shaped MQW LD structures, optical confinement factor, Γ can be expressed [54] by the equation (2.6):

$$\Gamma = \frac{\int_{-\frac{W}{2}}^{\frac{W}{2}} \int_{-\frac{t}{2}}^{\frac{t}{2}} |\Psi|^2 dxdy}{\iint |\Psi|^2 dxdy} \tag{2.6}$$

where W is the width of the mesa and t is the total thickness of the MQW layers.

The polar properties of AlN, GaN and InN are different from one another (see Table 2.1). Their difference can be leveraged to help suppress QCSE. Judiciously chosen quaternary AlInGaN materials can completely (or partially) minimize the net interface polarization charge within the active region and enhance electron-hole wavefunction overlap in LEDs and LDs by polarization charge matching [40, 55-57]. Though the use of polarization-charge-matched quaternaries has already been proposed in the literature to improve performance of visible wavelength LEDs and LDs, this charge matching concept is yet to be extended to the DUV LDs operating in the UV-C band. Our ability to grow a polarization charge minimized (or free) active region depends on how precisely we can control the composition of AlInGaN quaternaries. It has been reported that growth of high crystalline quality AlInGaN layers is difficult [58], though such issues do not appear to be fundamental. Recently, Sakalauskas *et al.* have grown a wide range of AlInGaN materials on *c*-plane sapphire substrates with GaN templates [59] and studied their optical properties. They confirmed pseudomorphic growth of AlInGaN films by high-resolution x-ray diffraction measurements. Experimental studies like this inspire confidence in the prospect of realizing polarization charge minimized active regions for DUV LDs using appropriately chosen quaternary AlInGaN compositions.

2.3 Homogeneous EBL Design

The purpose of EBLs in an LD epitaxial structure is to prevent the leakage of electrons from the active region. Within the QWs, captured electrons have a tendency to

escape because of their small effective mass. Wide bandgap materials are employed for EBLs and they are placed on top of the active region in so-called "p-up" designs. In the absence of EBLs, electrons injected from the n-side may reach deep into the p-side where they may recombine non-radiatively. The conduction band offset of the EBL tends to block the flow of escaping electrons and thus, improve the electroluminescence efficiency by reducing non-radiative recombination in the quasi-neutral p-type material above the active region. This fact is most easily appreciated, at least qualitatively, through examination of an analytic formula for thermionic emission current. The thermionic emission current across a heterojunction (flowing from narrow bandgap to wide bandgap) can be expressed [60] by the equation (2.7):

$$j_{therm} = A^* T_c^2 e^{\left(\frac{E_{F,n}^{NB} - E_c^{NB} - |\Delta E_c|}{k_B T_c}\right)} \tag{2.7}$$

where A^* is the effective Richardson constant, T_c is the temperature of the carriers, $E_{F,n}^{NB}$ and E_c^{NB} are the quasi-Fermi level for electrons and the conduction band energy level in the narrow bandgap material, respectively and ΔE_c is the conduction band offset at the heterojunction. Thermionic emission current decreases exponentially with the barrier height.

Unfortunately, the interface polarization charge associated with the III-N homogeneous EBLs plunges the conduction energy downward relative to the electron quasi-Fermi level at the spacer/EBL interface [40] and may also lead to a parasitic inversion layer in the p-type spacer materials [30]. Due to the influence of non-radiative recombination processes, the formation of this parasitic inversion layer leads to a reduction in optical gain. Furthermore, homogeneous EBLs also give rise to undesirable hole blocking layers on the p-side [31, 61], exacerbating the problem of hole injection. If the bandgap energy of EBLs is widened with the intention of blocking more electrons,

the overall situation becomes aggravated because more polarization charges are introduced at the EBL/spacer interface.

To solve these issues, compositionally graded EBLs are proposed in the literature [30, 62-68] instead of homogeneous EBLs. Compositional grading redistributes the interfacial polarization charge over the entire volume of the EBL layer, suppressing the formation of any parasitic well at the EBL/spacer interface. Polarization charge matching has also been proposed to eliminate the interface charges at the EBL/spacer interface. For instance, lattice-matched ternary [69] and polarization-charge-matched quaternary [70] homogeneous EBLs are reported to improve the overall performance of visible and near-UV LEDs. Several authors have reported short-period superlattices (SPSL) based EBLs [71, 72] to improve hole injection efficiency and electrical confinement of electrons. Although this strategy effectively reduces hole blocking barrier height, it also directly introduces deep hole traps which impede the vertical transport of holes through these layers.

2.4 P-type Conductivity

Highly conductive p-type layers (waveguide and EBL) are essential to efficiently inject holes into the active region of LDs. But the conductivity of p-type III-N materials is usually inferior to that of the n-type materials. This is primarily attributable to the limited p-type doping efficiency because of the high activation energy of Mg dopant atoms and possibly other compensation mechanisms [73-75]. The situation worsens approaching wider bandgap materials. The electrically active concentration of ionized impurity atoms is determined by Fermi-Dirac distribution [76] as shown in the equation (2.8):

$$N_A^- = \frac{N_A}{1+(g_A)e^{\left(\frac{E_A - E_{F,p}}{k_B T}\right)}} \tag{2.8}$$

where N_A is the substitutional acceptor concentration, g_A is the degeneracy factor for the impurity level, E_A is the acceptor ionization (activation) energy, and $E_{F,p}$ is the quasi-Fermi energy level for holes. Holes also move slowly because of their heavier effective masses. Poor conductivity of p-type layers in LD designs has several consequences. Joule heating may necessitate the operation of DUV LDs in pulsed mode instead of continuous wave (CW) mode. A large fraction of the applied voltage may be dropped across the p-waveguide and EBL because of the parasitic series resistance. This voltage drop may reduce the effectiveness of the EBL to block the leakage of electrons from the active region as a result of band-bending. Artificial hole blocking layers may emerge on the p-side because of the unscreened polarization charge at the waveguide/EBL and EBL/spacer interfaces, limiting the mechanism for hole injection to inefficient thermionic emission.

To mitigate the deleterious effects of low p-type conductivity, various approaches are now the focus of intensive research. Recent publications document very encouraging new strategies for reducing the high activation energy of Mg dopants [77-81] or otherwise increasing free hole concentration in binary GaN and related materials [82], including one report of up to 7.9×10^{19} cm^{-3} free hole concentration in p-GaN [83]. A technique known as "polarization doping" has been suggested for the improvement of p-type dopant (Mg) ionization efficiency in compositionally graded AlGaN layers through the field ionization of the dopant atoms via the electric field induced by polarization charge [31, 84-89]. This appellation is somewhat misleading, as electric fields of sufficient magnitude to ionize deep acceptor atoms would necessarily drive free carriers away from the high-field region, leaving behind only fixed space charge rather than highly conductive material. Nevertheless, reports in the literature for both N-face [31, 84,

85, 88] and the conventional metal-face [86, 87, 89] growths purport to have demonstrated the "polarization doping" effect in graded materials; I will argue that any such improvements in conductivity are for different reasons. If N-face growth is adopted, one must not only ensure good crystalline quality of the epitaxial layers, but also make Ohmic contact to a wide bandgap p-type layer [87].

2.5 Optical Absorption Loss

Ohmic metallization for the p-contact is highly absorptive at DUV emission wavelengths. For instance, the absorption coefficient of nickel is 1.06×10^6 cm^{-1} at 250 nm [90]. Therefore, even a small penetration of the optical field into the p-Ohmic metal may yield a large absorption loss. The distributed optical loss can be expressed [8] by the equation (2.9):

$$L = \iint \alpha(x,y)|\Psi(x,y)|^2 dxdy \tag{2.9}$$

where α is the position dependent absorption coefficient. For III-N epitaxial layers, α can be calculated using the imaginary part, k of the complex refractive index and the emission wavelength, λ according to the equation (2.10):

$$\alpha = \frac{4\pi}{\lambda} k \tag{2.10}$$

To minimize the overlap between the optical mode profile and p-Ohmic metal, it is necessary to use wide bandgap (low refractive index) materials as the p-waveguide layers. But they suffer from poor p-type conductivity and the related consequences are discussed in the previous section (section 2.4). Although narrow bandgap III-N materials exhibit a lower activation energy for Mg dopants, and therefore provide superior p-type

conductivity, their use as p-type waveguide layers may introduce undesirable effects in vertical injection UV LD designs. The optical mode profile may shift toward the p-waveguide layer because of the higher refractive index. This shift tends to degrade the optical confinement factor and introduce waveguide absorption loss in the p-type layer at DUV wavelengths. The p-type conductivity considerations make it difficult to design waveguides that keep the optical mode profile centered on the active region and simultaneously minimize the optical absorption losses in the p-Ohmic metal and p-type layers.

To minimize the absorption losses and solve growth related issues, InGaN based longer wavelength QW LDs have been reported in which epitaxial p-cladding layer is replaced with non-epitaxial material [91, 92], such as silver, indium tin oxide, silver-palladium-copper alloy. At longer wavelength (~ 410 nm), silver exhibits a very low refractive index (~ 0.17) [90, 91], offering a significant index contrast relative to the active region. Although silver is absorptive (6.35×10^5 cm^{-1} at 410 nm) [90], the large index contrast minimizes the penetration of the optical field into the silver cladding layer. Unfortunately, this large index contrast decreases at DUV wavelengths [90] rendering silver a lossy waveguide or cladding layer material for DUV LD designs. Figure 2.3 shows the wavelength dependence of silver's refractive index and optical absorption coefficient.

FCA via indirect phonon-assisted processes may contribute a significant fraction of the total optical loss. Kioupakis *et al.* [93] have shown that phonon-assisted absorption of holes in the p-doped waveguiding and cladding layers is a dominant loss mechanism in GaN LDs. The high activation energy of Mg dopant makes the situation worse, because in order to ensure adequate conductivity, a very high chemical concentration of Mg dopants is needed. Huang *et al.* [94] and Kuramoto *et al.* [95] proposed asymmetric waveguide structures that shift the optical mode toward the less-lossy n-side to minimize the indirect phonon-assisted FCA loss in p-type layers. N-type III-N layers are less-lossy

because a lower chemical concentration of Si dopants is needed to achieve target conductivity (better ionization efficiency).

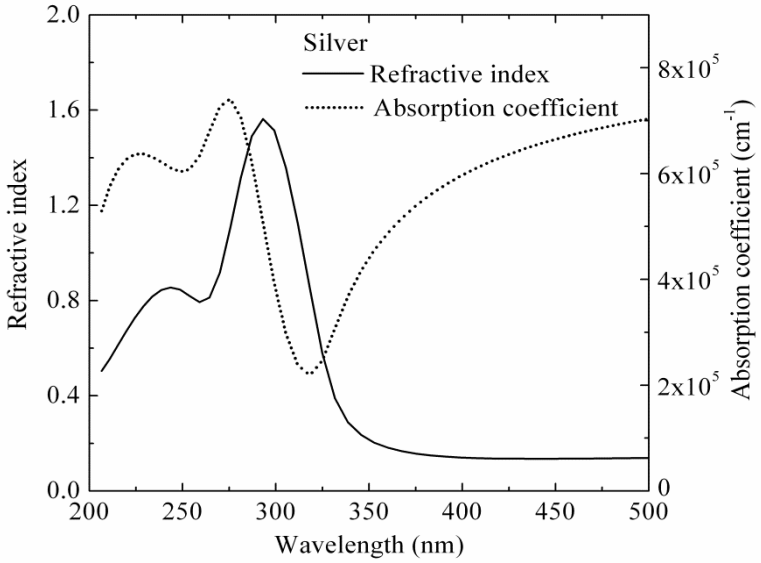

Figure 2.3: Refractive index and absorption coefficient of silver as a function of wavelength [90].

2.6 Polarization of the Optical Field and Strain Relaxation

Polarization of the light emitted by III-N ternaries and quaternaries depends on a number of factors such as composition, strain etc. It is dominated by either TE mode or TM mode. For ridge shaped LDs, TE modes offer better optical confinement than the TM modes. Weaker confinement of the TM modes may lead to greater optical losses associated with the Ohmic metallization for p-contact. These losses may be partially suppressed with a thicker p-waveguide at the expense of additional series resistance and Joule heating. In bulk AlN, stimulated emission is strongly TM polarized [23] because

the split-off (CH) band is the topmost valence band [8]. As crystal-field splitting energy of AlN is negative (-227 meV), there is a tendency to believe that optical emission of Al-rich III-N alloys is TM polarized [96, 97]. It is important to understand optical polarization from the perspective of bandstructure. In unstrained AlGaN alloys with high aluminum content, the CH band lies energetically above the heavy-hole (HH) band. Separation of the CH band and HH band is reduced in strained AlGaN alloys grown on AlN templates. Sufficiently large compressive strain and/or quantum confinement can eventually cause the crossover between HH and CH bands and thus favor TE polarization. Figure 2.4 shows a schematic drawing of this crossover between HH and CH bands in the presence of strain. Banal *et al.* investigated the polarization properties of $Al_xGa_{1-x}N$/AlN QWs grown on sapphire (0001) substrates [98] and observed that the TE mode is dominant for $x < 0.82$.

For the III-N based LDs and LEDs, usually it is assumed that the entire epitaxial structure is grown pseudomorphically on top of the substrate. In reality, if the total thickness of the epitaxial structure exceeds a certain limit, known as the critical thickness, strain will begin to relax through the formation of dislocations. The lattice constant of a partially relaxed epitaxial layer can be modeled [99] by the equation (2.11):

$$a_{in-plane}(t) = a_e + \frac{t_c}{t}(a_s - a_e) \tag{2.11}$$

where a_s and a_e are the lattice constants of the substrate and epitaxial layer (in their relaxed and equilibrium condition) respectively, t_c is the critical thickness for pseudomorphic growth and t is the thickness of the epitaxial layer. This equation is valid for $t > t_c$. To ensure TE polarization (and avoid introducing gain-compromising defects), it is necessary to grow the active regions within the critical thickness for pseudomorphic growth. This critical thickness depends primarily on the lattice mismatch between the substrate and the epitaxial layer. Greater lattice mismatches may lead to smaller critical

thicknesses. Several models have been reported for estimating the critical thickness of epitaxially grown materials [100-102].

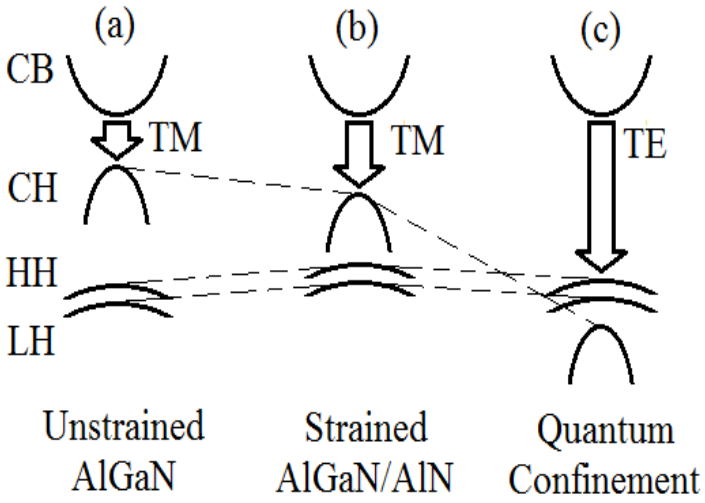

Figure 2.4: Schematic illustration of bandstructures for (a) unstrained $Al_xGa_{1-x}N$, (b) strained $Al_xGa_{1-x}N$ on AlN, and (c) $Al_xGa_{1-x}N$/AlN QWs near the Γ point [98].

Among them, Fischer's model [101] is an equilibrium model for strain relaxation in metastable heteroepitaxial semiconductor structures. Critical thicknesses estimated by this model are more accurate than those predicted by the Matthews-Blakeslee model [100]. Fischer's model was originally applied to SiGe/Si heterostructures. Very few authors have applied it properly to III-N epitaxial materials [99, 103, 104]. In fact, published experimental data on critical thickness, obtained using photoluminescence, mobility and conductivity measurements, are different than those predicted by Fischer's model [104, 105], and provide encouragement that rather thick layers can be grown pseudomorphically.

It has been suggested that strain relaxation with the help of thicker buffer layers and suitable growth conditions [106, 107] may be exploited to improve LD performance

through a reduction of piezoelectric polarization charge in the active region. Unfortunately, such strain engineering alone often affects only minor change in the net interfacial polarization charge. Moreover, it is important to consider the ramifications of strain engineering from the perspective of optical polarization. Lack of compressive strain may reduce the optical gain of TE modes in DUV LDs grown on AlN substrate, incurring a penalty to threshold current. Reduction of compressive strain may also enhance coupling to TM modes and may lead to multi-mode operation, and greater optical losses.

CHAPTER 3

SIMULATION MODEL

In recent years, a few research groups have documented work involving III-N LD simulation in the literature. Among the commercial laser simulation packages used are Crosslight's Laser Technology Integrated Program (LASTIP) [108, 109], Synopsis' Technology Computer Aided Design (TCAD) platform [94, 110], the STR Group's Simulator of Light Emitters based on Nitride Semiconductor (SiLENSe) [111], and RSOFT's LaserMOD software [112], the latter of which derives from the Minilase-II program [113] developed at the University of Illinois. Significantly fewer studies involving non-commercial III-N LD simulation software have been documented in the literature. Among them, Karbownik and Sarzala have reported the numerical simulation of an InGaN/GaN ridge waveguide laser based on a finite element discretization of the energy balance equations and an effective index model for optical modes [114]. Witzigmann *et al.* have developed and applied numerical simulation software to study the optical spectra of InGaN/GaN MQW light emitters, based on a finite volume discretization of the device equations and a vector description of optical modes [115].

The fundamental set of equations used for the purpose of laser simulation in this dissertation are the (1) Poisson equation, (2) Charge carrier continuity equations, (3) Quantum-well scattering equations (for QW carrier capture), (4) Quantum-well gain calculations (Schrödinger equation), (5) Photon rate equation and (6) Helmholtz equation. The coupling between the different equations in the laser simulation is illustrated in Figure 3.1, in which important quantities exchanged between different equations are mentioned together with the directional flows between the equation blocks. The Poisson equation and carrier continuity equations for electron and hole are the three governing

equations for charge transport in semiconductor devices under low field regime, in which the drift-diffusion equations are valid. The Poisson equation is shown in equation (3.1):

$$\nabla . \varepsilon \nabla \varphi = -q(p - n + N_D - N_A) \tag{3.1}$$

where ε is the electrical permittivity, q is the elementary electronic charge, p and n are the hole and electron densities, N_D is the concentration of ionized donors and N_A is the concentration of ionized acceptors.

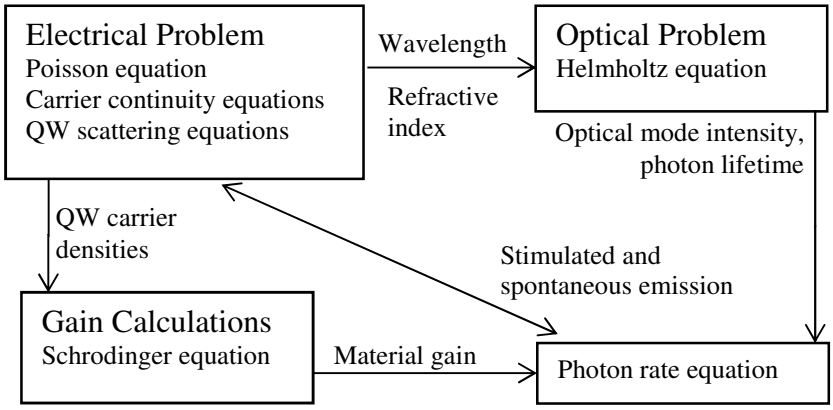

Figure 3.1: Coupling between different models used in the laser simulation.

Electron and hole continuity equations are shown in equation (3.2) and equation (3.3):

$$\nabla . \vec{J}_n = qR_{net} + q\frac{\partial n}{\partial t} \tag{3.2}$$

$$-\nabla . \vec{J}_p = qR_{net} + q\frac{\partial p}{\partial t} \tag{3.3}$$

where R_{net} is the net electron–hole recombination rate, $\vec{J}_n$ is the electron current density, and $\vec{J}_p$ is the hole current density. Quantum confined electron and hole populations within the MQW active region are calculated according to a strain-dependent 8-band k.p

Hamiltonian appropriate for wurtzite material [113]. Interactions between free and bound carrier populations are governed by carrier-carrier and carrier-phonon scattering. A ballistic transport approach is used to model the carrier capture or escape into or out of a quantum well [116]. Carrier populations are separated into bound and continuum states, and separate continuity equations are applied to both populations. The QW scattering model accounts for the net capture rate, that is, not all of the carriers will be scattered into the bound states of the quantum-well. A thermionic emission model is employed to describe the transport of free carriers across heterojunctions [116, 117]. Fixed polarization charge (spontaneous and piezoelectric) is considered at each polar interface [8]. The Poisson equation is used for self-consistent coupling of electrostatic potential with bound and free charge carrier populations. Optical modes of the LD structure are calculated according to the vector Helmholtz equations shown in equation (3.4) and (3.5):

$$\left(\frac{\partial^2}{\partial x^2}+\frac{\partial^2}{\partial y^2}\right)\vec{E}(x,y)+k_0^2\left(n^2(x,y)-\varepsilon_{eff}\right)\vec{E}(x,y)=0 \tag{3.4}$$

$$\left(\frac{\partial^2}{\partial x^2}+\frac{\partial^2}{\partial y^2}\right)\vec{H}(x,y)+k_0^2\left(n^2(x,y)-\varepsilon_{eff}\right)\vec{H}(x,y)=0 \tag{3.5}$$

where $\vec{E}(x,y)$ is the electric field vector, $\vec{H}(x,y)$ is the magnetic field vector, ε_{eff} is the effective dielectric constant, $n(x,y)$ is the refractive index profile, and k_0 is the wavenumber of the mode [118]. The Helmholtz equations are solved by the finite-element method described in [119]. The rate equation for photons is described [8] in the equation (3.6):

$$\frac{dS_m}{dt}=\left(\frac{c}{n_{eff}}G_m-\frac{1}{\tau_{ph}}\right)S_m+C_mR_{sp} \tag{3.6}$$

where S_m is the integral of the photon density for mode m, G_m is the gain, τ_{ph} is the photon lifetime, C_m is the spontaneous emission factor, and R_{sp} is the integral of the spontaneous emission rate. A set of photon rate equations for the energy associated with each mode is solved self-consistently with the aforementioned electronic equations, coupling the optical and electronic problems. The Newton iteration method is used to solve the electrical and optical problems self-consistently. When the iteration converges, the solution set for the current bias is used as an initial guess for the next bias. In this way, continuous wave operation of the laser diode is simulated.

CHAPTER 4

AlInN DUV LASER DIODES ON AlN SUBSTRATES USING TAPERED ELECTRON BLOCKING LAYERS

We have presented a 250 nm LD design in reference [120] based exclusively on AlInN active layers grown epitaxially on a bulk AlN substrate, and discussed its operation in terms of numerical simulations. DUV LDs emitting in the spectral range between 240 and 260 nm will find natural application to direct sterilization and disinfection [121], next-generation high-density optical data storage devices [122], etc. AlInN offers a new and promising alternative to AlGaN for the realization of optoelectronic devices operating in the UV-C band in terms of bandgap and waveguide design, yet has received relatively little attention in the literature. The compressive strain of pseudomorphic AlInN layers on AlN is greater than that of AlGaN on AlN for any given value of optical bandgap. Therefore, the TE mode which offers better optical confinement in ridge-shaped geometry, will be dominant in AlInN/AlInN LDs in the presence of any partial strain relaxation. These considerations render AlInN a promising alternative to AlGaN for high efficiency LD devices operating in the UV-C band.

Our design features a tapered EBL because homogeneous EBLs may lead to a parasitic inversion layer at the spacer/EBL interface which reduces optical gain and also give rise to undesirable hole blocking layers on the p-side, exacerbating the problem of hole injection. We have also explored alternatives to the tapered EBL design. Our simulation results suggest that unlike other alternatives, the tapered EBL design eliminates the parasitic inversion layer without any undesirable side effect.

4.1 Epitaxial Structure Design

In order to achieve minimum threshold current and maximum slope efficiency for an AlInN/AlInN LD design, we have conducted a directed exploration of a rich design parameter subspace by means of numerical simulation, and propose the epitaxial layer structure detailed in Table 4.1.

Table 4.1: Epitaxial layer structure for an AlInN/AlInN LD design operating at 250 nm. EBL and n-cladding (inner) layer compositions are graded to redistribute interfacial polarization charge over their entire thickness.

Layer Name	Material	Thickness (nm)	Refractive index
Contact	GaN	10	2.3
P-cladding (Outer)	$AlIn_{0.05}N$	600	2.1875
P-cladding (Inner)	$AlIn_{0.10}N$	100	2.225
EBL	$AlIn_xN$	10	2.2363 ~ 2.2062
Spacer	$AlIn_{0.12}N$	4.0	2.24
QW	$AlIn_{0.17}N$	2.0	2.2775
QWB	$AlIn_{0.12}N$	4.0	2.24
N-cladding (Inner)	$AlIn_xN$	100	2.2265 ~ 2.2385
N-cladding (Outer)	$AlIn_{0.05}N$	600	2.1875
Buffer	$AlIn_{0.03}N$	1000	2.1725
Substrate	AlN	–	2.15

Two-dimensional calculations predict good optical confinement (~ 1.00%) for 650 μm LD stripes formed by etching to a depth of 0.61 μm, or 100 nm above the top surface of the electron blocking layer (EBL), with lasing at 250 nm. The corresponding optical

mode profile is shown in Figure 4.1(a). Figure 4.1(b) illustrates the energy band diagrams and carrier densities, at a bias condition above the lasing threshold.

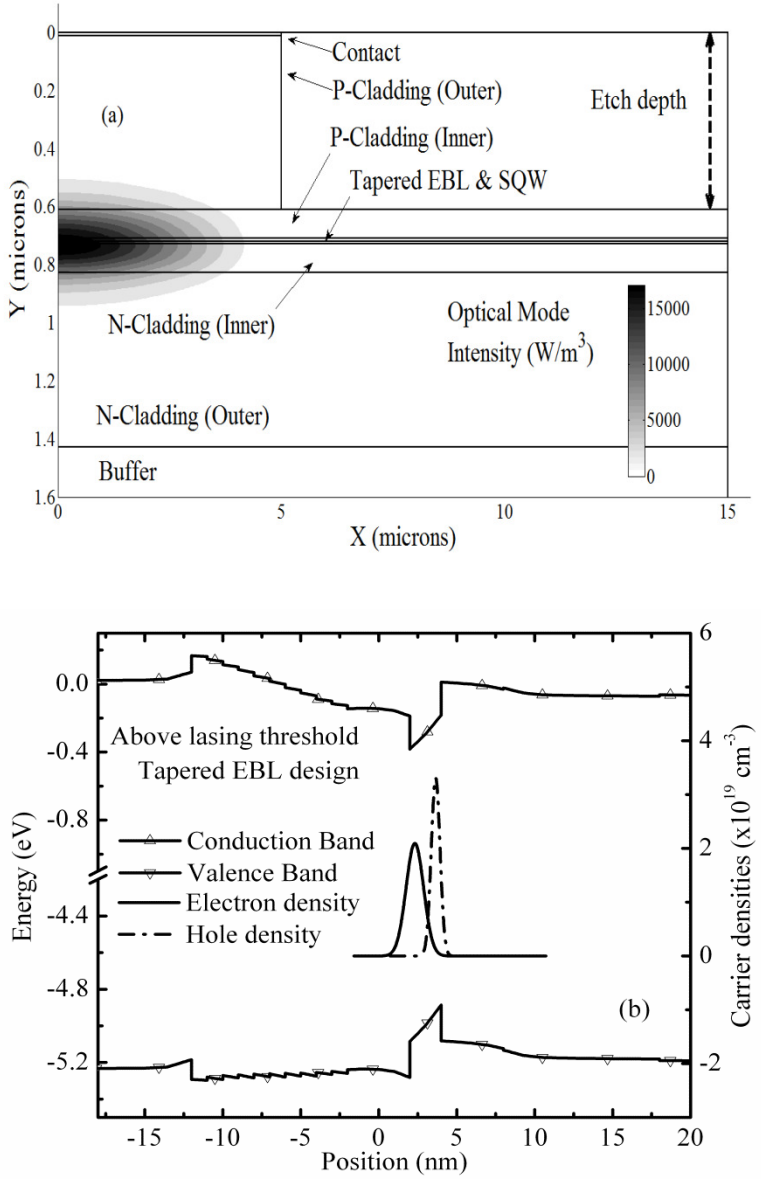

Figure 4.1: (a) Optical mode profile corresponding to the epitaxial structure of Table 4.1 (Only the fundamental TE mode is shown here) and (b) energy band diagrams and carrier densities above the lasing threshold. The linearly graded (tapered) EBL affects a volumetric redistribution of polarization charge, suppressing a parasitic inversion layer at the spacer/EBL interface.

Refractive indices used for optical mode calculation are tabulated in Table 4.1, and are calculated from binary refractive indices [123] using Vegard's law without bowing parameters. The design presented here assumes highly conductive (and wide bandgap) cladding and waveguide layers. Therefore, the waveguide has sufficient refractive index contrast and the effect of bowing parameters should not be significant. Although optical confinement factor may seem low, increasing QW thickness and/or increasing the number of QWs is not an option for AlInN/AlInN LDs for two reasons. Carrier capture time is very small (~ 1.0 ps) for injected holes [124-127]. As a result, increasing the number of QWs gives rise to a non-uniform distribution of carriers in the active region (results not shown here), diminishing optical gain. Secondly, increasing the QW thickness will reduce the electron and hole wave function overlap inside the active region due to polarization charge induced built-in electric fields [52, 53].

In order to optimize the optical confinement factor, we have investigated LD performance for different cladding layer thicknesses and material compositions. LD structures with different cladding layer designs have similar epitaxial layers. The LD structure is assumed to be 650 μm long with a mesa width of 10 μm. The cross-sectional area of the p-contact is 6.50×10^{-5} cm^2, and the entire structure is assumed to be pseudomorphically grown on top of a *c*-axis AlN substrate. Simulation results in Figure 4.2 show the effect of cladding layer indium content on the L-I curve. In-rich cladding layer designs increase threshold current in spite of their higher electrical conductivity due to their lower optical confinement factor. In the low In content limit (around 0.03 ~ 0.05), however, it is electrical conductivity rather than optical confinement factor which plays the larger role. As a consequence, minimum threshold current is reached at $AlIn_{0.05}N$. Above 5% indium content, the reduction in optical confinement factor becomes significant and outweighs the advantage of a conductive cladding layer design. A similar phenomenon, also attributable to a reduction in optical confinement factor, is observed for thicker cladding layer designs (illustrated in Figure 4.3). As the refractive index

contrast between the SQW region and the cladding layer is comparatively smaller in AlInN-based epitaxial structures than in AlGaN alternatives, thicker cladding layers result in an even greater penetration of the optical mode profile into the cladding region, and a decrease in optical confinement factor.

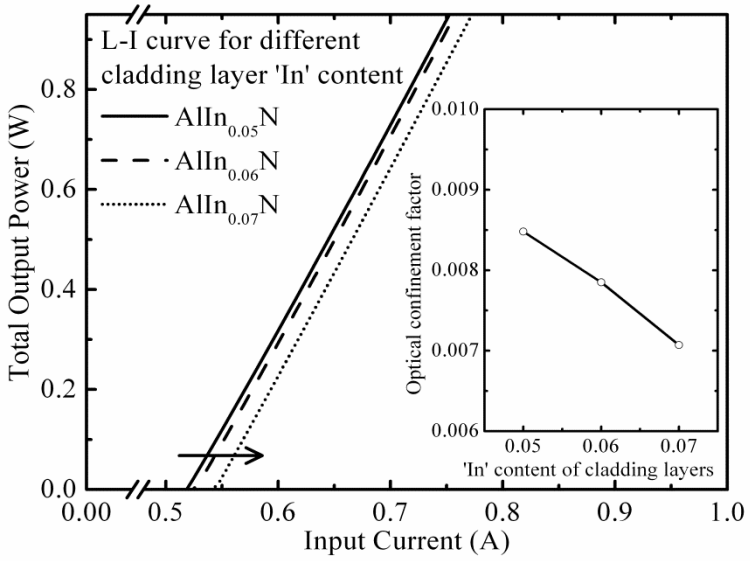

Figure 4.2: L-I curves for different cladding layer indium content. The inset shows the change in optical confinement factor with cladding layer indium mole fraction. Indium rich cladding layers reduce optical confinement and degrade LD performance despite their improved carrier mobility.

4.2 Effect of Strain Relaxation

In our numerical simulations, it is assumed that epitaxial buffer layers do not exceed the critical thickness for strain relaxation, and therefore the AlN substrate determines the in-plane lattice constant for all subsequently grown material. Calculations based on Fischer's model indicate that a 1.00 μm thick $AlIn_{0.03}N$ buffer layer grown on an AlN substrate will relax sufficiently to determine the in-plane lattice constant of

subsequently grown pseudomorphic layers [99, 101, 104, 128]. However, Fischer's model is an equilibrium model for strain relaxation in metastable heteroepitaxial semiconductor structures. Originally applied to SiGe/Si heterostructures, very few authors have applied it properly to III-N epitaxial materials [99, 104, 128]. In fact, published experimental data on critical thickness, obtained using photoluminescence (PL), mobility and conductivity measurements, are different than those predicted by Fischer model [104, 105], and provide encouragement that rather thick layers can be grown pseudomorphically on top of III-N [129].

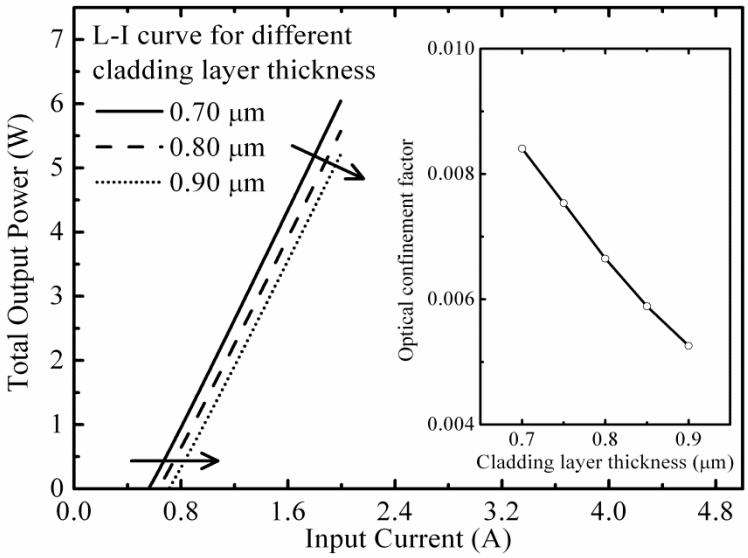

Figure 4.3: L-I curves for different cladding layer thickness. Inset figure shows optical confinement factor versus cladding layer thickness. Optical confinement factor decreases in thicker cladding layer design due to the lower refractive index contrast in AlInN based material system.

Strain plays a very important role in determining the polarization of the optical field. The effect of in-plane lattice constant on threshold current and lasing wavelength is illustrated in Figure 4.4, considering both TE and TM optical modes. The TE mode is dominant in compressively strained AlInN/AlInN LDs, while tensile strain favors the TM

mode. For ridge geometry LDs, weaker confinement of the TM mode can lead to losses associated with the upper Ohmic metallization. Partial suppression of these losses may be achieved with a thicker p-cladding layer at the expense of additional series resistance.

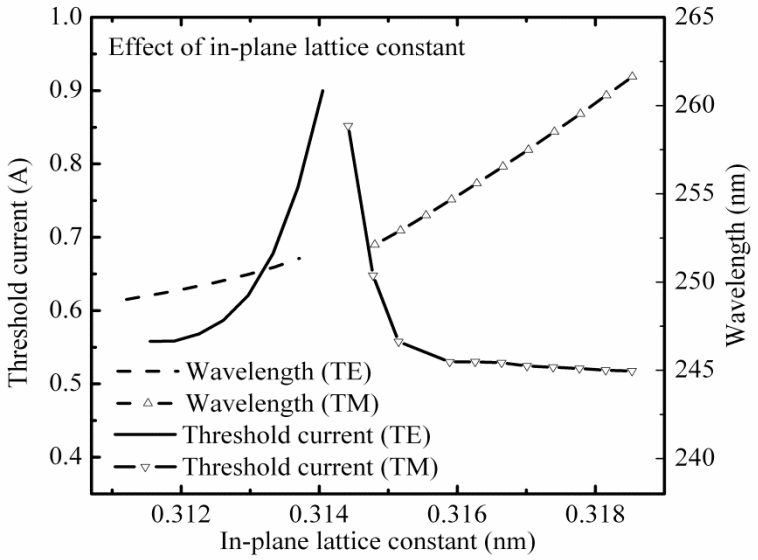

Figure 4.4: Threshold current and lasing wavelength for different in-plane lattice constant. The TE mode dominates in a compressively strained pseudomorphic AlInN layer on an AlN substrate. On the other hand, tensile strain favors the TM mode.

4.3 Alternatives to Tapered EBL design

In our proposed epitaxial structure (see Table 4.1), we suggest a tapered EBL design in which the EBL material composition is linearly graded rather than uniform. Before discussing the merits of the tapered EBL design, we first address the problems associated uniform EBL layers in AlInN-based UV LDs. Figure 4.5 shows the energy band diagram and carrier densities for a uniform EBL design. A large net polarization charge exists at the EBL/spacer interface due to piezoelectric polarization resulting from strain. This plunges the conduction band downward relative to the electron quasi-Fermi

level, forming a parasitic interfacial inversion layer in the p-type spacer material. Due to the influence of non-radiative recombination processes, the formation of this parasitic inversion layer leads to a reduction in optical gain. In all our simulations, we have used a Shockley-Read-Hall (SRH) recombination lifetime of 1.0 ns [109] and an Auger recombination coefficient of 1×10^{-30} cm^6 s^{-1} [130]. Due to the lack of documented studies of Auger coefficients for the AlInN material system in the literature, we have used the highest value reported for the related material InGaN [130]. We expect that the actual Auger coefficients for AlInN are in reality significantly lower, and interpret our results as a 'worst case scenario' for quantities such as threshold current which are adversely influenced by non-radiative recombination processes. In order to suppress the formation of a parasitic inversion layer at the EBL/spacer interface, we have investigated LD designs with a variety of EBL and spacer layer attributes.

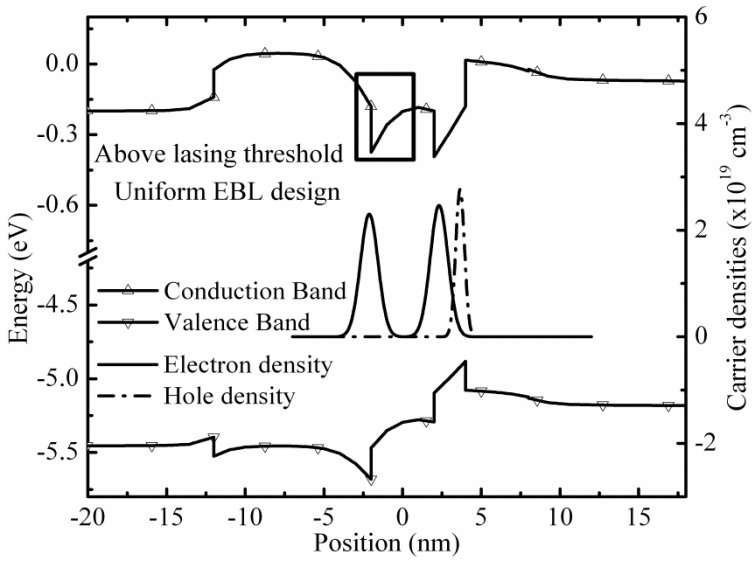

Figure 4.5: Energy band diagrams and carrier densities of uniform EBL design (above lasing threshold). A parasitic inversion layer exists at the EBL/spacer interface.

Piezoelectric polarization charge can be influenced by a change in strain. Lowering the indium content of the spacer layer or increasing that of the EBL may reduce the lattice mismatch between these two layers, and thus minimize the net interfacial polarization charge. Figure 4.6 demonstrates that a reduction of spacer layer indium content improves both threshold current and slope efficiency. As expected, this is attributable to a reduction in lattice mismatch, and leads consequentially to the reduction of net polarization charge at the EBL/spacer interface.

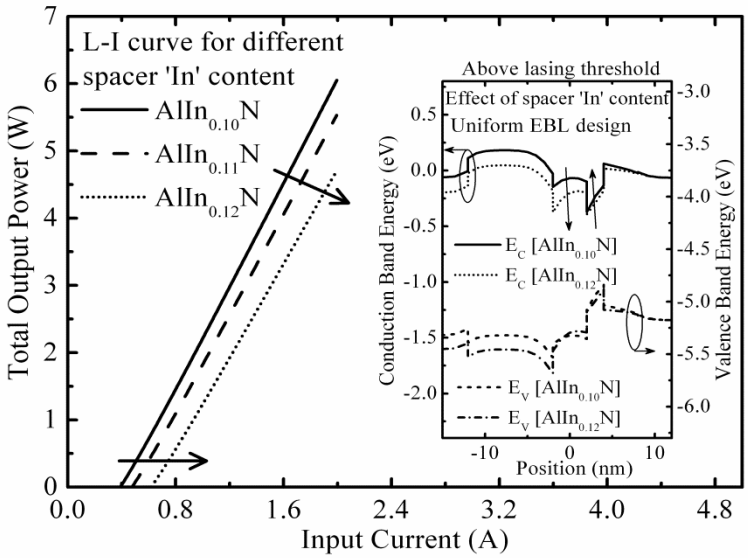

Figure 4.6: L-I curves for different spacer In content. Inset figure shows how energy band diagrams (above lasing threshold) change with spacer In mole fraction. Lowering spacer In content may eliminate parasitic inversion layer but as a side effect, it modifies the energy band diagram of the SQW.

But there is a problem with this approach: net polarization charge at the lower spacer layer interface increases, plunging the quantum well conduction band downwards in energy relative to the quasi-Fermi level. This may not only reduce the electron-hole overlap in QW, but also influence lasing wavelength as well. Similarly, indium rich EBL

designs also reduce threshold current and improve slope efficiency (see Figure 4.7). An undesirable side-effect of this design strategy, however, is a reduction in barrier height, compromising the effectiveness of this layer to block the leakage of injected electrons from the active region.

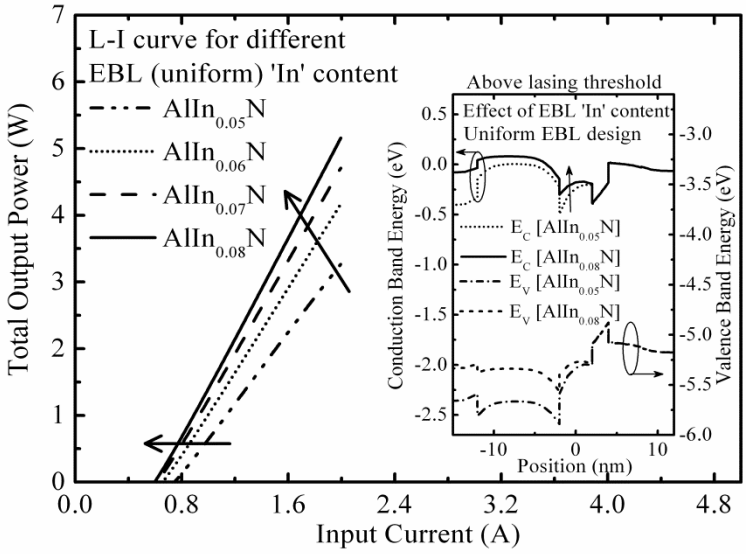

Figure 4.7: L-I curves for different EBL indium content. Inset figure shows energy band diagrams (above lasing threshold) for two different EBL indium mole fractions. An undesired consequence of this approach is the reduction of EBL barrier height.

In addition to the indium content of the spacer and EBL layers, we have also investigated whether a change in their respective thicknesses may help suppress parasitic inversion layer charge. Our simulations indicate that thicker EBL and spacer layers only slightly improve salient features of the L-I curve, but that the problem of a parasitic inversion layer persists. In theory, highly conductive spacer layers can narrow the physical extent of the parasitic inversion layer. Although Figure 4.8 shows signs of improvement in both threshold current and slope efficiency, in practice, this improvement will be limited by the reduction of minority carrier lifetime, an effect which is not

considered in the simulated L-I curves of Figure 4.8. Besides, high activation energy of Mg dopants makes the realization of sufficiently large free hole concentrations challenging in heavily doped p-type AlInN for present purposes.

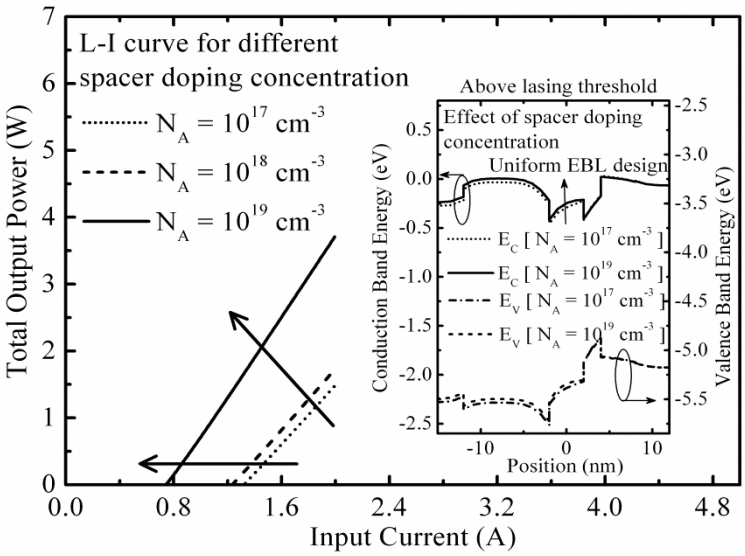

Figure 4.8: L-I curves for different spacer doping concentration. Inset figure shows energy band diagrams (above lasing threshold) for two different doping concentrations of spacer. Higher activation energy of P-type dopant makes it difficult to achieve highly conductive AlInN layers.

It is evident that the conventional, contemporary design strategies to improve LD performance presented in Figure 4.6, 4.7 and 4.8 either come with undesirable side effects or are challenging for practical implementation, and moreover do nothing to prevent the formation of pernicious, parasitic inversion layers. As mentioned earlier, the main reason for the parasitic inversion layer charge is Coulombic attraction from a large net polarization charge at the EBL/spacer interface. Linearly tapering the EBL material composition, however, affects a redistribution of this interfacial polarization charge over the entire volume of the EBL layer, suppressing the formation of any parasitic inversion layer without penalty to electron barrier height. A juxtaposition of L-I and V-I curves for

two LDs featuring tapered and uniform EBL designs is provided in Figure 4.9, from which it is evident that the tapered design results in an 8% reduction in threshold current, a 4% reduction in threshold voltage and a 20% increase in slope efficiency. The uniform EBL design compared here has the same dimension and epitaxial structure of that of tapered EBL design (Table 4.1) except that homogeneous $Al_{0.93}In_{0.07}N$ material is used for the EBL. Band diagrams (above lasing threshold) and carrier densities for both tapered and uniform EBL designs are provided in Figure 4.10, demonstrating the efficacy of the tapered EBL design in suppressing the formation of a parasitic inversion layer. Although the barrier height of tapered EBLs is reduced at the spacer/EBL interface, it is sufficiently large at the other interface to block electron leakage from the active region.

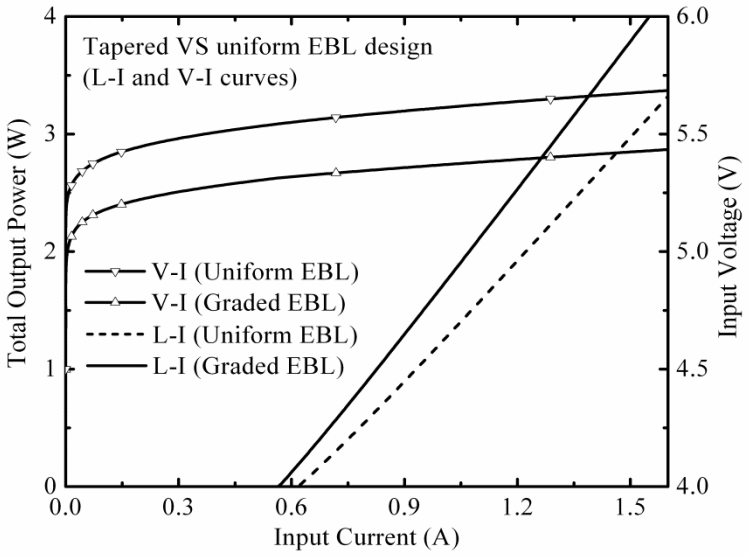

Figure 4.9: Comparison of L-I and V-I curves between tapered and uniform EBL design. Tapered design yields an 8% reduction in threshold current, a 4% reduction in threshold voltage and a 20% increase in slope efficiency.

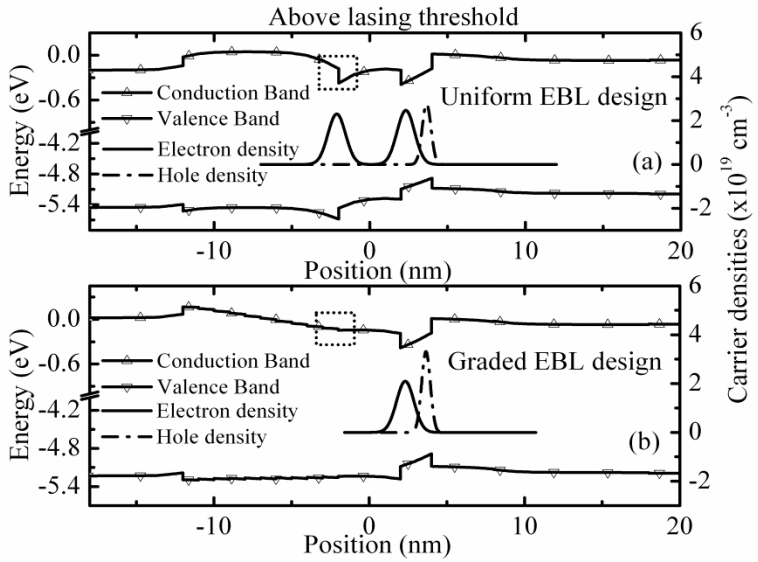

Figure 4.10: Energy band diagrams (above lasing threshold) and carrier densities of uniform (a) and graded (b) EBL design. Parasitic inversion layer charge is completely removed in (b) without any undesired side effects.

CHAPTER 5

POLARIZATION CHARGE MATCHING IN AlGaN BASED DUV LDS USING QUATERNARY AlInGaN BARRIERS

At present, the epitaxial growth of AlInN with superior crystalline quality poses some technical challenges but they don't appear to be fundamental. The issues arise primarily from the difference in optimum growth temperature between AlN and InN. Therefore, we shifted our immediate research focus to design another UV LD based mainly on AlGaN ternary materials. We have presented another 250 nm DUV edge-emitting LD design in reference [131] using polarization-charge-matched quaternary QWBs and a tapered EBL. Our design completely eliminates polarization-charge-induced built-in electric fields inside the active region and improves the overlap between electron and hole wavefunctions. Although the use of polarization-charge-matched quaternaries has already been proposed in the literature to improve performance of visible wavelength LEDs and LDs, reference [131] presents the first demonstration that this is also feasible for DUV LDs operating at sub-300 nm wavelengths. We have suggested a systematic quaternary composition selection method, which can be easily applied to LED and LD designs operating at arbitrary wavelength.

5.1 Epitaxial Structure Design

We have explored a rich design parameter subspace by means of numerical simulation in order to achieve minimum threshold current and maximum slope efficiency for an AlGaN/AlGaN edge emitting LD design, and propose the epitaxial layer structure detailed in Table 5.1. It is assumed that all layers are pseudomorphically grown on top of an AlN substrate. Two-dimensional calculations predict good optical confinement for 650

μm edge emitting LD stripes formed by etching to a depth of 0.61 μm, or 100 nm above the top surface of the EBL, with lasing at λ=250 nm. The ridge width is 10 μm and cavity length is 650 μm. Left and right facet reflectivities are assumed to be 85% and 95% respectively. For the sake of comparison, no background optical loss is considered in our simulations.

Table 5.1: Epitaxial layer structure for an AlGaN/AlGaN edge emitting LD design operating at 250 nm. EBL and n-waveguiding layer compositions are graded to redistribute interfacial polarization charge over their entire thickness [120].

Layer Name	Material	Thickness (nm)	Refractive index
Contact	GaN	10	2.3
P-cladding	$AlGa_{0.15}N$	600	2.1725
P-waveguiding	$AlGa_{0.20\sim0.15}N$	100	2.18 ~ 2.1725
EBL	$AlGa_{0.34\sim0.15}N$	40	2.201 ~ 2.1725
Spacer	$AlGa_{0.34}N$	3.0	2.201
QW (×3)	$AlGa_{0.465}N$	2.0	2.2197
QWB (×3)	$AlGa_{0.34}N$	3.0	2.201
N-waveguiding	$AlGa_{0.15\sim0.34}N$	100	2.1725 ~ 2.201
N-cladding	$AlGa_{0.15}N$	600	2.1725
Buffer	$AlGa_{0.10}N$	1000	2.165
Substrate	AlN	–	2.15

The corresponding optical mode profile is shown in Figure 5.1(a). Refractive indices used for optical mode calculation are tabulated in Table 5.1, and are calculated from binary refractive indices [123] using Vegard's law. Figure 5.1(b) illustrates the energy band diagrams and carrier densities, at a bias condition above the lasing threshold. L-I and V-I

curves are shown in Figure 5.2. Other parameters used in our calculations, including Shockley–Read–Hall lifetime and Auger recombination coefficients, have been reported in reference [120].

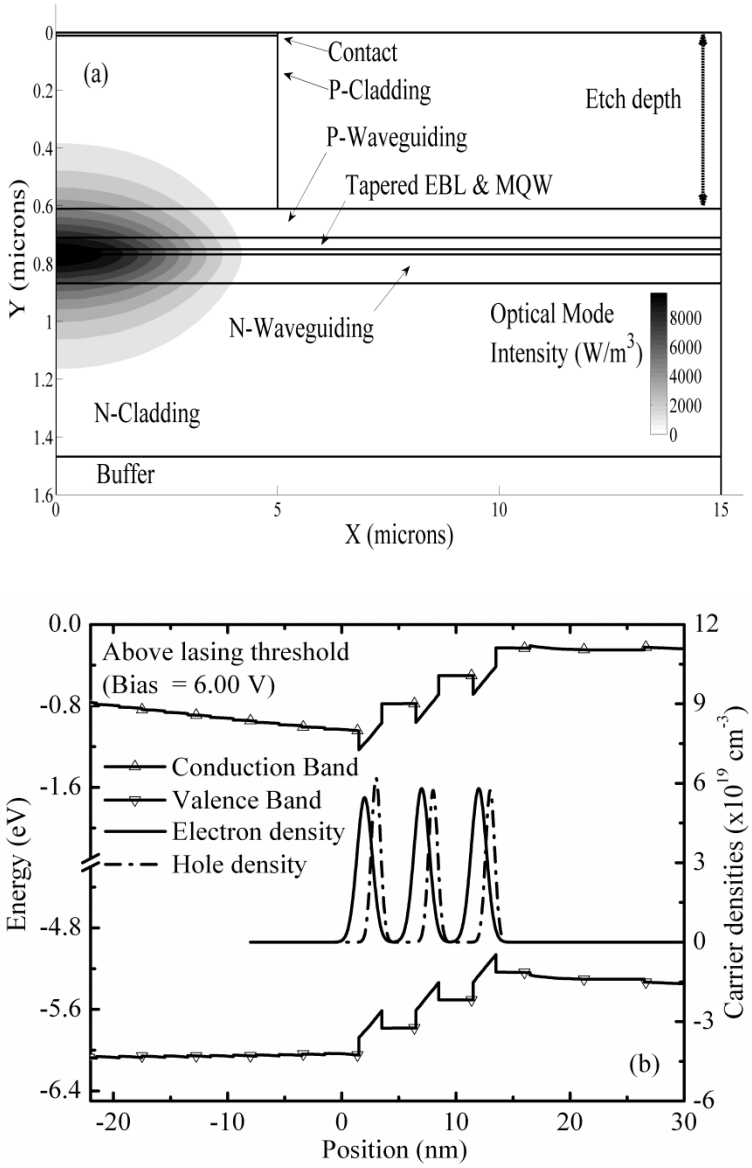

Figure 5.1: (a) Optical mode profile corresponding to the epitaxial structure of Table 5.1 (Only the fundamental TE mode is shown here) and (b) energy band diagrams and carrier densities above the lasing threshold.

Two of the major causes of non-radiative recombination are point and extended defects in epitaxial material. The influence of defects as recombination centers in our simulations is modeled by non-radiative recombination lifetime, and has a profound influence on LD performance. High defect density will lower Shockley–Read–Hall lifetimes, degrading both threshold current and quantum efficiency in the usual ways.

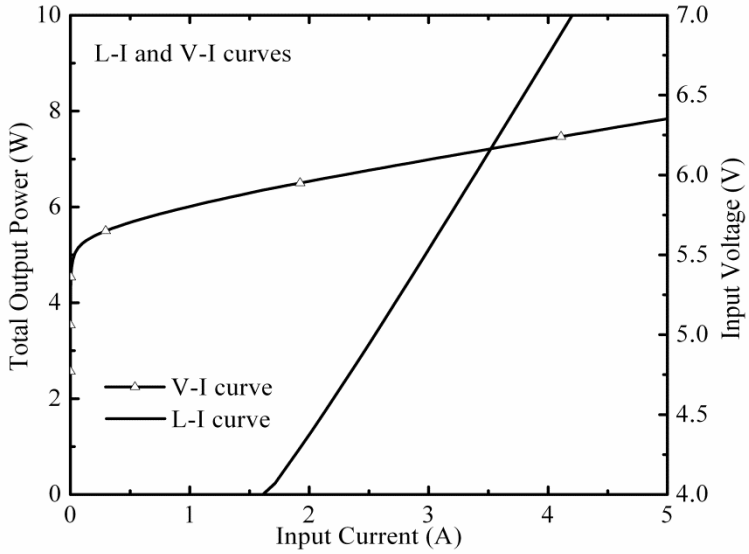

Figure 5.2: L-I curve and V-I curve of the epitaxial structure of Table 5.1.

The design trends presented here are intended to serve as a guide to epitaxial layer design, as edge-emitting DUV LDs have yet to be reported. Our calculations assume both n- and p-type free carrier concentrations in the undepleted waveguiding and cladding layers of 5×10^{18} cm^{-3}. We recognize that this level of free hole concentration may be difficult to achieve in practice at the present time. The threshold voltage of our baseline design is around 6.0 V (see Figure 5.2). Unfortunately, the experimentally measured threshold voltage of the shortest wavelength (336 nm) UV LD reported to date is significantly higher (~ 30 V) [29]. Several issues may be responsible for this large

discrepancy, including the highly nonlinear contact resistance measured in practice [132, 133], series resistance of low conductivity p-cladding and waveguide layers, artificial hole blocking layers due to unscreened polarization charge at p-waveguiding layer/EBL interface etc.

5.2 A Hypothetical Study Neglecting Polarization Charge

From the band diagrams and carrier densities of Figure 5.1(b), it is obvious that quasi-bound electron and hole populations are spatially separated within QWs because of polarization charge induced built-in electric fields. The amount of polarization charge at an $Al_{0.66}Ga_{0.34}N/Al_{0.535}Ga_{0.465}N$ interface is calculated to be 0.0112 Cm^{-2} [8]. To estimate the performance degradation due to polarization charge alone, a hypothetical structure has been simulated. In this particular simulation, the baseline design of Table 5.1 has been used but we intentionally neglected net interface polarization charge in the active region. Energy band diagrams and carrier densities are shown in Figure 5.3. The polarization-charge-free artificial active region yields better electroluminescence efficiency because quasi-bound electron and hole population within the QWs exhibit large spatial overlap. Threshold current is reduced significantly and slope efficiency is also improved (see Figure 5.4). This hypothetical study clearly indicates the usefulness of a polarization charge free active region. To realize this, we can use the design template of Table 5.1, but replace ternary AlGaN QWBs with quaternary AlInGaN material. Using quaternary AlInGaN QWBs with appropriate composition, net interface polarization charge at hetero-interfaces with ternary AlGaN QWs can be minimized.

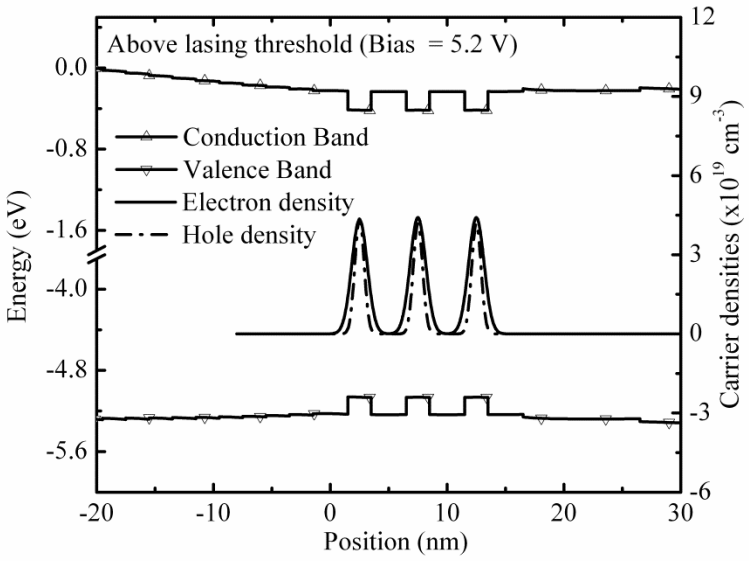

Figure 5.3: Energy band diagrams and carrier densities above the lasing threshold. In this hypothetical simulation, absence of net interface polarization charge from the active region eliminates spatial separation of electron and hole population, improves electroluminescence efficiency, reduces threshold voltage significantly.

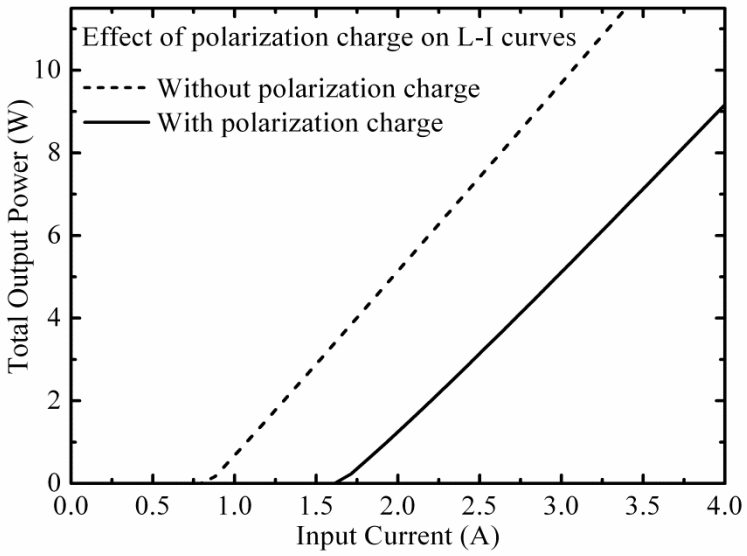

Figure 5.4: Effect of net interface polarization charge on L-I curves. Epitaxial structure of Table 5.1 is used as the baseline design. Hypothetical simulation result (where polarization charge is neglected in the active region) suggests that LD performance can be improved significantly with a polarization charge minimized active region.

5.3 Polarization-charge-matched AlInGaN Compositions

Figure 5.5 shows all the quaternary AlInGaN compositions that will yield minimum net interface polarization charge with ternary $Al_{0.535}Ga_{0.465}N$. It also shows contours of quaternaries with finite net interfacial polarization charge. If we adopt a 'brute force' technique to calculate the contour for polarization-charge-minimized quaternary $Al_xIn_yGa_{1-x-y}N$ compositions, the computational overhead may be significant depending on the resolution of x and y composition space. The calculation needs to go through all the (x, y) permutations to find the required contour. To speed up the calculation, we use course step sizes (0.01) for both x and y.

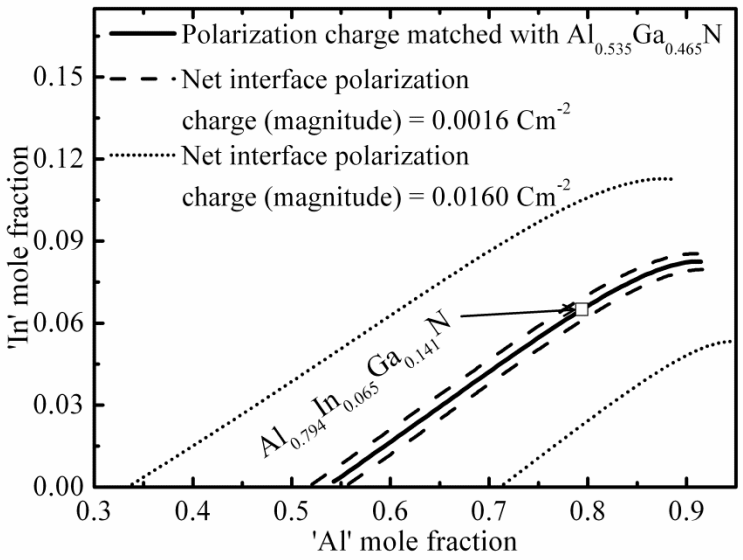

Figure 5.5: Locus of all quaternary AlInGaN compositions that minimizes net interfacial polarization charge with $Al_{0.535}Ga_{0.465}N$ QWs. Contours of quaternaries with finite net interfacial polarization charge are also shown.

For every x data point, the plot of net interface polarization charge magnitude versus y should be a V-shaped curve with a minimum. If the curve is not V-shaped, it means that there is no charge minimized composition for that x data point. Depending upon the

discretization of y, the minima of the V-shaped curve may or may not be close to 0.0 Cm^{-2}. To locate the charge minimized composition, we re-discretize y around the current minima using finer step size and repeat the charge calculation procedure. A similar method is applied to calculate the contours for finite level of polarization charges. Although technically we can use any charge-minimized composition indicated by Figure 5.5, not all quaternary AlInGaN material on this minimum polarization charge curve will behave as a QWB with respect to $Al_{0.535}Ga_{0.465}N$ QWs. It should provide sufficiently deep QWs in both the conduction band and valence band. $Al_{0.794}In_{0.065}Ga_{0.141}N$ is, for example, a promising candidate. With an AlInGaN QWB, it is necessary to compositionally grade the EBL from $Al_{0.794}In_{0.065}Ga_{0.141}N$ (bottom) to $Al_{0.85}Ga_{0.15}N$ (top) to redistribute polarization charge volumetrically [120]. N-waveguiding should undergo similar tapering for the same reason. A comparison of L-I and V-I curves for two LDs containing ternary AlGaN and quaternary AlInGaN QWB designs is provided in Figure 5.6, from which it is evident that the quaternary design results in a 57% reduction in threshold current, a 13% reduction in threshold voltage and a 10% increase in slope efficiency. Although the built-in potential of a p-n junction diode does not depend on polarization charge, our simulations indicate a reduction in threshold voltage when interfacial polarization charge is minimized. This is because the polarization fields inside the active region actually raise the effective barrier height for hole injection. With high interfacial polarization, a larger applied voltage is required to lower the p-side potential barrier sufficiently for the free flow of holes into the active region.

Band diagrams (above lasing threshold) and carrier densities for both ternary AlGaN and quaternary AlInGaN QWB designs are provided in Figure 5.7, demonstrating the ability of the quaternary QWB design to realize a polarization charge minimized active region to improve electroluminescence efficiency significantly. The quaternary QWB design implicit in the simulation results shown in Figure 5.6 and 5.7 is based on the design template of Table 5.1. Through careful design, further optimization of this

structure is possible. Using ternary QWBs, we determined that it is not possible to use QWs thicker than 2.0 nm to increase optical confinement factor [52, 53], as thicker QWs would lead to unacceptably high spatial separation of the quasi-bound electron and hole populations [52, 113]. With polarization charge matched quaternary QWBs, however, QW thicknesses can be increased beyond 2.0 nm.

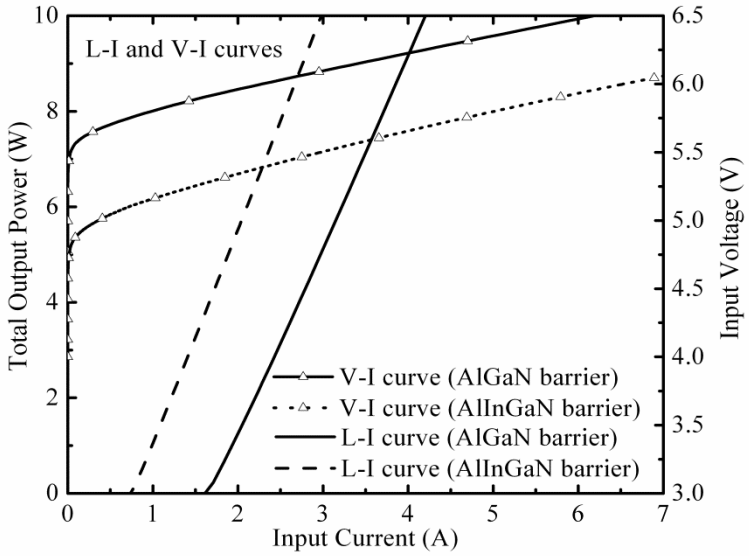

Figure 5.6: Comparison of L-I and V-I curves with ternary AlGaN and quaternary AlInGaN QWBs respectively. Polarization charge matched $Al_{0.794}In_{0.065}Ga_{0.141}N$ QWB reduces threshold current by 57%, and increases slope efficiency by 10%. Threshold voltage is also reduced by 13%.

We have investigated LD performance for different QW thicknesses and the results are shown in Figure 5.8. Thicker QW designs exhibit lower threshold current, primarily due to a larger optical confinement factor. It should be mentioned that change in QW thickness also influences lasing wavelength. A small red-shift is observed in thicker QW designs (see Figure 5.9).

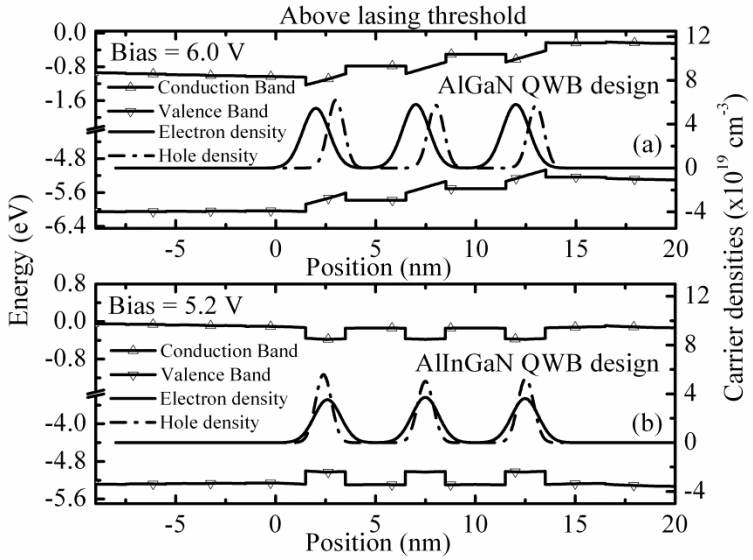

Figure 5.7: Energy band diagrams (above lasing threshold) and carrier densities of ternary AlGaN (a) and quaternary AlInGaN (b) QWB design. Polarization charge induced built-in electric field is completely eliminated in (b). This reduces threshold voltage and improves electroluminescence efficiency significantly.

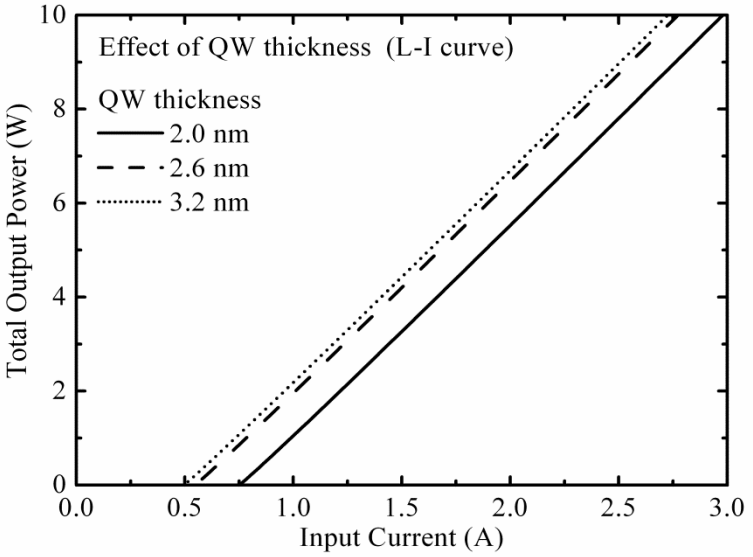

Figure 5.8: Effect of QW thickness on L-I curves. Thicker QW design can take the advantage of enhanced optical confinement factor and can reduce threshold current of quaternary QWB design further.

The red-shift can be explained from the perspective of a simple one-dimensional (1-D) rectangular potential well problem. In a 1-D rectangular well, the quantized ground state energy level comes closer to the bottom of the well as the well is made thicker. Hence, the lasing transition energy between electron and hole ground states becomes slightly smaller; this is exactly the behavior that is observed in the PL studies of QW heterostructures made from non-polar material [134]. Although optical confinement factor shows an approximately linear relationship with QW thickness, non-uniform distribution of carriers among QWs may become significant if QW thickness is increased arbitrarily, and ultimately degrade electroluminescence efficiency. Figure 5.10 shows that the threshold current of our quaternary QWB design may be approximately minimized with a QW thickness of 3.5 nm. For QWs thicker than 4.0 nm, lack of homogeneity of carrier distribution among the QWs begins to outweigh the advantage of enhanced optical confinement factor.

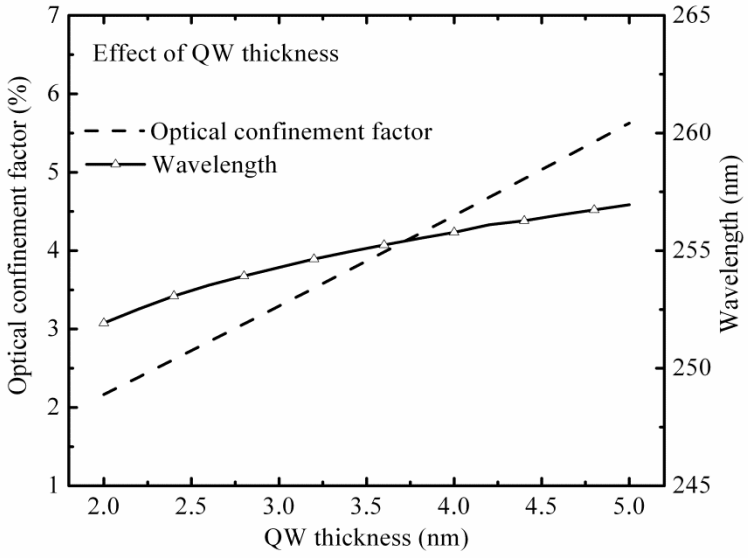

Figure 5.9: Effect of QW thickness on optical confinement factor and lasing wavelength. In a thicker rectangular potential well, quantized ground energy level comes closer to the bottom of the well. This explains why lasing wavelength becomes slightly longer in thicker QW design.

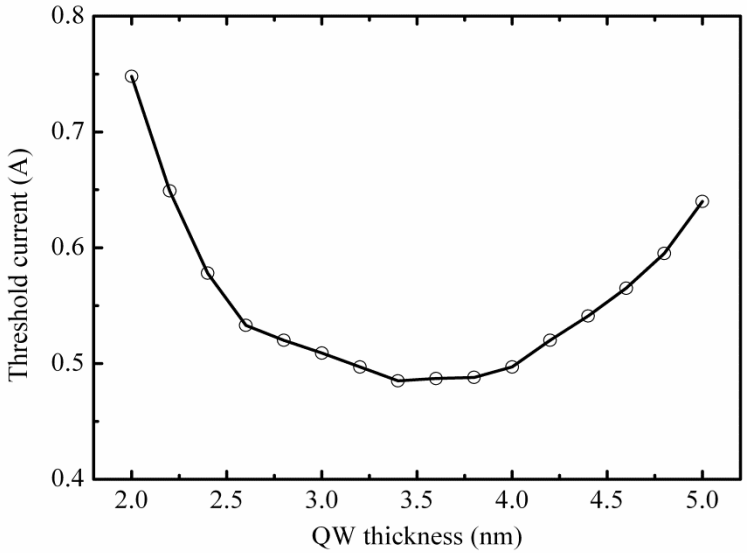

Figure 5.10: Effect of QW thickness on threshold current. Thinner (< 2.5 nm) QW designs suffer from reduced optical confinement factor. On the other hand, thicker (> 4.0 nm) QW designs give rise to non-uniformity among QWs carrier populations, which reduces electroluminescence efficiency and increases threshold current in spite of very large optical confinement factor.

This is why there is a minimum on threshold current vs. QW thickness plot (see Figure 5.10). With larger net interfacial polarization charge, this minimum may occur at a smaller thickness [135].

5.4 A Systematic Quaternary Composition Selection Method

So far, we have investigated designs with $Al_{0.794}In_{0.065}Ga_{0.141}N$ as the QWB, though many other polarization-minimizing choices for quaternary material compositions are possible. It is possible, for example, to choose polarization matched quaternaries with different bandgap energy. Figure 5.11 shows how bandgap energy (bulk and unstrained) varies along the locus of polarization charge minimized quaternaries. With a different

quaternary QWB, we can modify QW depths in the conduction band and the valence band. LD designs with shallow QWs will yield higher threshold current because only a small fraction of injected carriers will be captured inside the QWs. On the other hand, the distribution of carriers will be non-uniform if QWs are very deep [136], and one must anticipate variation of lasing wavelength with QWB bandgap energy. Table 5.2 lists band offsets and the lasing wavelength for three different quaternary QWB designs. For the QWs, 3.5 nm thick $Al_{0.535}Ga_{0.465}N$ material has been assumed. Figure 5.12 compares the L-I curves of these three designs. Low threshold current is observed with larger band offsets.

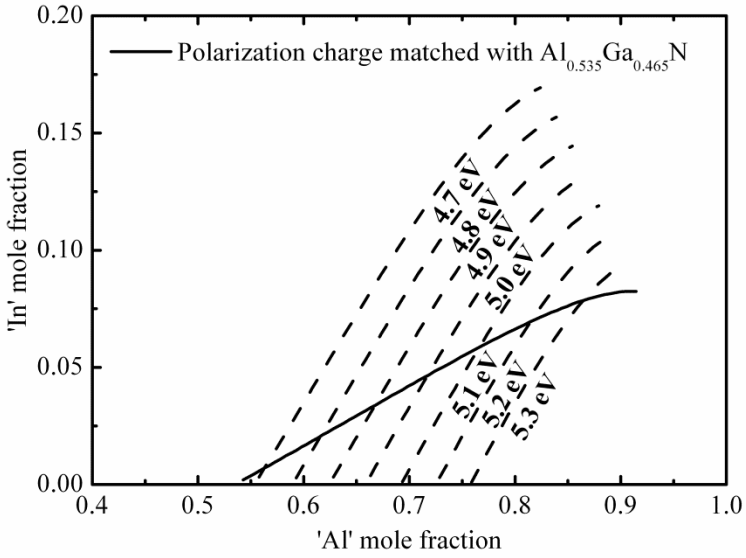

Figure 5.11: Locus of polarization charge minimized quaternary AlInGaN compositions together with contours of constant bandgap energy (bulk and unstrained).

Unfortunately, there is an upper limit of band offsets that cannot be exceeded in our design. The maximum bandgap offset, ΔE_g that can be achieved in our polarization charge minimized design with $Al_{0.535}Ga_{0.465}N$ QWs is 0.75 eV (see Figure 5.11).

However, longer UV wavelength designs can surely take advantage of comparatively deeper QWs to capture a large fraction of injected carriers.

Table 5.2: Band offsets and lasing wavelength of AlInGaN (QWB) / AlGaN (QW) edge emitting LD designs.

Quaternary QWB	Band offsets		Lasing wavelength (nm)
	ΔE_C (eV)	ΔE_V (eV)	
$Al_{0.722}In_{0.048}Ga_{0.23}N$	0.160	0.199	255.3
$Al_{0.758}In_{0.057}Ga_{0.185}N$	0.192	0.24	255.2
$Al_{0.868}In_{0.079}Ga_{0.053}N$	0.302	0.356	254.8

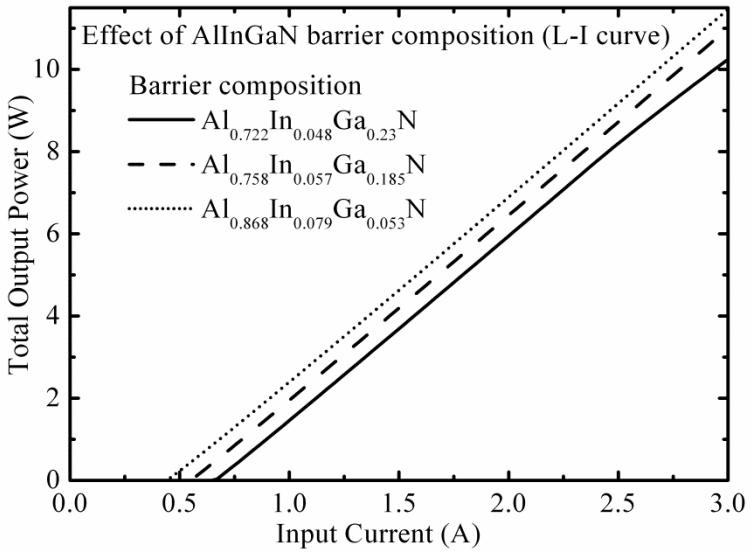

Figure 5.12: Comparison of L-I curves with different quaternary QWBs. For these simulations, 3.5 nm thick QWs have been assumed.

Conduction and valence band offsets can be calculated using the vacuum level as reference (known as the Anderson's rule or the electron affinity model [137]) or the absolute valence band energy as reference [33]. We use the electron affinity model in our simulation to determine the alignment of conduction and valence bands at heterointerfaces. Typically, band offset ratio (ΔE_c:ΔE_v) is assumed 50:50 [84] or 70:30 [138] for AlGaN/GaN material interfaces. But, it is possible to have different ratios if material interface involves AlInGaN quaternary compositions. Electron affinity of InN is significantly larger than that of AlN [8]. Hence, it is possible to make ΔE_c significantly smaller than ΔE_v (and vice-versa) if quaternary mole composition is chosen appropriately. Such an interface may not have minimized polarization charge.

5.5 Sensitivity Analysis

Our ability to grow a polarization charge minimized (or free) active region depends on how precisely we can control the composition of AlInGaN quaternaries. It may be challenging to control individual mole fractions with three digits of precision (± 0.001). Any deviation from the target quaternary QWB composition will increase net interface polarization charge. Nevertheless, significant improvement in device performance does not rely on the complete absence of interfacial polarization charge. In order to investigate the effect of partial polarization charge matching, we have simulated the LD structure of Table 5.1 with different magnitudes of net interfacial polarization charge in the active region. From the observed relationship between threshold current vs. net polarization charge, further reduction of threshold current becomes negligible for net polarization charge less than 0.0008 Cm^{-2} (see Figure 5.13). Based on this study, we conclude that maintaining the magnitude of net polarization charge below 0.0008 Cm^{-2} is sufficient to effectively suppress any electron and hole wave function separation within the QWs. It is interesting to determine how far one can deviate from target quaternary

mole compositions and remain within the tolerable limits of net interface polarization charge (< 0.0008 Cm^{-2}). For example, let us assume that our target mole composition is $Al_{0.794}In_{0.065}Ga_{0.141}N$. Figure 5.14 shows the contour line of quaternaries which will yield a net interface polarization charge (magnitude) of 0.0008 Cm^{-2} with $Al_{0.535}Ga_{0.465}N$ QWs. Any composition outside of the contour lines will yield higher polarization charge (see Figure 5.5). For the 'Al' mole fraction, the error margin is ± 0.008 and that of indium (In) mole fraction is ± 0.002. It is important to note that even a partially minimized polarization charge (< 0.0112 Cm^{-2}) design will perform better than that of the baseline structure in Table 5.1.

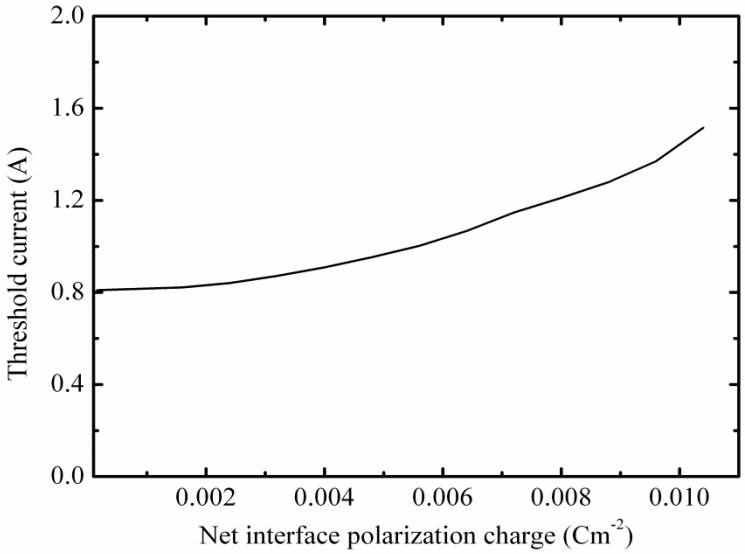

Figure 5.13: Threshold current vs. net interfacial polarization charge. If we artificially reduce the net interfacial polarization charge within the MQW active region and simulate the epitaxial structure of Table 5.1, it is observed that the threshold current decreases. However, the change is very small for net interface polarization charge below 0.0008 Cm^{-2}.

Until now, we have explored designs with quaternary AlInGaN QWBs and ternary AlGaN QWs. Unfortunately, it is not possible to do it the other way around, i.e.

with ternary QWBs and quaternary QWs. All the quaternary compositions that are polarization charge matched to a particular ternary AlGaN, have bandgap energies greater than that of the AlGaN ternary (see Figure 5.11), and provide no electrical confinement. It may be possible to design polarization charge free active regions using quaternaries for both QWBs and QWs [139], yet this approach poses greater challenges for crystal growth.

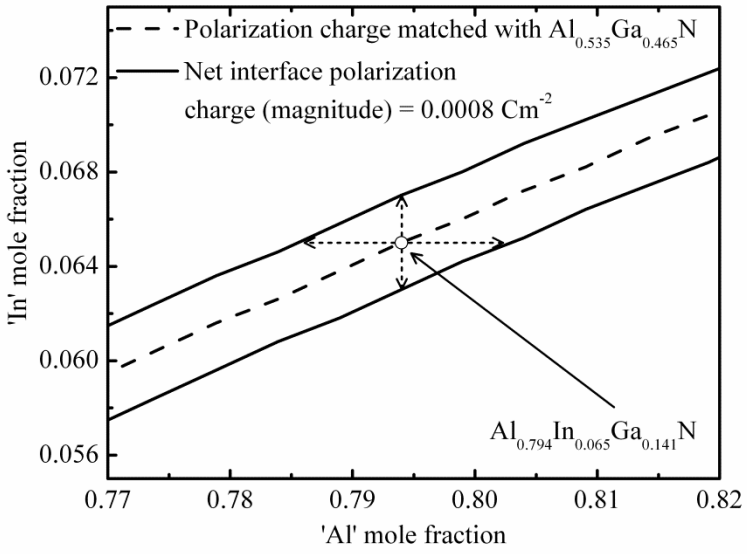

Figure 5.14: Contour of quaternaries with finite (0.0008 Cm^{-2}) net interface polarization charge together with the locus of polarization charge minimized quaternaries. Any quaternary composition inside the solid lines, will produce smaller net interface polarization charge (< 0.0008 Cm^{-2}) with $Al_{0.535}Ga_{0.465}N$.

CHAPTER 6

LATERAL CURRENT INJECTION DUV LD DESIGN USING REGROWN OHMIC CONTACTS

Simulation results of the LD structures presented in Chapter 4 and 5 assume that the waveguide and cladding layers are highly conductive. For the AlGaN based LD design of Chapter 5, our calculations considered both n- and p-type free carrier concentrations of 5×10^{18} cm^{-3} in the undepleted waveguide and cladding layers. We recognize that this level of free hole concentration may be difficult to achieve in practice at the present time. Weak electrical activation of the Mg dopant atoms leads to greater Joule heating in the resistive p-type layers. Besides, unscreened polarization charge at the interface between waveguide and EBL, as well as between spacer and QW layers contributes electrostatically to the emergence of parasitic hole blocking layers. To avoid these problems related to the vertical current injection designs, we have presented a lateral current injection (LCI) design in reference [140] for AlGaN DUV edge-emitting LDs on AlN substrates using polarization charge matched quaternary QWBs and regrown Ohmic contacts. Although the LCI LD design has already been proposed in the literature to be used as longer wavelength active sources in optoelectronic integrated circuits using GaInAsP/InP and related material systems [141], reference [140] presents the first theoretical demonstration that this approach is also feasible for UV LDs operating at sub-300 nm wavelengths in the III-N material system.

LCI LD designs significantly decouple the problem of electrical injection from that of optical confinement. Hence, thick layers of undoped wide bandgap materials may be used to form the optical waveguide of LCI LD designs for better optical confinement without disturbing lateral current flow from regrown p-contact through an undoped MQW active region toward regrown n-contact. Lateral interfaces between regrown

contacts and MQW active regions do not have any polarization charge because they are perpendicular to the growth axis for *c*-plane growths. As a consequence, unlike vertical injection designs, no artificial carrier blocking layer exists in the path of current flow. With polarization-charge-matched QWBs, a large number of QWs can be used in LCI designs, which not only enhances the optical confinement factor but also distributes Joule heating over a large volume. This is not a viable option for vertical injection design, because the bound carrier distributions rapidly become non-uniform among the various wells. Furthermore, there is some evidence that regrown Ohmic contacts offer certain advantages with respect to conventional alloyed Ohmic contacts [142]. Unlike ion implantation which requires high temperature annealing, regrowth of heavily doped III-V nitride Ohmic contacts can be done at relatively low temperature [143]. Besides, it offers a smooth transition from regrown Ohmic region to the as-grown epitaxial layers [144]. Unlike n-type AlGaN, regrowth of p-type AlGaN may be very difficult in the presence of incidental silicon delta doping at the regrowth interface [145], but this issue does not appear to be fundamental. Various approaches are reported in the literature to suppress Si spikes [145, 146].

6.1 Epitaxial Structure Design

To achieve minimum threshold current and maximum slope efficiency for an AlGaN/AlInGaN edge emitting LCI LD design, we have explored a rich design parameter subspace by means of numerical simulation and propose the epitaxial layer structure detailed in Table 6.1. It is assumed that all layers are pseudomorphically grown [120] on top of an AlN substrate. Good optical confinement is predicted by two-dimensional calculations for 500 μm edge emitting LD stripes formed by etching to a depth of 210 nm, or 150 nm above the top surface of the spacer, with lasing at $\lambda = 290$ nm. Ridge width is 2 μm and cavity length is 500 μm. Left and right facet reflectivities

are assumed to be 85% and 95% respectively (Mirror loss is 2.14 cm^{-1}). Though we considered ten optical modes (TE) in all simulations, only one mode (the 1st order mode) participated in lasing over the range of injection currents considered. The first four optical mode profiles are shown in Figure 6.1.

Table 6.1: Epitaxial layer structure for an AlGaN/AlInGaN edge emitting LCI LD design operating at 290 nm. Both p- and n-waveguiding layer compositions are graded to redistribute interfacial polarization charge over their entire thickness [120].

Layer Name	Material	Thickness (nm)	Refractive index
P-waveguiding	AlN	210	2.15
Grading	$Al_{0.79}In_{0.11}GaN$~AlN	150	2.2475 ~ 2.15
Spacer	$Al_{0.79}In_{0.11}GaN$	5.0	2.2475
QW (×20)	$Al_{0.30}GaN$	2.0	2.255
QWB (×20)	$Al_{0.79}In_{0.11}GaN$	5.0	2.2475
Grading	AlN~$Al_{0.79}In_{0.11}GaN$	150	2.15 ~ 2.2475
N-waveguiding	AlN	2000	2.15
Substrate	AlN	-	2.15

Refractive indices used for optical mode calculations are tabulated in Table 6.1, and are calculated from binary refractive indices [123] using Vegard's law. Neumann boundary conditions are applied to the left and right most vertical edges of the simulation domain to calculate the optical field. TM modes are neglected in all simulations because TE modes are dominant in compressively strained AlGaN based MQW LD designs [120, 131]. If there is any partial strain relaxation by lateral expansion due to a relatively large aspect ratio of the ridge, the optical gain of TE modes may be reduced, incurring a penalty to threshold current [120].

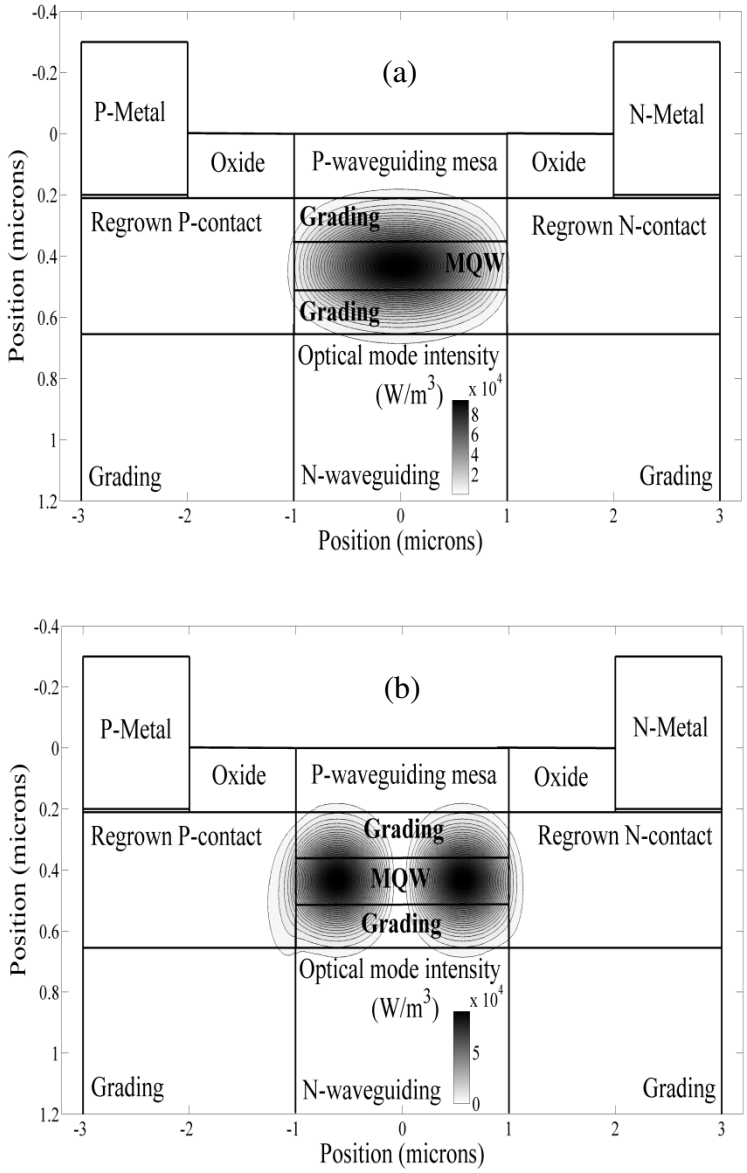

Figure 6.1: Optical mode profiles corresponding to the epitaxial structure of Table 6.1 (The first four TE modes are shown here). Only the first order mode (b) participated in lasing. Insufficient lateral refractive index contrast between regrown contacts and MQW active region fails to confine higher order modes (c) and (d) within the ridge width.

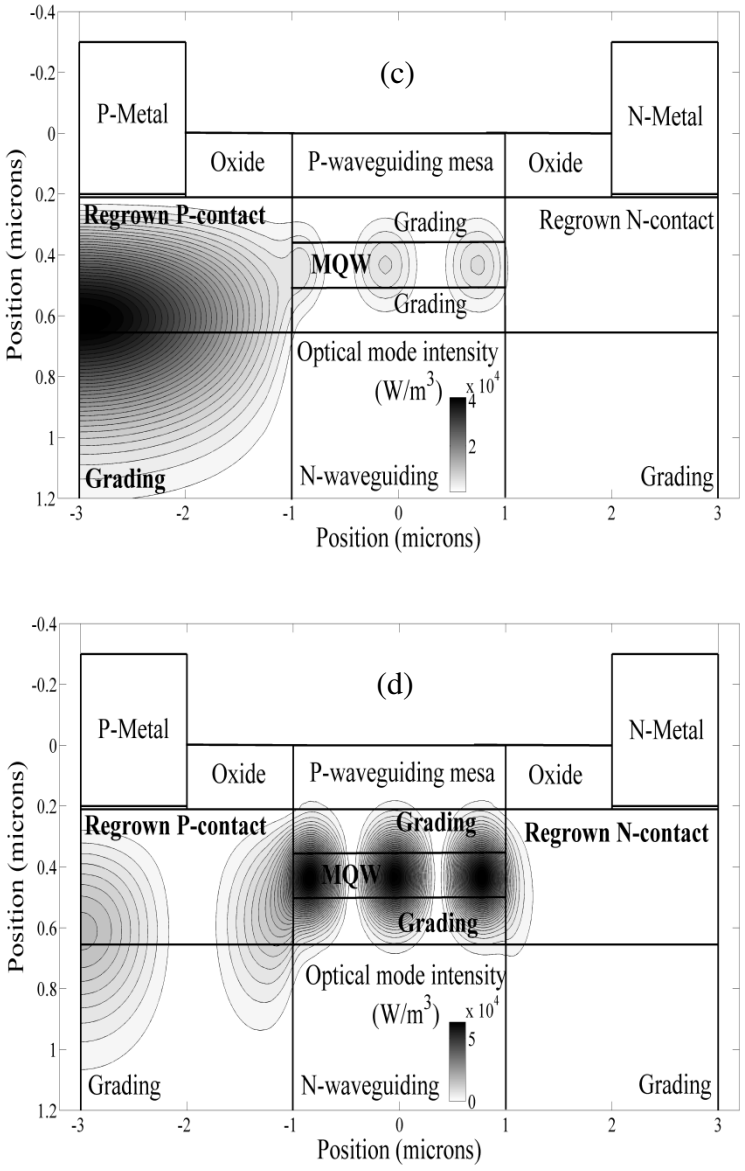

Figure 6.1 continued.

To estimate the effect of strain relaxation via lateral expansion, we have simulated our baseline design (Table 6.1) with different in-plane lattice constants. The effect of in-plane lattice constant on threshold current and lasing wavelength is illustrated in Figure 6.2, considering both TE and TM optical modes. Partially relaxed MQW active regions suffer from reduced TE optical gain due to lack of compressive strain. Both the threshold

current and the lasing wavelength have increased. In AlInN/AlInN LD designs [120], we found that if the compressive strain drops below 0.90%, the TM mode dominated the TE mode. But here, even with 100% strain relaxation (no compressive strain), it is still the TE mode which lases (instead of TM mode). In fact, it requires 0.80% tensile strain to switch from TE to TM mode. This is because the crystal field splitting energy, Δ_{cr} of $Al_{0.30}GaN$ is only -61.1 meV whereas that of AlN is -227 meV [8].

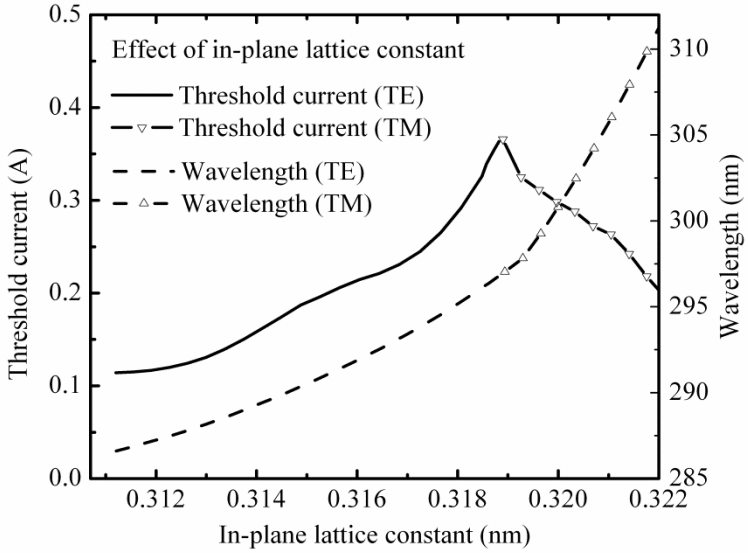

Figure 6.2: Effect of strain relaxation on threshold current and lasing wavelength. Partial strain relaxation increases the threshold current by reducing the optical gain of TE modes.

6.2 Effect of Optical Loss

Optical loss in metals plays a vital role in determining the lasing mode(s) because it modifies the modal losses associated with optical modes. Nickel and aluminum are considered as the p- and n-metals, respectively. At λ = 290 nm, the absorption coefficient

of nickel is 8.77×10^5 cm^{-1} and that of aluminum is 1.49×10^6 cm^{-1} [90]. Total optical loss in metals for the lasing mode of Figure 6.1 is 0.014 cm^{-1}. Higher order modes have significantly greater optical loss (> 8 cm^{-1}). Ternary AlGaN with 55% Al or more is assumed optically non-absorbing at λ = 290 nm and no other background optical loss is considered in our simulations. To estimate the absorption coefficient of AlGaN, a composition, strain and wavelength dependent complex refractive index model is used [8, 33]. But, the parameters used in the model are extracted from undoped bulk samples. So, Mg doped p-type AlGaN may exhibit sub-bandgap absorption. At this moment, there is no model to quantify this absorption coefficient at the wavelength of our interest but this can be qualitatively incorporated in all simulation results with the introduction of phenomenological distributed optical loss. Figure 6.3 illustrates the energy band diagrams and carrier densities, at equilibrium as well as at a bias condition above the lasing threshold. L-I and V-I curves are shown in Figure 6.4. With no additional optical loss, the threshold current is 114 mA and the slope efficiency is 2.77 W/A. Figure 6.5 shows the degradation of baseline LD performance (threshold current and slope efficiency) as a function of additional optical loss. For example, an additional loss of 10 cm^{-1} significantly degrades slope efficiency (~ 0.5 W/A) but only slightly increases threshold current (~ 126 mA). The slope efficiency of an edge-emitting laser is directly proportional to the ratio of the mirror loss to the total loss [147], where the total loss is the summation of the mirror loss and the internal losses. If the internal losses are significantly larger than the mirror loss, the slope efficiency exhibits a $^1/_{loss}$ behavior (see Figure 6.5). Shockley–Read–Hall lifetime and Auger recombination coefficients are taken from [109] and [148] respectively. It is our finding that the former (SRH) exerts considerably greater influence on threshold current than the latter (Auger). Other parameters used in our calculations have been previously reported [120, 131].

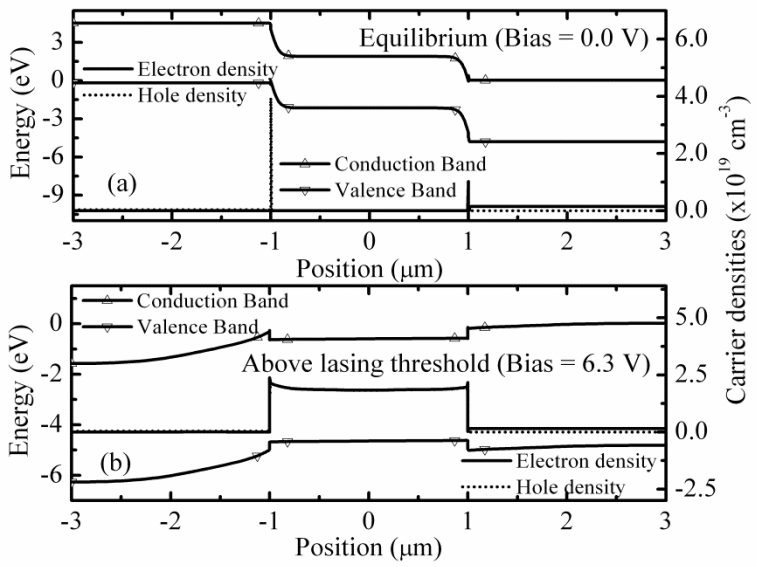

Figure 6.3: Energy band diagrams and carrier densities (a) at equilibrium and (b) above the lasing threshold.

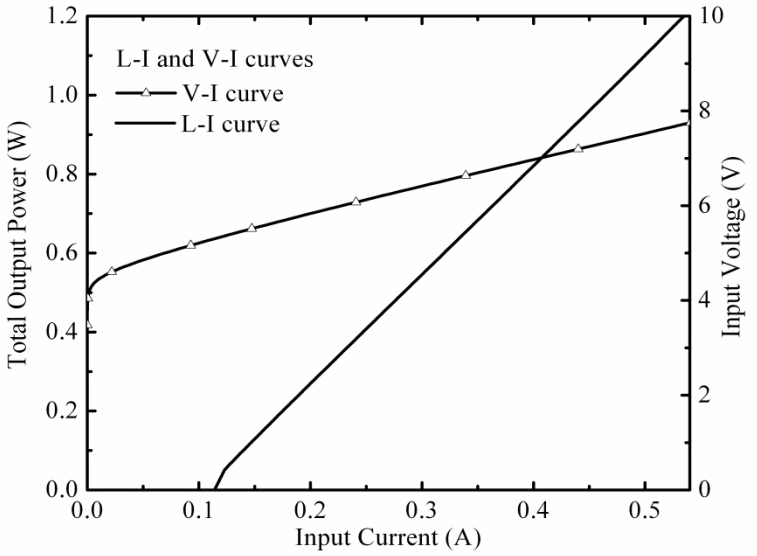

Figure 6.4: L-I curve and V-I curve of the epitaxial structure of Table 6.1.

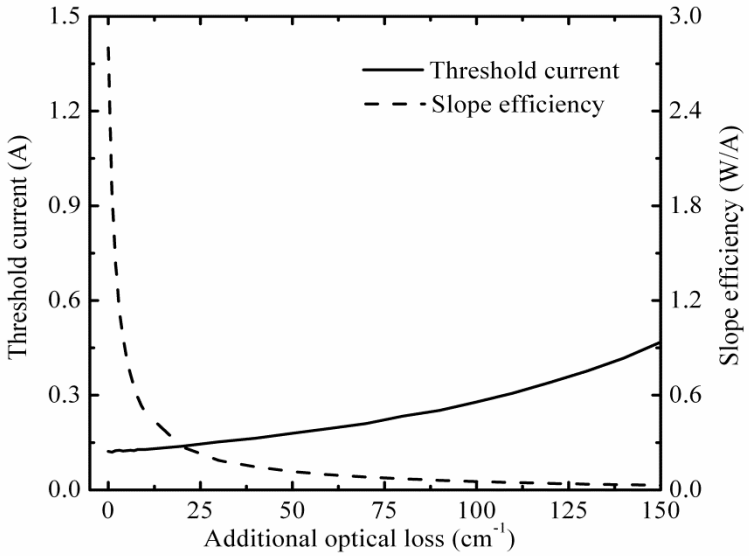

Figure 6.5: Effect of additional optical loss on threshold current and slope efficiency. Sub-bandgap absorption loss may degrade slope efficiency significantly.

6.3 Regrown Contact Layers

The entire epitaxial structure, with the exception of the regrown contacts, is assumed undoped to ensure that current flows laterally through the narrow bandgap QWs only. Furthermore, an undoped epitaxial structure may offer reduced defect density, which will increase Shockley–Read–Hall lifetimes, improving both threshold current and quantum efficiency. The bandgap of the regrown Ohmic contacts should be sufficiently larger than that of the QWs to block the leakage of carriers from the active region, as well as assist in lateral optical confinement through their lower refractive index. The substitutional dopant (Si) concentration of the $Al_{0.60}GaN$ regrown n-contact was taken to be 2×10^{18} cm^{-3}. The valence band discontinuity, ΔE_v at the regrown n-contact/QW interface is 340 meV.

Choosing appropriate and optimized material composition for the regrown p-contact is vital for LCI LD designs in the III-V nitride material system. To achieve lasing at 290 nm, it must have an Al mole fraction greater than 30% to effectively block the leakage of electrons from the active region. Further increasing the Al composition, the conduction band discontinuity will increase (which is necessary to block electrons) but the p-type conductivity will degrade because of higher Mg activation energy. With decreasing Al mole fraction, the exact opposite happens. Electrons leak from the active region and reach the regrown p-contact, where they recombine non-radiatively. Moreover, the optical mode(s) may shift toward the regrown p-contacts. In the present design, $Al_{0.55}GaN$ was determined to be the optimal material choice for the regrown p-contact, and a substitutional dopant (Mg) concentration of 3×10^{19} cm^{-3} has been assumed. The conduction band discontinuity, ΔE_c at the regrown p-contact/QW interface is 371 meV.

6.4 Lateral Confinement of Higher Order Modes

Although the fundamental and the first order modes are confined within the active region, the refractive index asymmetry between the n and p regrown contact layers causes the higher order modes to leak out of the active region and to become asymmetric. They leak out toward the regrown p-contact layer because the chosen material ($Al_{0.55}GaN$) does not offer sufficient index contrast for the higher order modes. Wide bandgap regrown contact layers can provide more index contrast and confine the higher order modes. Figure 6.6 shows the first four optical modes simulated on a modified baseline design where both the p and n regrown contact layer's compositions are assumed to be $Al_{0.80}GaN$. Such a design is not a viable option because the wide bandgap regrown layers will be barely conductive.

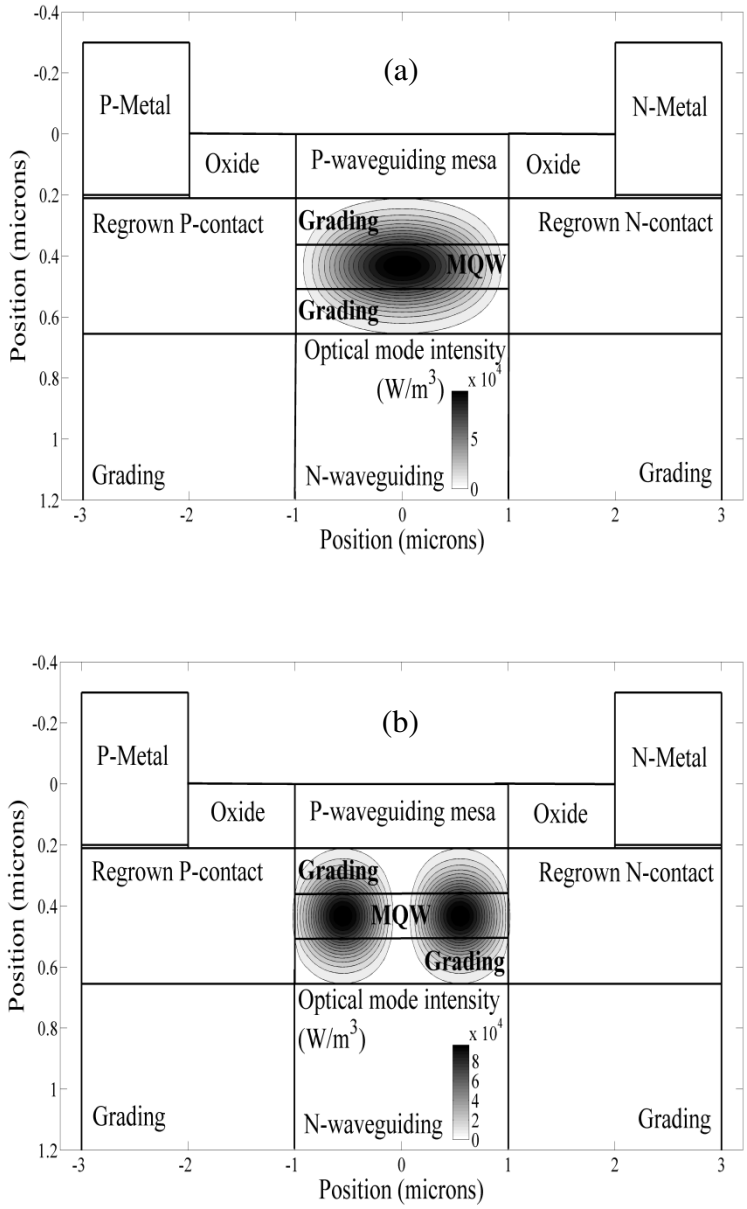

Figure 6.6: Optical modes corresponding to a hypothetical structure. These profiles demonstrate that wide bandgap regrown contact layers can confine higher order modes (c) and (d). But this design is not feasible because of conductivity considerations.

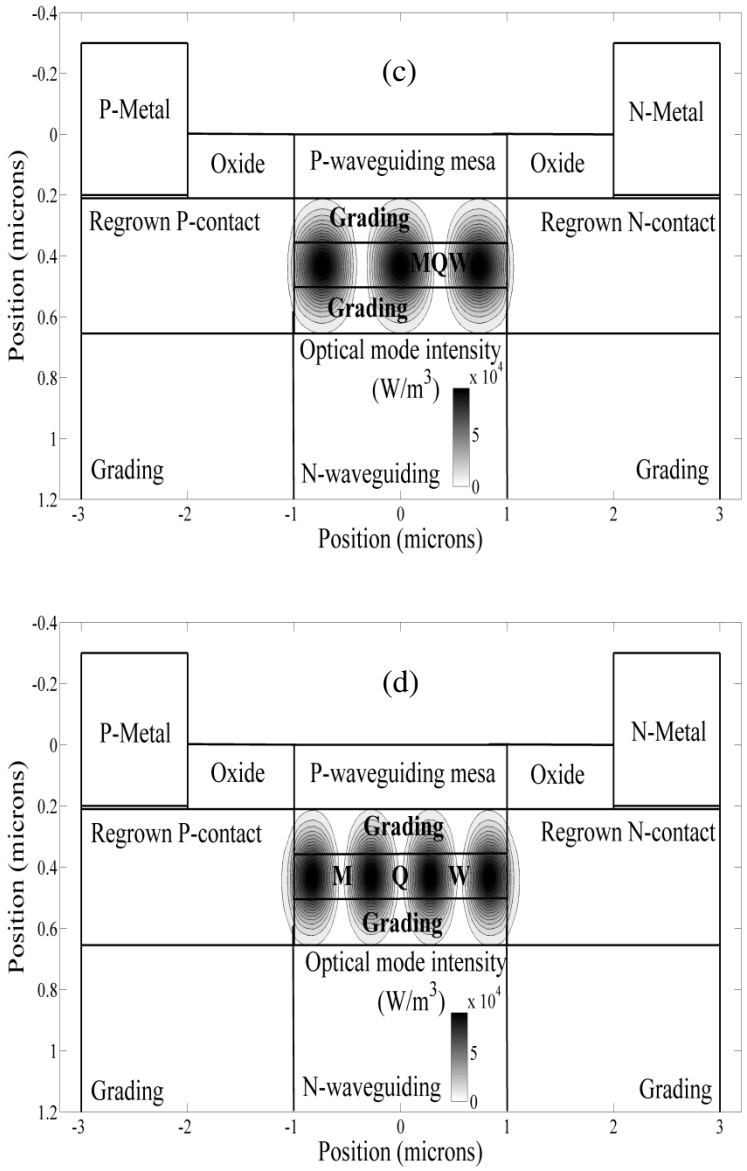

Figure 6.6 continued.

6.5 Polarization Charge Matching and Number of QWs

Grading is applied at the bottom of the regrown contacts to redistribute polarization charge volumetrically and to prevent the formation of a parasitic lateral current leakage path. Similarly, grading is used on top of the N-waveguide layer and

below the P-waveguide layer to eliminate parasitic channels and to ensure uniform distribution of carriers from the top QW to the bottom one. $Al_{0.79}In_{0.11}GaN$ (used for the QWB) has the largest bandgap and it is polarization charge matched to $Al_{0.30}GaN$ (used for the QW). Polarization charge matching both reinforces uniform carrier distribution vertically among the QWs, and reduces electron and hole wavefunction separation. The wide bandgap of the QWBs ensures that current flows laterally through the QWs only. Because of this and minimized non-radiative recombination rates at the regrown contacts, injection efficiency is expected to be high. One particular advantage of the LCI LD design over vertical injection designs is that it can support a larger number of QWs [149-151] without introducing significant non-uniformity in the carrier distribution among the wells. However, in a design employing too many QWs, the total thickness of an active region grown on top of an N-waveguide layer may exceed the critical thickness for pseudomorphic growth, and those QWs at the top of the structure may suffer from reduced TE optical gain due to lack of compressive strain [120]. On the other hand, the threshold current density will be higher in LCI LD designs using only a few QWs. Regardless of the number of QWs, the lateral carrier distribution inside the wells may become non-uniform above the lasing threshold (see Figure 6.3). This can be attributed to the disparity of electron and hole mobilities [152]. Above the lasing threshold it is observed that carrier densities exhibit a lateral peak at the interfaces with regrown Ohmic contacts [149] (see Figure 6.3). Like the lasing mode of Figure 6.1, the stimulated emission profile (not shown here) also peaks close to these interfaces, with reduced emission in the middle of the active region [152]. This is why the 1st order mode (total two lobes and both of them inside the active region) lased instead of the fundamental mode because the 1st order mode is pumped more efficiently.

6.6 Threshold Current Density and Joule Heating

The threshold current density of the proposed design is calculated to be 157 kA/cm^2. To estimate this threshold current density, the lateral cross-section of the entire MQW stack has been considered. In the literature, a cross-sectional area of ridge width and cavity length is used to normalize threshold current [153] which is not correct for LCI type LDs [154]. A simple prescription for decreasing threshold current density in LCI designs is to use thicker QWBs. However, care must be taken to ensure that the optical confinement factor is not degraded by a large margin, and the critical thickness for pseudomorphic growth is not exceeded by the active region. Thicker QW designs demand more threshold current for population inversion. During lasing more voltage is dropped laterally across the regrown p-contact than any other region because of its moderate p-type conductivity. This in turn may reduce the effectiveness of the conduction band offset to block electrons. Also, the lasing wavelength increases with the thickness of QWs.

One major disadvantage of the LCI LD design is that a large current must flow through a small lateral cross-section of the active region. In a vertical injection design, current flows instead through the larger cross-sectional area of the mesa. However, with the help of a large number of QWs, Joule heating (P_{heat}) may be distributed over a larger volume in an LCI design, reducing the average temperature. The temperature difference between the active region and the heat sink can be estimated with the expression $\Delta T = R_{th} \times P_{heat}$ where R_{th} is the thermal resistance [33]. At an injection current level of 150 mA, ΔT is approximately 52 K assuming that R_{th} = 75 K/W. Based on this rough estimate, it can be concluded that the design presented in Table 6.1 may be operated in CW mode instead of pulsed mode.

CHAPTER 7

INVERSE TAPERED P-WAVEGUIDE FOR EFFICIENT HOLE TRANSPORT

In the previous chapters, we have presented AlInN/AlInN [120] and AlGaN/AlInGaN [131] edge emitting vertical injection LD designs operating at 250 nm wavelength. These investigations revealed that compositionally graded EBLs [120] and polarization charge matched quantum well barriers (QWBs) [131] can significantly improve LD performance. Although AlInN and AlInGaN based designs may offer promising LD performance advantages, high quality crystal growth of In-rich materials is presently considered more challenging. In this chapter, we tried to improve hole injection through electrostatic engineering of the hole injection layers. We have presented a 290 nm UV edge emitting vertical injection LD design in reference [155] based exclusively on metal-face growth of ternary AlGaN layers on a bulk *c*-axis AlN substrate. In contrast to the designs presented in Chapter 4 and 5, the epitaxial layer structure of Table 7.1 exhibits some new features. It only employs ternary AlGaN compositions and avoids ternary AlInN and quaternary AlInGaN. As a consequence of design innovations that bring substantial net benefit, the optical mode profile of devices presented here is no longer centered on the active region. Instead, it is pushed away from the highly absorptive p-Ohmic metal to minimize the optical absorption loss.

In order to reduce the problem of hole injection, several EBL designs are investigated and compared via numerical simulation. Simulation results suggest that superior hole injection can be achieved if a conventionally tapered EBL [65-68, 120, 131] is replaced by an inverse tapered p-waveguide layer whose bandgap decreases along the growth direction. This inverse tapering eliminates the electrostatically induced artificial hole blocking layer in conventionally tapered EBL design, and leads to significantly

lower threshold current. The design presented here assumes realistic chemical and electrical concentrations of dopant atoms for all p-type layers, and uses only ternary AlGaN mole compositions that are feasible with current growth technology. Simulation results presented here consider the composition-dependence of dopant activation energy [74, 75, 156, 157], even in graded material, for accurate calculation of incomplete ionization of dopant species [76] throughout the epitaxial layer structure. The complexity introduced by this ionization model is critical for the accurate prediction of hole injection. Also, a composition, strain and wavelength dependent complex refractive index model [8, 33] has been used to calculate optical modes and absorption coefficients (and loss) of ternary AlGaN epitaxial layers at the emission wavelength. LD designs targeting shorter emission wavelengths (< 290 nm) can easily adopt this idea of inverse tapering and thereby eliminate the severe problem of hole injection.

7.1 Epitaxial Structure Design

To achieve superior hole injection efficiency and minimum optical loss in the p-Ohmic metal, we have explored different p-waveguide layer and EBL designs by means of numerical simulation. Table 7.1 lists the epitaxial layer structure of a typical AlGaN/AlGaN edge emitting vertical injection LD design with a conventionally tapered EBL. It is assumed that all layers are pseudomorphically grown [120, 131] on top of an AlN substrate. 500 μm edge emitting LD stripes are formed by etching to a depth of 310 nm, or 220 nm above the top surface of the spacer, with lasing at λ = 290 nm. The ridge width is 2 μm and cavity length is 500 μm. Left and right facet reflectivities are assumed to be 85% and 95% respectively (Mirror loss is 2.14 cm^{-1}). We have considered several TE and TM modes in all simulations, and confirmed that only the fundamental modes are strongly confined by the optical waveguide. Of the two fundamental modes, lasing occurs only in the TE mode over the range of injection currents we have studied, as is

expected in compressively strained AlGaN based MQW LD designs [120, 131]. Its optical mode profile is shown in Figure 7.1. Refractive indices used for optical mode calculations are presented in Table 7.1, and are estimated from the real part of a complex refractive index model [8, 33]. The imaginary part of this model is used to estimate the absorption coefficients in the epitaxial layers. The entire epitaxial structure of Table 7.1 is assumed optically transparent at the emission wavelength (290 nm).

Table 7.1: Epitaxial layer structure for an AlGaN/AlGaN edge emitting vertical injection LD design operating at 290 nm.

Layer Name	Material	Thickness (nm)	Refractive index
Contact	GaN	10	2.603
p-waveguide	$Al_{0.48}GaN$	500	2.624
EBL	$Al_{0.54 - 0.60}GaN$	20	2.565 - 2.522
Spacer	$Al_{0.54}GaN$	5.0	2.565
QW (×2)	$Al_{0.34}GaN$	2.0	2.741
QWB (×2)	$Al_{0.54}GaN$	5.0	2.565
Grading	$Al_{0.45 - 0.54}GaN$	20	2.662 - 2.565
n-waveguide	$Al_{0.45}GaN$	150	2.662
Grading	$Al_{0.70 - 0.45}GaN$	400	2.46 - 2.662
Buffer	$Al_{1.00 - 0.70}GaN$	1000	2.292 - 2.46
Substrate	AlN	-	2.292

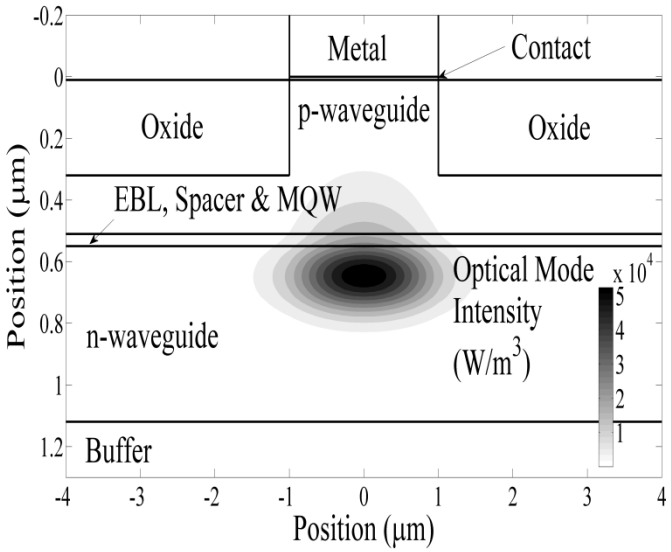

Figure 7.1: Optical mode profile corresponding to the epitaxial structure of Table 7.1 (Only the lasing TE mode is shown here).

Optical loss in metals plays a critical role in determining the threshold current. For purposes of our numerical calculation, the p- and n-Ohmic metals are taken to be nickel and aluminum, respectively. At λ = 290 nm, the absorption coefficient of nickel is 8.77×10^5 cm^{-1} and that of aluminum is 1.49×10^6 cm^{-1} [90], resulting in a total optical loss of 2.4 cm^{-1} in the metals for the lasing mode of Figure 7.1. Figure 7.2 illustrates the energy band diagram at a bias condition below the lasing threshold. L-I and V-I curves are shown in Figure 7.3. The threshold current is 715 mA and the slope efficiency is 0.08 W/A. Shockley–Read–Hall lifetime and Auger recombination coefficients are taken from [109] and [148], respectively. Other parameters used in our calculations have been previously reported [120, 131].

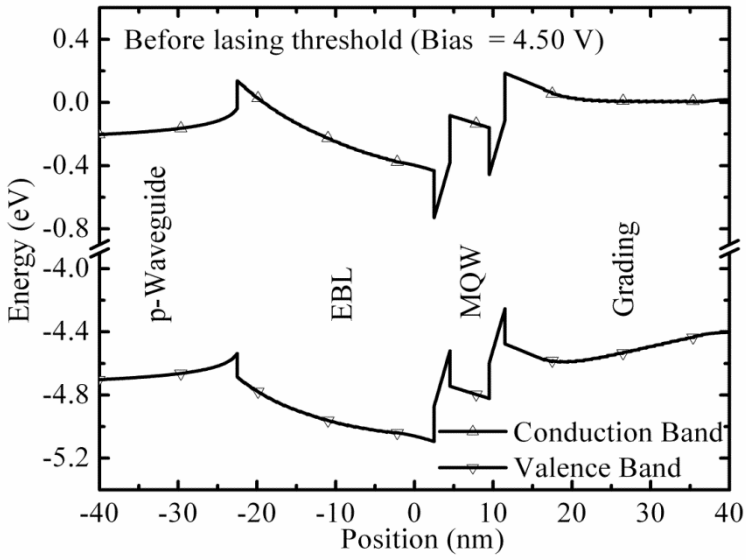

Figure 7.2: Energy band diagram of the epitaxial structure of Table 7.1 at a bias before the lasing threshold. Conventionally tapered EBL is also acting as a significant hole blocking layer (Barrier height is 0.6 eV).

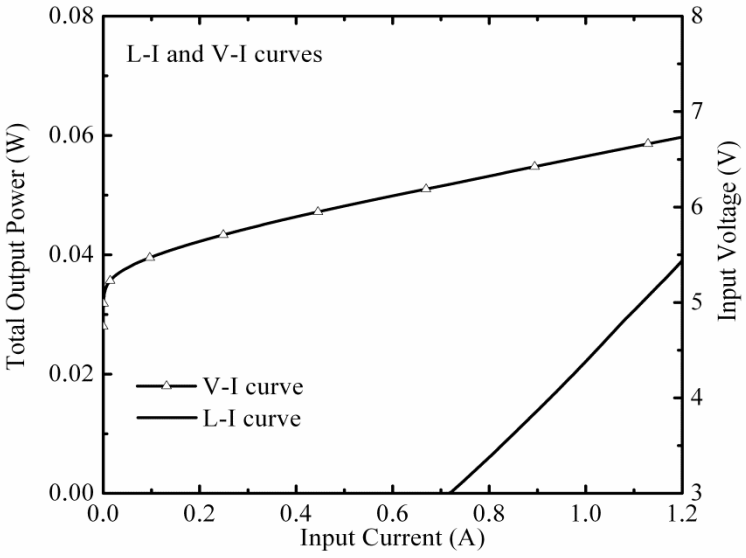

Figure 7.3: L-I and V-I curve of the epitaxial structure of Table 7.1.

In contrast to previously reported designs [120, 131] presented in Chapter 4 and 5, the epitaxial layer structure of Table 7.1 exhibits several new features. It only employs ternary AlGaN compositions and avoids ternary AlInN and quaternary AlInGaN. Although AlInN and AlInGaN based designs may offer promising LD performance advantages [120, 131], high quality crystal growth of In-rich materials is presently considered more challenging. In order to achieve higher p-type conductivity, narrow bandgap $Al_{0.48}GaN$ (E_{gap} = 4.58 eV) is utilized for the p-waveguide layer. Wider bandgap material would incur greater Joule heating because of poor p-type conductivity. On the other hand, narrow bandgap p-waveguide material may become optically absorptive at the lasing wavelength, and will moreover exacerbate optical losses by pulling the optical mode toward the highly absorptive p-Ohmic metal. Similarly, a thinner p-waveguide layer would yield higher optical loss, while a thicker layer would introduce additional series resistance and associated Joule heating. In contrast to previously reported designs [120, 131], the optical mode profile of the structure presented in Table 7.1 is no longer centered on the active region (see Figure 7.1). A narrow bandgap ($Al_{0.45}GaN$) n-waveguide layer is employed to counterbalance the high refractive index of the proposed p-waveguide layer, and to pull the optical mode downwards, away from the lossy p-Ohmic metal. In fact, $Al_{0.45}GaN$ (used for n-waveguide layer) is the smallest possible bandgap material which is transparent at the 290 nm emission wavelength. Thicker and narrower bandgap n-waveguide material may reduce lateral series resistance (and Joule heating) but it would significantly degrade the optical confinement factor and may also introduce additional optical absorption. Furthermore, a thinner and/or wider AlGaN n-waveguide layer may not be able to pull the optical mode downwards effectively if thinner and wider bandgap AlGaN is employed. Figure 7.4 illustrates the effects of waveguide's composition and thickness on threshold current, optical absorption loss in the metal and optical confinement factor. The exhaustive study presented in Figure 7.4

helped us to optimize the waveguide design. The optical confinement factor for the structure presented in Table 7.1 is calculated to be 0.75%.

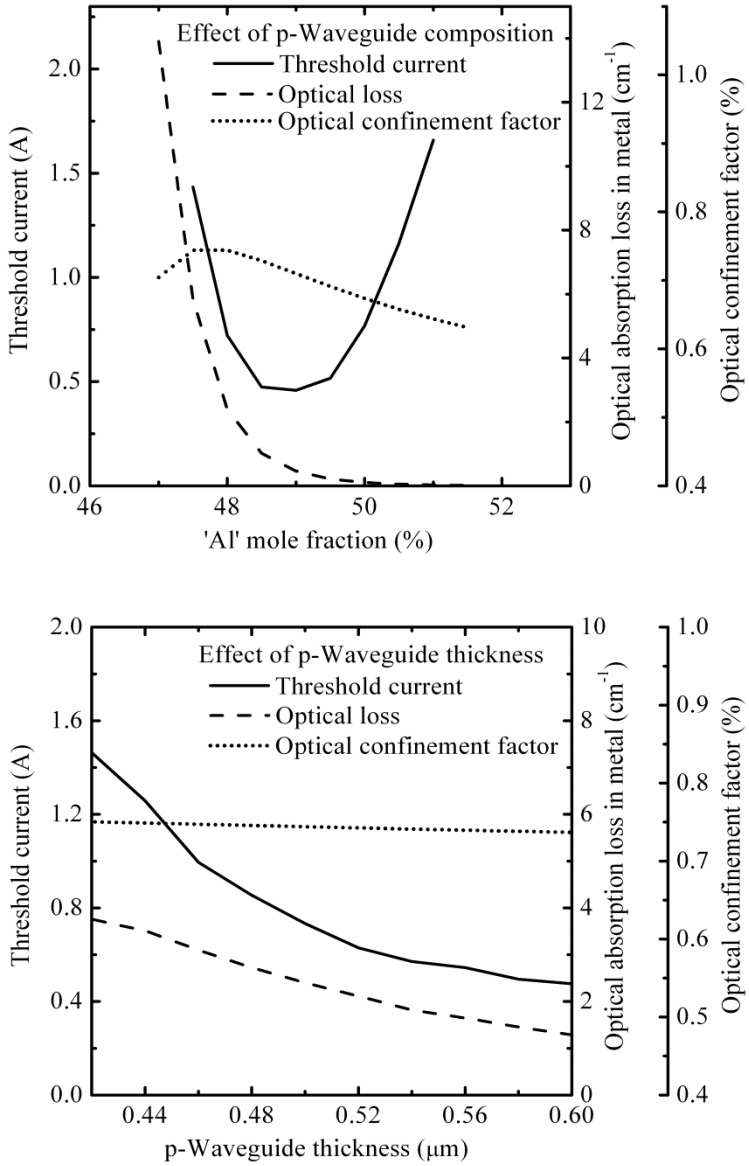

Figure 7.4: Effect of p- and n- waveguide's composition and thickness on threshold current, optical absorption loss in metal and optical confinement factor.

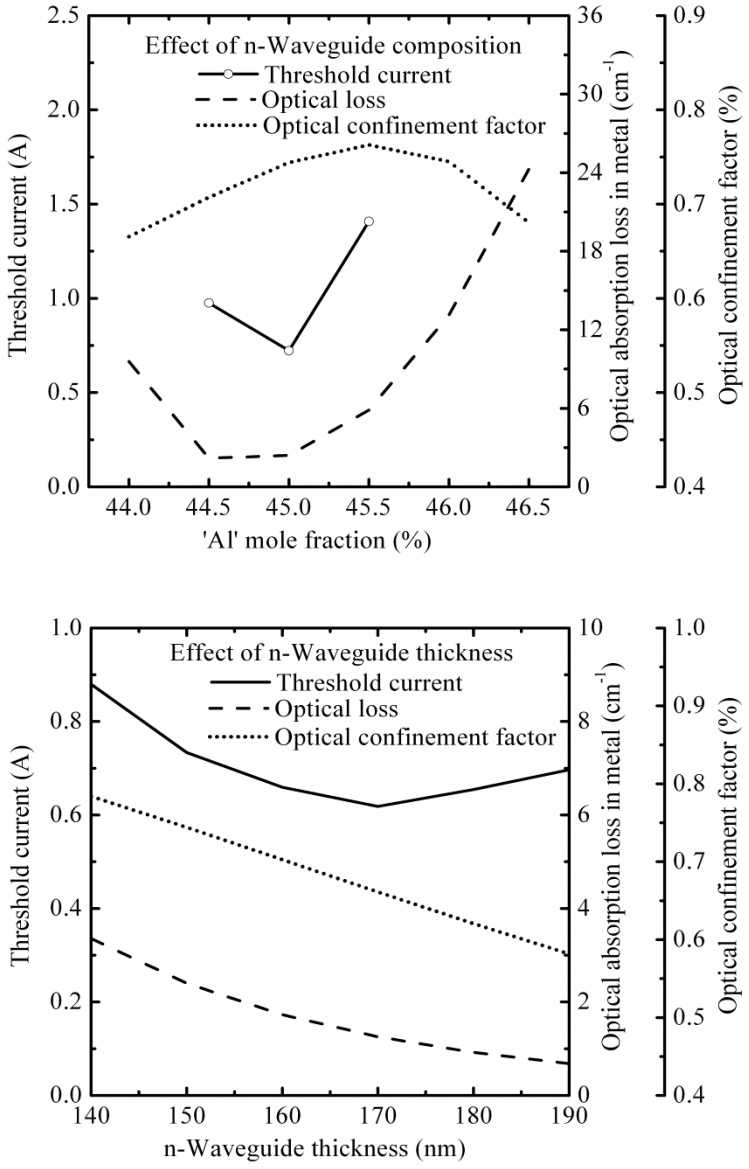

Figure 7.4 continued.

From the energy band diagram of Figure 7.2, one may observe that a conventionally tapered EBL (in which the bandgap increases along the growth direction) acts as a large hole blocking layer primarily due to the unscreened polarization charge at the p-waveguide layer/EBL and spacer/QW interfaces. The substitutional dopant (Mg) concentration of the spacer, EBL and p-waveguide layer is taken to be 10^{18} cm^{-3} (For the

n-waveguide layer, the substitutional Si concentration is assumed to be 2×10^{18} cm^{-3}). We point out that the prominence of this hole blocking layer will be artificially but only partially masked if 100% ionization of dopant atoms is assumed; however, this is not only incorrect, but also leads to a gross overestimate of hole injection efficiency. One way to reduce the potential barrier for hole injection is to dope the p-type layers heavily. Figure 7.5 shows the effect of heavy Mg doping on the energy band diagram. As expected, the barrier height of the hole blocking layer is reduced significantly. Both threshold current and voltage are lowered due to improved hole injection efficiency (see Figure 7.6).

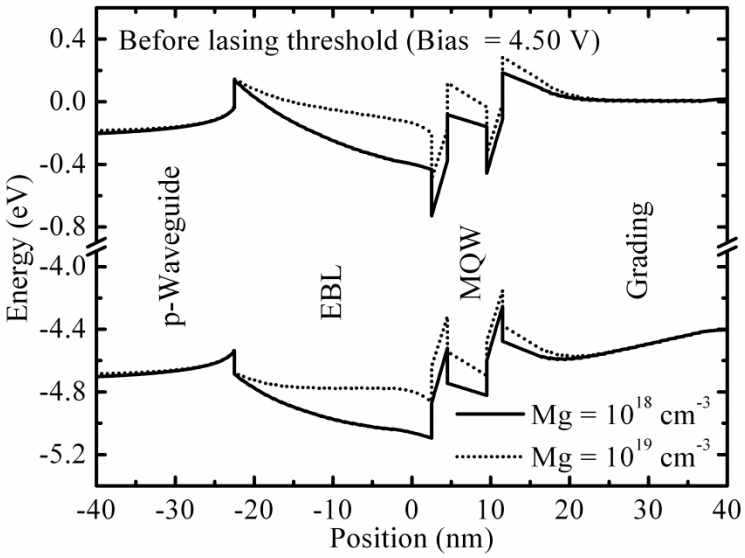

Figure 7.5: Effect of heavy Mg doping on the energy band diagram of the epitaxial structure of Table 7.1. Hole blocking layer is suppressed significantly.

Although heavy doping degrades carrier mobility [77, 158, 159], this effect alone does not exert a large influence on either threshold current or voltage. Instead, it is the energetic barrier to hole injection due to the valence band discontinuity at the p-

waveguide layer/EBL interface with conventional tapering which is the dominant effect, limiting the mechanism for hole injection to mere thermionic emission.

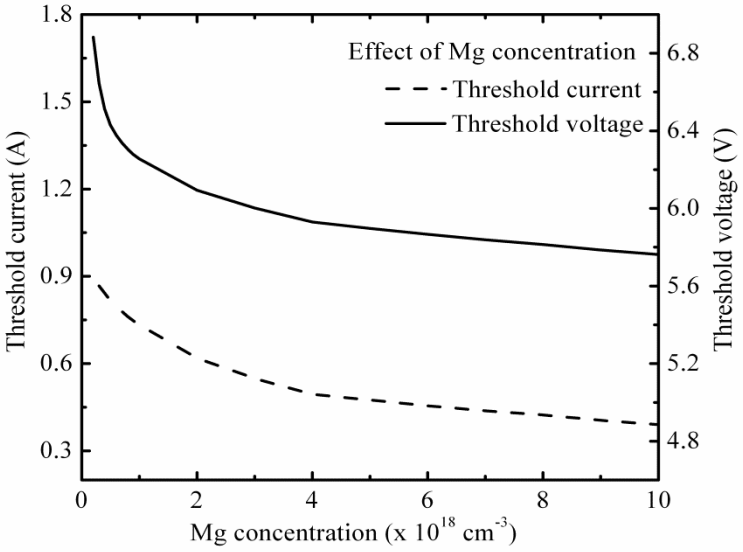

Figure 7.6: Both threshold current and voltage improve with heavy doping of p-type layers. But the improvements may be exaggerated because mobility degradation has not been considered explicitly.

7.2 Two-step Tapered EBL Design

The abrupt valence band discontinuity at the p-waveguide layer/EBL interface can be eliminated by using an EBL with two step tapering. Specifically, the bottom half of the EBL may be tapered upwards such that its bandgap increases in the growth direction (from $Al_{0.54}GaN$ to $Al_{0.60}GaN$) for efficient electron blocking. The upper half may be tapered downwards along the direction of growth (from $Al_{0.60}GaN$ to $Al_{0.48}GaN$) to eliminate abrupt valence band discontinuities. We have simulated the baseline epitaxial structure of Table 7.1 by replacing the conventionally tapered EBL with the proposed two step tapered design, and the results are shown in Figure 7.7 and 7.8. For meaningful

comparison, the EBL thickness is held constant at 20 nm. Two step tapering of the EBL yields a 46% reduction in threshold current and 76% improvement in slope efficiency (see Figure 7.8). Unfortunately, the band diagram of Figure 7.7 clearly indicates that the two step tapered EBL does not reduce the size of the potential barrier to hole injection, but merely halves its effective thickness and eliminates the abrupt valence band offset. To improve the hole injection efficiency further, it is important to investigate and understand the nature of this polarization charge induced hole blocking layer in more detail.

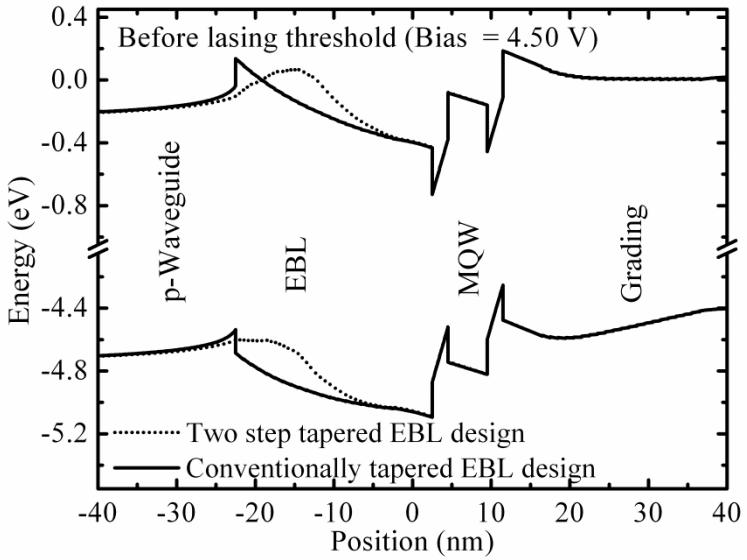

Figure 7.7: Comparison of the energy band diagrams between conventionally tapered and two step tapered EBL designs. Two step tapering eliminates the abrupt valence band offset at the P-waveguide layer/EBL interface and reduces the effective thickness of the hole blocking layer.

The sign and magnitude of the net interface polarization charge of an $Al_xGa_{1-x}N/Al_yGa_{1-y}N$ interface depends on several factors, including growth axis, metal-face vs. N-face growth, difference between mole fraction x and y and their relative significance [8]. In our simulation, metal-face *c*-axis growth is assumed. It is obvious that a large mole fraction contrast will increase the magnitude of the net interface charge, but it is the sign

of the difference between x and y which determines the sign of the polarization charge. If we assume that a layer of $Al_xGa_{1-x}N$ is grown on top of $Al_yGa_{1-y}N$, the net interface polarization charge will be positive if x > y and vice versa (see Figure 7.9). Therefore, the volumetrically redistributed polarization charge of the two step tapered EBL is positive in the bottom half and negative in the upper half. With moderate dopant (Mg) concentration in the p-type layers (10^{18} cm^{-3}), this redistributed polarization charge opposes the bound charges associated with dopant atoms at the bottom half of EBL and reinforces at the top.

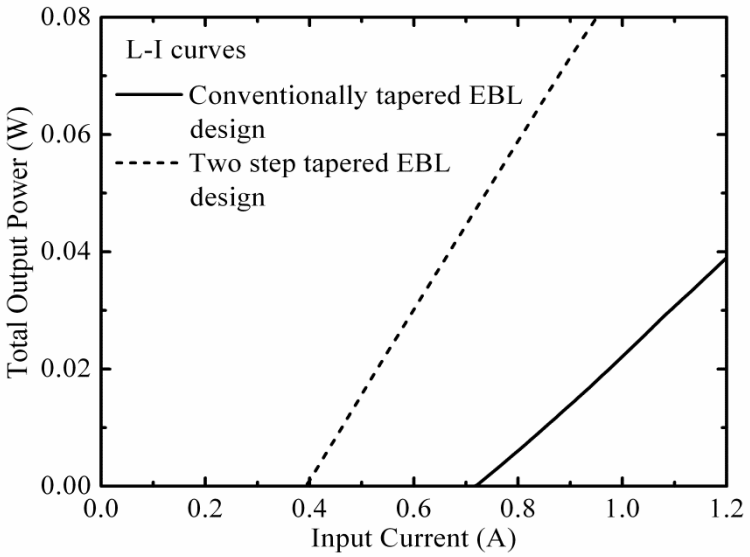

Figure 7.8: Comparison of L-I curves between conventionally tapered and two step tapered EBL designs. With two step tapering, threshold current is reduced by 46% and slope efficiency is improved by 76%.

In cases where the magnitude of the redistributed polarization charge in the lower half of the EBL exceeds the charge of electrically active dopant atoms in that layer, the location of the p-n junction itself is transferred to the interface between the two halves of the EBL. This explains why the effective thickness of the hole blocking layer is halved in a two step tapered EBL design. Because the volumetric redistribution of polarization charge in the upper half contributes additively to the fixed charge contributed by ionized Mg atoms,

the potential drop over the EBL layer is primarily across the bottom half, while the valence band is almost flat throughout the upper half (see Figure 7.7).

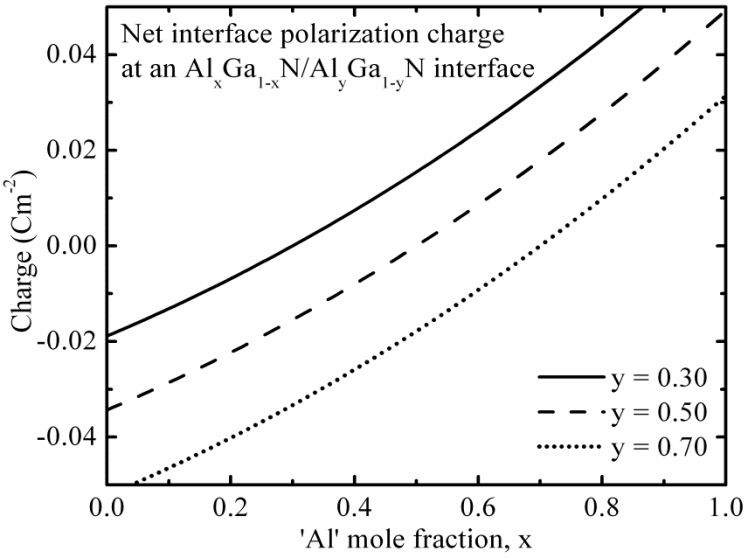

Figure 7.9: Compositional dependence of the net interface polarization charge at an AlGaN/AlGaN interface. It is assumed that the layers are pseudomorphically grown on top of AlN substrate.

7.3 Inverse Tapered p-Waveguide Design

Now that the root cause of the hole blocking layer has been identified, the next step is to address strategies for its suppression. One such approach is to flip the sign of the polarization charge at the bottom half of two step tapered EBL, in such a way that the redistributed polarization charge should be negative throughout the entire thickness of the EBL. From a compositional perspective, this means that the two step tapered EBL should be replaced by an inverse tapered p-waveguide layer where the bandgap should decrease along the growth direction. This may be a risky proposition, as electrons may leak from

the MQW active region in the absence of an explicit EBL, and thereby degrade LD performance. However, in spite of the band diagram under flatband conditions, our numerical simulations reveal that above the lasing threshold, neither the conventional nor the two step tapered EBL are effective in blocking electrons anyway, due to the redistribution of electrostatic potential under strong forward bias. Indeed, because of poor p-type conductivity, a large fraction of the applied voltage is dropped across the EBL. This point is demonstrated in Figure 7.10. Above the lasing threshold, the conduction band is almost flat at the bottom half of the two step tapered EBL, and the only thing impeding the leakage of electrons is the conduction band offset at the spacer/QW interface.

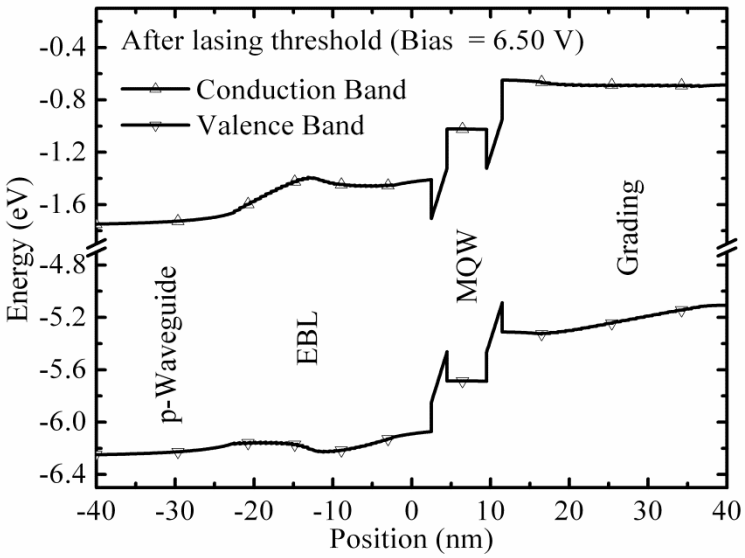

Figure 7.10: Energy band diagram of the two step tapered EBL design above lasing threshold. A sufficient fraction of the applied voltage drops across the EBL and to make the conduction band almost flat.

Nevertheless, in spite of electron leakage, numerical simulations indicate that this device can be made to lase, albeit at high injection current density. This observation suggests that the inverse tapering efficacy in DUV LD design may actually solve the problem of poor hole injection. Still, care must be taken to keep the electron leakage within tolerable limits via appropriate selection of MQW (and spacer) material compositions.

We therefore modify baseline design of Table 7.1 by replacing the tapered EBL with an inverse tapered p-waveguide layer (from $Al_{0.54}GaN$ to $Al_{0.48}GaN$). Inverse tapering is affected over a thickness of 20 nm, with all other quantities unchanged. Simulation results show that the parasitic electrostatic barrier to hole injection is suppressed significantly (see Figure 7.11). Excellent hole injection efficiency leads to the dramatic improvement in LD performance shown in Figure 7.12.

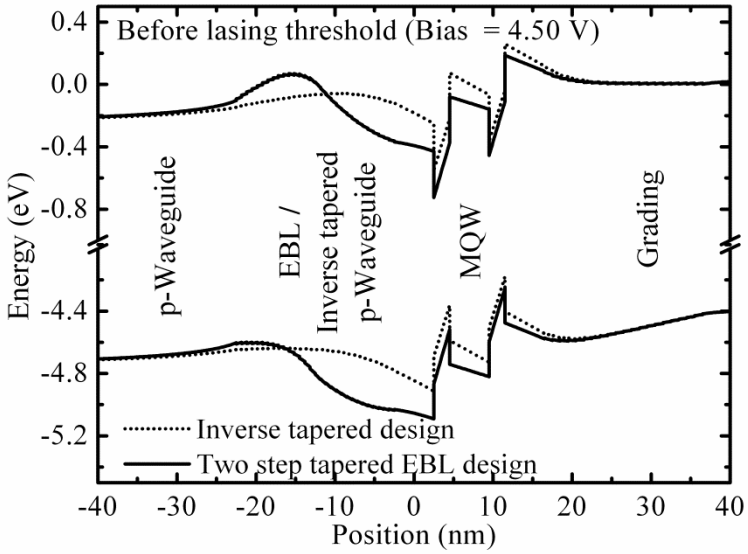

Figure 7.11: Comparison of the energy band diagrams between two step tapered EBL and inverse tapered designs. Inverse tapering reduces the potential barrier of the hole blocking layer by 180 meV.

The L-I characteristic of two step tapered EBL design is included for comparison. The proposed inverse tapered design's threshold current is reduced by 33% and slope efficiency is improved by 14% with respect to the two step tapered EBL design. Threshold voltage is also reduced by 0.4 V (results not shown here). As there is no explicit EBL in the inverse tapered design, leakage of electrons from the active region can only be kept within acceptable limits if MQW and spacer compositions are chosen judiciously. To investigate this, we have studied the influence of different spacer compositions on the inverse-tapered design described. The material composition of the QWBs are kept identical to that of the spacer to ensure similar emission wavelength among the QWs. Figure 7.13 shows how the threshold current, lasing wavelength and optical confinement factor change with spacer (and QWB) composition.

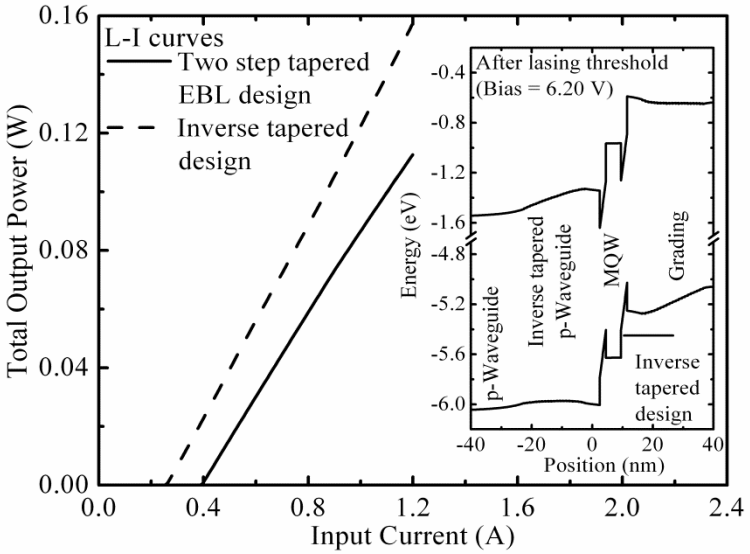

Figure 7.12: Comparison of L-I curves between two step tapered and inverse tapered designs. Inverse tapering reduces threshold current by 33% and improves slope efficiency by 14%. Inset shows the energy band diagram of the inverse tapered design above the lasing threshold, and the clear absence of potential barriers to hole injection.

Rapid degradation of threshold current indicates that electron leakage becomes dominant if the aluminum content falls below 54%. 59% Al minimizes the threshold current (and electron leakage), incurring a small red-shift to the emission wavelength. The red-shift can be easily corrected by modifying QWs' composition and/or thickness. For aluminum content in excess of 60%, threshold current starts rising sharply because of degradation of optical confinement and further separation of electron and hole wavefunctions within the QWs.

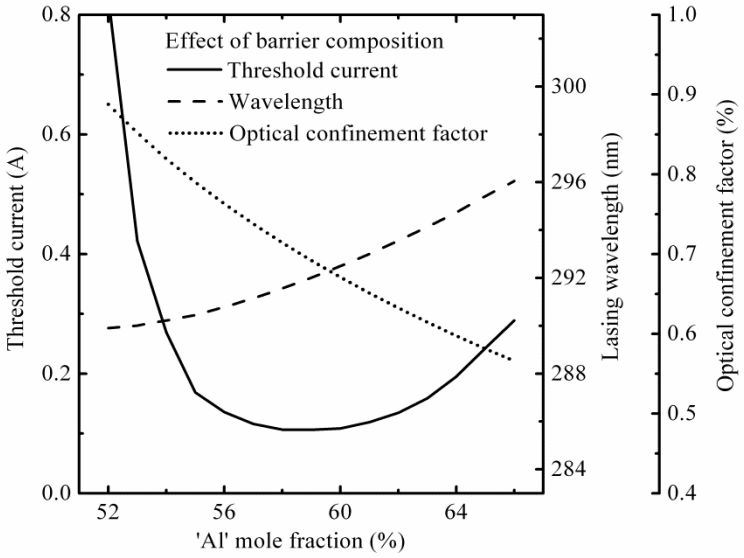

Figure 7.13: Effect of QWBs and spacer's composition on the threshold current, lasing wavelength and optical confinement factor. Narrow bandgap barriers fail to block electron leakage. On the contrary, wider bandgap QWBs (and spacer) pushes the optical mode downwards and red-shits emission wavelength via quantum-confined stark effect (QCSE).

Our inverse tapered design had a profound impact and actually generated the understanding that was necessary for our colleague Liu *et al.* in the Dupuis group. They demonstrated PN junction diode behavior under forward bias in the Al-rich material system [133].

7.4 Design Without an EBL

The inverse tapered design does not have an explicit EBL. The electron leakage is kept within tolerable limit by proper selection of MQBs and spacer's composition. It has been suggested in the literature that LED designs with no EBL may be better than those with an EBL [61]. Han *et al.* have investigated the effect of EBLs on the efficiency droop in InGaN/GaN MQW LEDs [61] and concluded that designs without an EBL offer better hole injection efficiency at high current density. To simulate such a structure, we modify the baseline design of Table 7.1 by replacing the conventionally tapered EBL with a layer of $Al_{0.48}GaN$ (p-waveguide's composition) of equal thickness (20 nm). All other quantities are unchanged for the sake of comparison. The results of simulation are shown in Figure 7.14 and 7.15. From the comparison of L-I for all four designs (see Figure 7.14), it is noted that design without an EBL is not better than the inverse tapered EBL design.

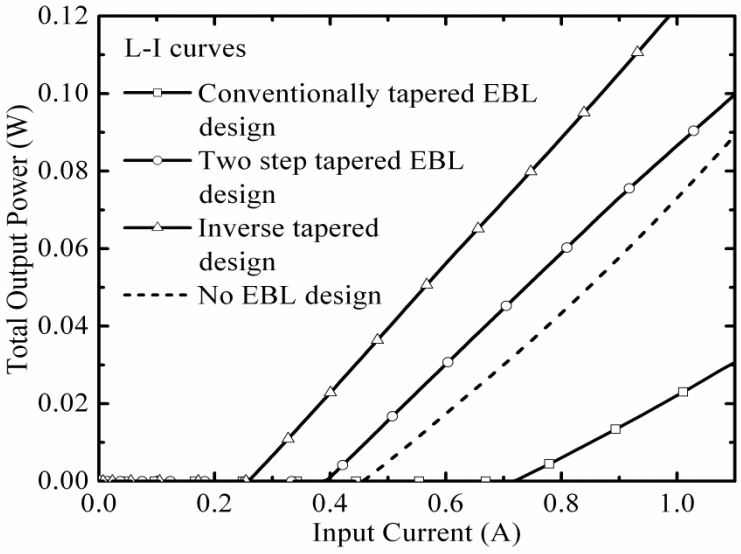

Figure 7.14: Comparison of L-I curves among all four designs. Design without an EBL beats the conventionally tapered EBL design only.

In fact, it only outperforms the conventionally tapered EBL design because the barrier height for hole injection is smaller comparatively (see Figure 7.15). Although the valence band offset is 76 meV only at the p-waveguide/spacer interface, spacer is now acting as a hole blocking layer because of the unscreened polarization charge. It is true that in the absence of an explicit EBL, the electron blocking is limited only by the conduction band offset of the spacer/QW interface and therefore, there will be leakage of electrons from the active region into the p-side. But, the degree of leakage will depend upon how much voltage is needed to lower the barrier height for efficient hole injection.

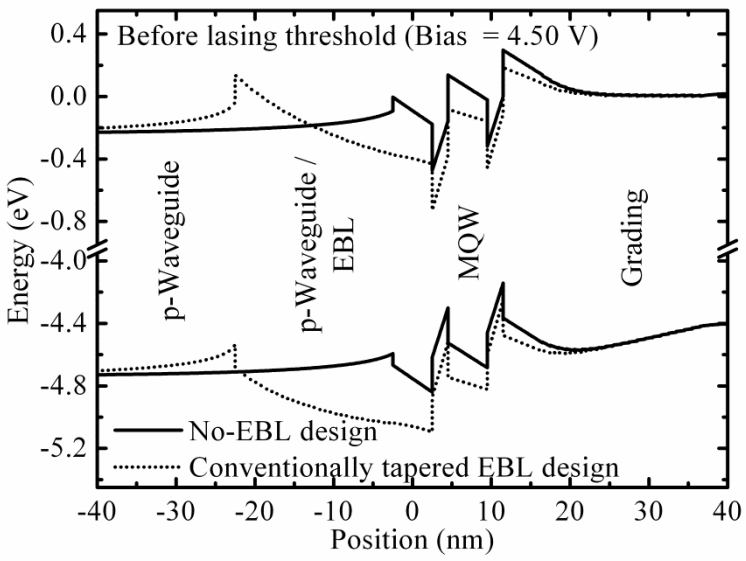

Figure 7.15: Comparison of the energy band diagrams between the design without an EBL and the conventionally tapered EBL design at a bias below the lasing threshold. The hole blocking barrier height is much smaller (0.34 eV) for the design with no EBL compared to that of the conventionally tapered EBL design (0.6 eV).

7.5 Effect of Free Carrier Absorption Loss

To estimate the optical absorption loss in III-N epitaxial layers, we have used a composition-, wavelength- and strain-dependent complex refractive index model [8, 33]. According to this model, the narrowest bandgap material ($Al_{0.45}GaN$) used for waveguide layer is found to be optically transparent at a 290 nm emission wavelength. Figure 7.16 shows the absorption spectra for GaN, AlGaN and AlN. However, Mg doped p-waveguide and Si doped n-waveguide layers may experience free carrier absorption (FCA) loss [93] and may degrade LD performance. The parameters used in the complex refractive index model are extracted from experimental data taken from undoped samples [8]. Therefore the model may not incorporate the effect of FCA loss correctly.

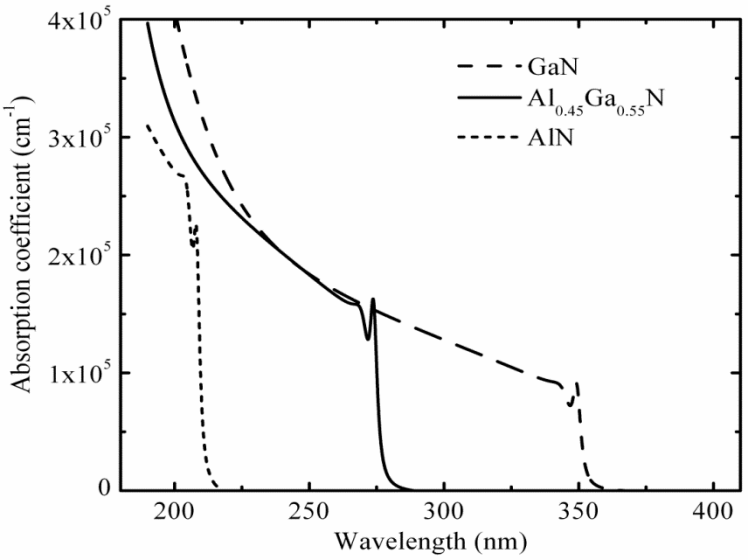

Figure 7.16: Optical absorption coefficient spectra for ternary $Al_{0.45}GaN$, binary GaN and AlN. $Al_{0.45}GaN$ is transparent for $\lambda >= 290$ nm.

At this moment, we don't have any model or experimental data to quantify the FCA loss coefficients for wide bandgap AlGaN layers. To understand qualitatively the

effect of FCA loss on LD performance, we have simulated the conventionally tapered EBL design, the two step tapered EBL design and the inverse tapered design with phenomenological distributed additional optical loss and the results are shown in Figure 7.17. By comparing the results of Figure 7.14 (simulated without additional optical loss) with that of Figure 7.17, it is noted that for all three designs, threshold current increases and slope efficiency decreases.

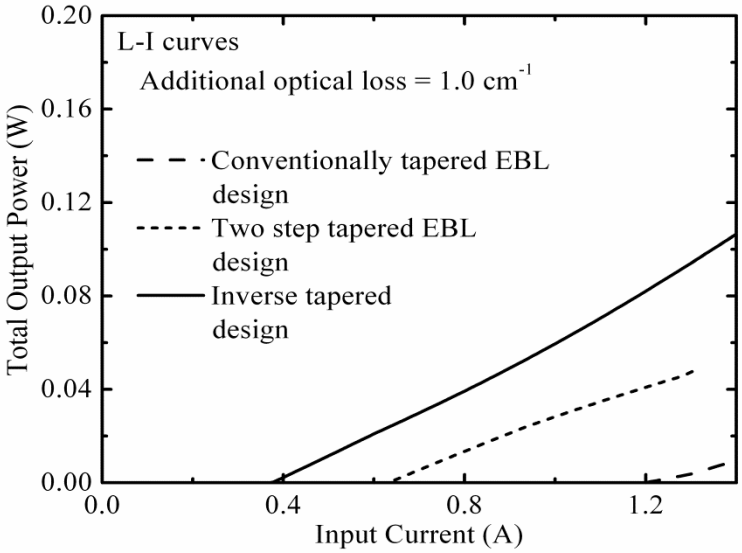

Figure 7.17: Comparison of L-I curves among all three designs in the presence of additional optical absorption loss (1.0 cm^{-1}). Inverse tapered design is the best design regardless of the additional absorption loss.

But regardless of the additional optical absorption loss, the inverse tapered design is always the best among the three designs. Figure 7.18 shows the degradation of threshold current and slope efficiency for the inverse tapered design as a function of additional optical loss. Asymmetric waveguide structures have been proposed in the literature [94, 95] to minimize the indirect phonon-assisted FCA loss in p-type layers. The epitaxial

structure of Table 7.1 features similar asymmetry in the waveguide design to push the optical mode (see Figure 7.1) away from highly absorptive p-Ohmic metal.

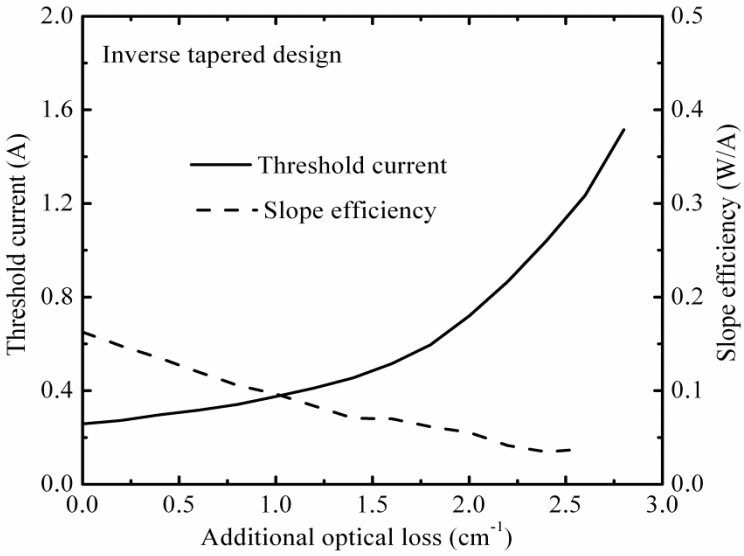

Figure 7.18: Effect of additional optical absorption loss on threshold current and slope efficiency for the inverse tapered design.

CHAPTER 8

CONCLUSION

8.1 AlInN DUV Laser Diodes on AlN Substrates Using Tapered Electron Blocking Layers

In Chapter 4, a prototypical 250 nm UV LD design based exclusively on AlInN ternary materials has been presented. AlInN-based UV LDs represent a promising alternative to AlGaN-based designs for applications in the UV-C band. Numerical simulations confirm satisfactory optical confinement in spite of low refractive index contrast. AlInN-based designs featuring homogeneous EBL layers exhibit a parasitic inversion layer of electrons as a consequence of strong interfacial polarization charge, resulting in a degradation of device performance. Instead, volumetric redistribution of polarization charge by means of a tapered EBL layer is shown to completely suppress the formation of a parasitic inversion layer without any undesirable consequences, and lead to lower threshold current. The results presented in this chapter represent the first theoretical investigation into the operation of AlInN based LD designs operating in the UV-C band.

8.2 Polarization Charge Matching in AlGaN Based DUV LDs Using Quaternary AlInGaN Barriers

A prototypical 250 nm DUV edge emitting LD design based on AlGaN ternary materials has been presented in Chapter 5. AlGaN-based UV LDs grown on AlN substrates represent a promising alternative to GaN or sapphire template based designs for applications in the UV-C band. Numerical simulations indicate that enhancement of wavefunction overlap in active regions can significantly improve threshold current and

slope efficiency. Properly chosen quaternary barrier compositions can eliminate net polarization charge at barrier/well interfaces. Overlap-enhanced LD designs can take advantage of thicker QWs to enhance both optical confinement factor and optical matrix element. Polarization matched quaternary barriers offer an additional degree of freedom to tune QW depth in the conduction and valence bands, a feature that can be used to increase carrier capture efficiency. Margin of error analysis reveals that even a partially suppressed interfacial polarization design is better than designs using ternary AlGaN barriers. Our quaternary barrier selection procedure can be easily extended to LED and LD designs operating at other wavelengths. Although the concept of polarization charge matching has already been proposed and demonstrated in the literature for LD and LED designs operating in the visible spectrum, the results presented in this chapter represent the first theoretical demonstration that the idea is also applicable for AlGaN based DUV LD designs.

8.3 Lateral Current Injection DUV LD Design Using Regrown Ohmic Contacts

A lateral current injection (LCI) design for AlGaN DUV edge emitting LDs on AlN substrates has been presented in Chapter 6. Two-dimensional optoelectronic simulation predicts lasing at a wavelength of 290 nm. Unlike vertical current injection designs, LCI designs offer the advantage of narrow bandgap p-type contact layers with minimal impact on optical confinement factor, through a partial decoupling of the problems of optical confinement and electrical injection. With polarization charge matched QWBs, a large number of QWs can be used in LCI designs which not only enhances optical confinement factor, but also distributes Joule heating over a large volume. The results presented in this chapter represent the first theoretical investigation of an LCI LD design in the III-V nitride material system.

8.4 Inverse Tapered p-Waveguide for Efficient Hole Transport

In Chapter 7, a prototypical 290 nm DUV vertical injection edge-emitting LD design based exclusively on AlGaN ternary materials has been presented. The simulation results presented here assumed realistic chemical concentration of dopant atoms with incomplete ionization. Conventionally tapered EBLs have been identified as the origin of a large electrostatic barrier to hole injection, associated with unscreened polarization charge. Several EBL designs have been investigated, and compared with conventionally-tapered EBL designs. Numerical simulations indicate that properly designed inverse tapered p-waveguide layers can significantly improve threshold current and slope efficiency through elimination of barriers to vertical hole transport, while incurring a minimum penalty to electron leakage from the active region. Optically transparent but narrow bandgap material has been utilized for n-waveguide layers to reduce the optical absorption in lossy p-Ohmic metal by pulling the optical mode downward. The proposed inverse tapered structure can be extended to LD designs operating at shorter wavelengths.

8.5 Future Research Directions

To extend the inverse tapered design of Chapter 7 to shorter emission wavelengths, it is necessary to design the p-type layers judiciously. At present, it will be extremely challenging to achieve p-type conductivity in AlGaN layers that are transparent at the 250 nm emission wavelength [133, 160]. The idea of photonic crystals [161] may be employed to lower the refractive index of the narrow bandgap p-waveguide layers by averaging it with air or low refractive index oxides, incurring a penalty to the series resistance. If we increase the thickness of the n-waveguide layer to reduce the corresponding lateral series resistance, there is a chance that the optical mode, which is not centered on the active region, may become a slab mode. This will reduce the optical confinement factor and may introduce additional optical absorption loss in the n-Ohmic

metal. A double etched ridge-shaped structure may be used to provide lateral confinement for the optical mode.

One of the critical problems for the III-N based LDs and LEDs is the existence of net interface polarization charge at the heterointerfaces for polar *c*-axis growth [113]. Significant research is going on to improve the quality of epitaxial layers grown along the non-polar and semi-polar axes [162], because at present their growth quality is not comparable to that of the *c*-axis growth [40]. To design LD structures to be grown along the non-polar or semi-polar axis, it is necessary to use the correct material parameters for the purpose of numerical simulation, especially the ones that are used for the bandstructure and polarization charge calculations. The charge transport model used in this dissertation accounts phenomenologically for ballistic transport in the active region by Bethe's thermionic emission theory, under the assumption that the heterojunctions are abrupt. The validity of this approximation deserves additional scrutiny for applications involving steep gradients in potential energy. It has been reported that hexagonal boron nitride (hBN) may be a very promising candidate for the p-type layers of UV light emitters [163]. The material system of hBN is compatible with wurtzite AlGaN and AlN, it may offer better electron blocking and hole injection via type-II band alignment with AlN. Besides these, the activation energy of p-type dopant atoms is significantly smaller than that in AlN. All these findings inspire confidence to pursue hBN based vertical injection edge-emitting DUV LD designs in the future.

One major disadvantage of the LCI LD design presented in Chapter 6 is that the current must flow through a small lateral cross-section of the active region. On the contrary, vertical injection designs allow the current to flow through the larger cross-sectional area of the mesa. Although the proposed LCI LD design employs a large number of QWs to distribute the Joule heating over a larger volume, it may be necessary to estimate the local distribution of temperature throughout the epitaxial structure by solving the two dimensional steady state heat flux equation. The outcome of such

rigorous calculations may predict whether the proposed design can be operated in continuous wave (CW) mode instead of pulsed mode.

REFERENCES

[1] J. Cabalo, M. DeLucia, A. Goad, J. Lacis, F. Narayanan, and D. Sickenberger, "Overview of the TAC-BIO detector," pp. 71160D-71160D-11, 2008.

[2] G. Knight, "Water and air treatment using ultraviolet light sources," presented at the Conference on Lasers and Electro-Optics (CLEO), Baltimore, MD 2011.

[3] P. H. Hart, S. Gorman, and J. J. Finlay-Jones, "Modulation of the immune system by UV radiation: more than just the effects of vitamin D?," *Nature reviews. Immunology,* vol. 11, pp. 584-96, Sep 2011.

[4] S. Abe, S. Sato, E. Ito, M. Tsukuda, M. Tomiyama, and E. Ohno, "Master Recording for High-Density Disk Using 248 nm Laser Beam Recorder," *Japanese Journal of Applied Physics,* vol. 41, pp. 1704-1708, 2002.

[5] H. Ding, G. Chen, A. K. Majumdar, B. M. Sadler, and Z. Xu, "Turbulence modeling for non-line-of-sight ultraviolet scattering channels," pp. 80380J-80380J-8, 2011.

[6] W. C. Xu, Y. Yang, and J. Y. Sun, "Study on Preparation and Properties of Fluorescent Offset Printing Ink," *Advanced Materials Research,* vol. 174, pp. 393-396, 2010.

[7] Z. W. Jun Du, Wei He, Yiping Tang, "Numerical analysis of impact of imprinting pressure on profile shape and mold deformation in UV-NIL " presented at the IEEE International Conference on Nano/Micro Engineered and Molecular Systems (NEMS), 2011.

[8] J. Piprek, *Nitride semiconductor devices : principles and simulation*. Weinheim: Wiley-VCH ; [Chichester : John Wiley [distributor]], 2007.

[9] T. Nishida, T. Makimoto, H. Saito, and T. Ban, "AlGaN-based ultraviolet light-emitting diodes grown on bulk AlN substrates," *Applied Physics Letters,* vol. 84, p. 1002, 2004.

[10] J. Edmond, A. Abare, M. Bergman, J. Bharathan, K. Lee Bunker, D. Emerson, K. Haberern, J. Ibbetson, M. Leung, P. Russel, and D. Slater, "High efficiency GaN-based LEDs and lasers on SiC," *Journal of Crystal Growth,* vol. 272, pp. 242-250, 2004.

[11] T. Kolbe, T. Sembdner, A. Knauer, V. Kueller, H. Rodriguez, S. Einfeldt, P. Vogt, M. Weyers, and M. Kneissl, "(In)AlGaN deep ultraviolet light emitting diodes with optimized quantum well width," *physica status solidi (a),* vol. 207, pp. 2198-2200, 2010.

[12] M. Kim, T. Fujita, S. Fukahori, T. Inazu, C. Pernot, Y. Nagasawa, A. Hirano, M. Ippommatsu, M. Iwaya, T. Takeuchi, S. Kamiyama, M. Yamaguchi, Y. Honda, H. Amano, and I. Akasaki, "AlGaN-Based Deep Ultraviolet Light-Emitting Diodes Fabricated on Patterned Sapphire Substrates," *Applied Physics Express,* vol. 4, p. 092102, 2011.

[13] M. Asif Khan, "AlGaN multiple quantum well based deep UV LEDs and their applications," *physica status solidi (a),* vol. 203, pp. 1764-1770, 2006.

[14] T. Mino, H. Hirayama, T. Takano, K. Tsubaki, and M. Sugiyama, "Characteristics of epitaxial lateral overgrowth AlN templates on (111)Si substrates for AlGaN deep-UV LEDs fabricated on different direction stripe patterns," *physica status solidi (c),* vol. 9, pp. 802-805, 2012.

[15] A. Fujioka, T. Misaki, T. Murayama, Y. Narukawa, and T. Mukai, "Improvement in Output Power of 280-nm Deep Ultraviolet Light-Emitting Diode by Using AlGaN Multi Quantum Wells," *Applied Physics Express,* vol. 3, p. 041001, 2010.

[16] Z. Ren, Q. Sun, S. Y. Kwon, J. Han, K. Davitt, Y. K. Song, A. V. Nurmikko, H. K. Cho, W. Liu, J. A. Smart, and L. J. Schowalter, "Heteroepitaxy of AlGaN on bulk AlN substrates for deep ultraviolet light emitting diodes," *Applied Physics Letters,* vol. 91, p. 051116, 2007.

[17] M. Khizar, Z. Y. Fan, K. H. Kim, J. Y. Lin, and H. X. Jiang, "Nitride deep-ultraviolet light-emitting diodes with microlens array," *Applied Physics Letters,* vol. 86, p. 173504, 2005.

[18] M. Shatalov, A. Lunev, X. Hu, O. Bilenko, I. Gaska, W. Sun, J. Yang, A. Dobrinsky, Y. Bilenko, R. Gaska, and M. Shur, "Performance and Applications of Deep Uv Led," *International Journal of High Speed Electronics and Systems,* vol. 21, p. 1250011, 2012.

[19] C. Chua, Z. H. Yang, C. Knollenberg, M. Teepe, and N. Johnson, "Sub-300 nm UV LEDs with Defect Reduction Layer and Vertical-injection Architecture," *2011 Conference on Lasers and Electro-Optics (Cleo),* 2011.

[20] Y. T. Liao, C. K. Kao, C. Thomidis, A. Moldawer, J. Woodward, D. Bhattarai, and T. D. Moustakas, "Recent progress of efficient deep UV-LEDs by plasma-assisted molecular beam epitaxy," *Physica Status Solidi C: Current Topics in Solid State Physics, Vol 9, No 3-4,* vol. 9, pp. 798-801, 2012.

[21] Y. Taniyasu, M. Kasu, and T. Makimoto, "An aluminium nitride light-emitting diode with a wavelength of 210 nanometres," *Nature,* vol. 441, pp. 325-328, 2006.

[22] T. Takano, Y. Narita, A. Horiuchi, and H. Kawanishi, "Room-temperature deep-ultraviolet lasing at 241.5 nm of AlGaN multiple-quantum-well laser," *Applied Physics Letters,* vol. 84, p. 3567, 2004.

[23] M. Shatalov, M. Gaevski, V. Adivarahan, and A. Khan, "Room-temperature stimulated emission from AlN at 214 nm," *Japanese Journal of Applied Physics Part 2-Letters & Express Letters,* vol. 45, pp. L1286-L1288, Dec 2006.

[24] T. Wunderer, C. L. Chua, J. E. Northrup, Z. Yang, N. M. Johnson, M. Kneissl, G. A. Garrett, H. Shen, M. Wraback, B. Moody, H. S. Craft, R. Schlesser, R. F. Dalmau, and Z. Sitar, "Optically pumped UV lasers grown on bulk AlN substrates," *physica status solidi (c),* vol. 9, pp. 822-825, 2012.

[25] S. Nagahama, T. Yanamoto, M. Sano, and T. Mukai, "Study of GaN-based laser diodes in near ultraviolet region," *Japanese Journal of Applied Physics Part 1-Regular Papers Short Notes & Review Papers,* vol. 41, pp. 5-10, Jan 2002.

[26] M. Kneissl, D. W. Treat, M. Teepe, N. Miyashita, and N. M. Johnson, "Ultraviolet AlGaN multiple-quantum-well laser diodes," *Applied Physics Letters,* vol. 82, p. 4441, 2003.

[27] K. Iida, T. Kawashima, A. Miyazaki, H. Kasugai, S. Mishima, A. Honshio, Y. Miyake, M. Iwaya, S. Kamiyama, H. Amano, and I. Akasaki, "350.9 nm UV Laser Diode Grown on Low-Dislocation-Density AlGaN," *Japanese Journal of Applied Physics,* vol. 43, pp. L499-L500, 2004.

[28] S. Masui, Y. Matsuyama, T. Yanamoto, T. Kozaki, S.-i. Nagahama, and T. Mukai, "365 nm Ultraviolet Laser Diodes Composed of Quaternary AlInGaN Alloy," *Japanese Journal of Applied Physics,* vol. 42, pp. L1318-L1320, 2003.

[29] H. Yoshida, Y. Yamashita, M. Kuwabara, and H. Kan, "Demonstration of an ultraviolet 336 nm AlGaN multiple-quantum-well laser diode," *Applied Physics Letters,* vol. 93, p. 241106, 2008.

[30] J. H. Ryou, P. D. Yoder, J. P. Liu, Z. Lochner, H. Kim, S. Choi, H. J. Kim, and R. D. Dupuis, "Control of Quantum-Confined Stark Effect in InGaN-Based Quantum Wells," *Ieee Journal of Selected Topics in Quantum Electronics,* vol. 15, pp. 1080-1091, Jul-Aug 2009.

[31] J. Simon, V. Protasenko, C. Lian, H. Xing, and D. Jena, "Polarization-Induced Hole Doping in Wide-Band-Gap Uniaxial Semiconductor Heterostructures," *Science,* vol. 327, pp. 60-64, 2009.

[32] J. P. Zhang, A. Chitnis, V. Adivarahan, S. Wu, V. Mandavilli, R. Pachipulusu, M. Shatalov, G. Simin, J. W. Yang, and M. A. Khan, "Milliwatt power deep

ultraviolet light-emitting diodes over sapphire with emission at 278 nm," *Applied Physics Letters,* vol. 81, p. 4910, 2002.

[33] J. Piprek, *Semiconductor optoelectronic devices : introduction to physics and simulation*. Amsterdam ; Boston: Academic Press, 2003.

[34] H. Tsuzuki, F. Mori, K. Takeda, M. Iwaya, S. Kamiyama, H. Amano, I. Akasaki, H. Yoshida, M. Kuwabara, and Y. Yamashita, "Novel UV devices on high-quality AlGaN using grooved underlying layer," *Journal of Crystal Growth,* vol. 311, pp. 2860-2863, 2009.

[35] N. Crystals, "AIN: can it become a universal substrate for Ill-nitrides?," *Compound Semiconductor,* vol. 16, pp. 17-19, 2010.

[36] Y. Zhang, S. Gautier, C.-Y. Cho, E. Cicek, Z. Vashaei, R. McClintock, C. Bayram, Y. Bai, and M. Razeghi, "Near milliwatt power AlGaN-based ultraviolet light emitting diodes based on lateral epitaxial overgrowth of AlN on Si(111)," *Applied Physics Letters,* vol. 102, p. 011106, 2013.

[37] H. Okumura, T. Kimoto, and J. Suda, "Over-700-nm Critical Thickness of AlN Grown on 6H-SiC(0001) by Molecular Beam Epitaxy," *Applied Physics Express,* vol. 5, p. 105502, 2012.

[38] R. Kirste, M. R. Wagner, C. Nenstiel, F. Brunner, M. Weyers, and A. Hoffmann, "Effect of TMGa preflow on the properties of high temperature AlN layers grown on sapphire," *physica status solidi (a),* vol. 210, pp. 285-290, 2013.

[39] G. Franssen, T. Suski, P. Perlin, R. Bohdan, A. Bercha, W. Trzeciakowski, I. Makarowa, R. Czernecki, M. Leszczyński, and I. Grzegory, "Screening of polarization induced electric fields in blue/violet InGaN/GaN laser diodes by Si doping in quantum barriers revealed by hydrostatic pressure," *physica status solidi (c),* vol. 3, pp. 2303-2306, 2006.

[40] Y.-K. Kuo, M.-C. Tsai, and S.-H. Yen, "Numerical simulation of blue InGaN light-emitting diodes with polarization-matched AlGaInN electron-blocking layer and barrier layer," *Optics Communications,* vol. 282, pp. 4252-4255, 2009.

[41] H.-H. Huang and Y.-R. Wu, "Study of polarization properties of light emitted from a-plane InGaN/GaN quantum well-based light emitting diodes," *Journal of Applied Physics,* vol. 106, p. 023106, 2009.

[42] A. A. Yamaguchi, "Theoretical investigation on polarization control of semipolar-oriented InGaN quantum-well emission using (Al)InGaN alloy substrates," *Applied Physics Letters,* vol. 94, p. 201104, 2009.

[43] P.-Y. Dang and Y.-R. Wu, "Optical polarization anisotropy of tensile strained InGaN/AlInN quantum wells for TM mode lasers," *Journal of Applied Physics,* vol. 108, p. 083108, 2010.

[44] H. P. Zhao, G. Y. Liu, J. Zhang, J. D. Poplawsky, V. Dierolf, and N. Tansu, "Approaches for high internal quantum efficiency green InGaN light-emitting diodes with large overlap quantum wells," *Optics Express,* vol. 19, pp. A991-A1007, Jul 4 2011.

[45] J. Park and Y. Kawakami, "Photoluminescence property of InGaN single quantum well with embedded AlGaN δ layer," *Applied Physics Letters,* vol. 88, p. 202107, 2006.

[46] H. Zhao, G. Liu, and N. Tansu, "Analysis of InGaN-delta-InN quantum wells for light-emitting diodes," *Applied Physics Letters,* vol. 97, p. 131114, 2010.

[47] H. Zhao, G. Liu, X.-H. Li, G. S. Huang, J. D. Poplawsky, S. T. Penn, V. Dierolf, and N. Tansu, "Growths of staggered InGaN quantum wells light-emitting diodes emitting at 520–525 nm employing graded growth-temperature profile," *Applied Physics Letters,* vol. 95, p. 061104, 2009.

[48] Z. Yang, R. Li, Q. Wei, T. Yu, Y. Zhang, W. Chen, and X. Hu, "Analysis of optical gain property in the InGaN/GaN triangular shaped quantum well under the piezoelectric field," *Applied Physics Letters,* vol. 94, p. 061120, 2009.

[49] W. Lee, M.-H. Kim, D. Zhu, A. N. Noemaun, J. K. Kim, and E. F. Schubert, "Growth and characteristics of GaInN/GaInN multiple quantum well light-emitting diodes," *Journal of Applied Physics,* vol. 107, p. 063102, 2010.

[50] J. Xu, M. F. Schubert, A. N. Noemaun, D. Zhu, J. K. Kim, E. F. Schubert, M. H. Kim, H. J. Chung, S. Yoon, C. Sone, and Y. Park, "Reduction in efficiency droop, forward voltage, ideality factor, and wavelength shift in polarization-matched GaInN/GaInN multi-quantum-well light-emitting diodes," *Applied Physics Letters,* vol. 94, p. 011113, 2009.

[51] B. Witzigmann, A. Witzig, and W. Fichtner, "A multidimensional laser simulator for edge-emitters including quantum carrier capture," *Ieee Transactions on Electron Devices,* vol. 47, pp. 1926-1934, Oct 2000.

[52] A. Venkatachalam, B. Klein, J. H. Ryou, S. C. Shen, R. D. Dupuis, and P. D. Yoder, "Design Strategies for InGaN-Based Green Lasers," *Ieee Journal of Quantum Electronics,* vol. 46, pp. 238-245, Feb 2010.

[53] P. J. Parbrook and T. Wang, "Light Emitting and Laser Diodes in the Ultraviolet," *Ieee Journal of Selected Topics in Quantum Electronics,* vol. 17, pp. 1402-1411, Sep-Oct 2011.

[54] H. Ghafouri-Shiraz, *The principles of semiconductor laser diodes and amplifiers : analysis and transmission line laser modelling*. London: Imperial College Press, 2004.

[55] A. Knauer, H. Wenzel, T. Kolbe, S. Einfeldt, M. Weyers, M. Kneissl, and G. Tränkle, "Effect of the barrier composition on the polarization fields in near UV InGaN light emitting diodes," *Applied Physics Letters,* vol. 92, p. 191912, 2008.

[56] M. F. Schubert, J. Xu, J. K. Kim, E. F. Schubert, M. H. Kim, S. Yoon, S. M. Lee, C. Sone, T. Sakong, and Y. Park, "Polarization-matched GaInN/AlGaInN multi-quantum-well light-emitting diodes with reduced efficiency droop," *Applied Physics Letters,* vol. 93, p. 041102, 2008.

[57] M.-H. Kim, M. F. Schubert, Q. Dai, J. K. Kim, E. F. Schubert, J. Piprek, and Y. Park, "Origin of efficiency droop in GaN-based light-emitting diodes," *Applied Physics Letters,* vol. 91, p. 183507, 2007.

[58] H. J. Chung, R. J. Choi, M. H. Kim, J. W. Han, Y. M. Park, Y. S. Kim, H. S. Paek, C. S. Sone, Y. J. Park, J. K. Kim, and E. F. Schubert, "Improved performance of GaN-based blue light emitting diodes with InGaN/GaN multilayer barriers," *Applied Physics Letters,* vol. 95, p. 241109, 2009.

[59] E. Sakalauskas, B. Reuters, L. R. Khoshroo, H. Kalisch, M. Heuken, A. Vescan, M. Röppischer, C. Cobet, G. Gobsch, and R. Goldhahn, "Dielectric function and optical properties of quaternary AlInGaN alloys," *Journal of Applied Physics,* vol. 110, p. 013102, 2011.

[60] K. Hess, *Advanced theory of semiconductor devices*. New York: IEEE Press, 1999.

[61] S.-H. Han, D.-Y. Lee, S.-J. Lee, C.-Y. Cho, M.-K. Kwon, S. P. Lee, D. Y. Noh, D.-J. Kim, Y. C. Kim, and S.-J. Park, "Effect of electron blocking layer on efficiency droop in InGaN/GaN multiple quantum well light-emitting diodes," *Applied Physics Letters,* vol. 94, p. 231123, 2009.

[62] J. Liu, Y. Zhang, Z. Lochner, S.-S. Kim, H. Kim, J.-H. Ryou, S.-C. Shen, P. Doug Yoder, R. D. Dupuis, and Q. Y. Wei, "Performance characteristics of InAlGaN laser diodes depending on electron blocking layer and waveguiding layer design grown by metalorganic chemical vapordeposition," *Journal of Crystal Growth,* vol. 315, pp. 272-277, 2011.

[63] Y. Zhang, T.-T. Kao, J. Liu, Z. Lochner, S.-S. Kim, J.-H. Ryou, R. D. Dupuis, and S.-C. Shen, "Effects of a step-graded AlxGa1−xN electron blocking layer in InGaN-based laser diodes," *Journal of Applied Physics,* vol. 109, p. 083115, 2011.

[64] C. H. Wang, C. C. Ke, C. Y. Lee, S. P. Chang, W. T. Chang, J. C. Li, Z. Y. Li, H. C. Yang, H. C. Kuo, T. C. Lu, and S. C. Wang, "Hole injection and efficiency droop improvement in InGaN/GaN light-emitting diodes by band-engineered electron blocking layer," *Applied Physics Letters,* vol. 97, p. 261103, 2010.

[65] Y.-Y. Zhang and G.-R. Yao, "Performance enhancement of blue light-emitting diodes with AlGaN barriers and a special designed electron-blocking layer," *Journal of Applied Physics,* vol. 110, p. 093104, 2011.

[66] W. Yang, D. Li, N. Liu, Z. Chen, L. Wang, L. Liu, L. Li, C. Wan, W. Chen, X. Hu, and W. Du, "Improvement of hole injection and electron overflow by a tapered AlGaN electron blocking layer in InGaN-based blue laser diodes," *Applied Physics Letters,* vol. 100, p. 031105, 2012.

[67] S.-J. Lee, C.-Y. Cho, S.-H. Hong, S.-H. Han, S. Yoon, S.-T. Kim, and S.-J. Park, "Enhanced Optical Power of InGaN/GaN Light-Emitting Diode by AlGaN Interlayer and Electron Blocking Layer," *IEEE Photonics Technology Letters,* vol. 24, pp. 1991-1994, 2012.

[68] Y. K. Kuo, J. Y. Chang, and M. C. Tsai, "Enhancement in hole-injection efficiency of blue InGaN light-emitting diodes from reduced polarization by some specific designs for the electron blocking layer," *Optics Letters,* vol. 35, pp. 3285-3287, Oct 1 2010.

[69] S. Choi, H. J. Kim, S.-S. Kim, J. Liu, J. Kim, J.-H. Ryou, R. D. Dupuis, A. M. Fischer, and F. A. Ponce, "Improvement of peak quantum efficiency and efficiency droop in III-nitride visible light-emitting diodes with an InAlN electron-blocking layer," *Applied Physics Letters,* vol. 96, p. 221105, 2010.

[70] Y.-K. Kuo, Y.-H. Chen, J.-Y. Chang, and M.-C. Tsai, "Numerical analysis on the effects of bandgap energy and polarization of electron blocking layer in near-ultraviolet light-emitting diodes," *Applied Physics Letters,* vol. 100, p. 043513, 2012.

[71] Y. Yan Zhang and Y. An Yin, "Performance enhancement of blue light-emitting diodes with a special designed AlGaN/GaN superlattice electron-blocking layer," *Applied Physics Letters,* vol. 99, p. 221103, 2011.

[72] Y.-Y. Zhang, X.-L. Zhu, Y.-A. Yin, and J. Ma, "Performance Enhancement of Near-UV Light-Emitting Diodes With an InAlN/GaN Superlattice Electron-Blocking Layer," *Ieee Electron Device Letters,* vol. 33, pp. 994-996, 2012.

[73] A. Y. Polyakov, N. B. Smirnov, A. V. Govorkov, E. A. Kozhukhova, A. M. Dabiran, P. P. Chow, A. M. Wowchak, I.-H. Lee, J.-W. Ju, and S. J. Pearton, "Comparison of electrical properties and deep traps in p-Al[sub x]Ga[sub 1−x]N

grown by molecular beam epitaxy and metal organic chemical vapor deposition," *Journal of Applied Physics,* vol. 106, p. 073706, 2009.

[74] M. L. Nakarmi, N. Nepal, J. Y. Lin, and H. X. Jiang, "Photoluminescence studies of impurity transitions in Mg-doped AlGaN alloys," *Applied Physics Letters,* vol. 94, p. 091903, 2009.

[75] M. Imura, N. Kato, N. Okada, K. Balakrishnan, M. Iwaya, S. Kamiyama, H. Amano, I. Akasaki, T. Noro, T. Takagi, and A. Bandoh, "Mg-doped high-quality AlxGa1–xN (x=0-1) grown by high-temperature metal-organic vapor phase epitaxy," *physica status solidi (c),* vol. 4, pp. 2502-2505, 2007.

[76] R. F. Pierret, *Advanced semiconductor fundamentals*, 2nd ed. ed. Upper Saddle River, N.J.: Prentice Hall ; London : Pearson Education, 2003.

[77] P. Kozodoy, H. Xing, S. P. DenBaars, U. K. Mishra, A. Saxler, R. Perrin, S. Elhamri, and W. C. Mitchel, "Heavy doping effects in Mg-doped GaN," *Journal of Applied Physics,* vol. 87, p. 1832, 2000.

[78] C. Bayram, J. L. Pau, R. McClintock, and M. Razeghi, "Delta-doping optimization for high quality p-type GaN," *Journal of Applied Physics,* vol. 104, p. 083512, 2008.

[79] Y. Kamii, I. Waki, H. Fujioka, M. Oshima, H. Miki, and M. Okuyama, "Electrical characteristics of Mg-doped GaN activated with Ni catalysts," *Applied Surface Science,* vol. 190, pp. 348-351, May 8 2002.

[80] R. Y. Korotkov, J. M. Gregie, and B. W. Wessels, "Electrical properties of p-type GaN:Mg codoped with oxygen," *Applied Physics Letters,* vol. 78, p. 222, 2001.

[81] M. L. Nakarmi, K. H. Kim, J. Li, J. Y. Lin, and H. X. Jiang, "Enhanced p-type conduction in GaN and AlGaN by Mg-δ-doping," *Applied Physics Letters,* vol. 82, p. 3041, 2003.

[82] E. Trybus, W. A. Doolittle, M. Moseley, W. Henderson, D. Billingsley, G. Namkoong, and D. C. Look, "Extremely high hole concentrations in *c*-plane GaN," *physica status solidi (c),* vol. 6, pp. S788-S791, 2009.

[83] W. A. Doolittle, M. Moseley, and E. Trybus, "Deeply Degenerate p-type GaN Grown by Metal Modulated Epitaxy," presented at the 2009 International Semiconductor Device Research Symposium (ISDRS 2009), College Park, MD, USA, 2009.

[84] J. Piprek, "Ultra-violet light-emitting diodes with quasi acceptor-free AlGaN polarization doping," *Optical and Quantum Electronics,* vol. 44, pp. 67-73, 2011.

[85] J. Verma, J. Simon, V. Protasenko, T. Kosel, H. Grace Xing, and D. Jena, "N-polar III-nitride quantum well light-emitting diodes with polarization-induced doping," *Applied Physics Letters,* vol. 99, p. 171104, 2011.

[86] L. Zhang, K. Ding, N. X. Liu, T. B. Wei, X. L. Ji, P. Ma, J. C. Yan, J. X. Wang, Y. P. Zeng, and J. M. Li, "Theoretical study of polarization-doped GaN-based light-emitting diodes," *Applied Physics Letters,* vol. 98, p. 101110, 2011.

[87] L. Zhang, K. Ding, J. C. Yan, J. X. Wang, Y. P. Zeng, T. B. Wei, Y. Y. Li, B. J. Sun, R. F. Duan, and J. M. Li, "Three-dimensional hole gas induced by polarization in (0001)-oriented metal-face III-nitride structure," *Applied Physics Letters,* vol. 97, p. 062103, 2010.

[88] K. Dong, D. Chen, B. Liu, H. Lu, P. Chen, R. Zhang, and Y. Zheng, "Characteristics of polarization-doped N-face III-nitride light-emitting diodes," *Applied Physics Letters,* vol. 100, p. 073507, 2012.

[89] S. Li, M. E. Ware, V. P. Kunets, M. Hawkridge, P. Minor, J. Wu, and G. J. Salamo, "Polarization induced doping in graded AlGaN films," *physica status solidi (c),* vol. 8, pp. 2182-2184, 2011.

[90] M. Polyanskiy. (06/15/2014). *Refractive Index Database*. Available: http://refractiveindex.info

[91] D. Bour, C. Chua, Z. Yang, M. Teepe, and N. Johnson, "Silver-clad nitride semiconductor laser diode," *Applied Physics Letters,* vol. 94, p. 041124, 2009.

[92] B. Cheng, C. L. Chua, Y. Zhihong, M. Teepe, C. Knollenberg, A. Strittmatter, and N. Johnson, "Nitride Laser Diodes With Nonepitaxial Cladding Layers," *Ieee Photonics Technology Letters,* vol. 22, pp. 329-331, 2010.

[93] E. Kioupakis, P. Rinke, and C. G. V. d. Walle, "Determination of Internal Loss in Nitride Lasers from First Principles," *Applied Physics Express,* vol. 3, p. 082101, July 16, 2010 2010.

[94] C.-Y. Huang, Y.-D. Lin, A. Tyagi, A. Chakraborty, H. Ohta, J. S. Speck, S. P. DenBaars, and S. Nakamura, "Optical waveguide simulations for the optimization of InGaN-based green laser diodes," *JOURNAL OF APPLIED PHYSICS,* vol. 107, p. 023101, 22 January 2010 2010.

[95] M. Kuramoto, C. Sasaoka, N. Futagawa, M. Nido, and A. A. Yamaguchi, "Reduction of Internal Loss and Threshold Current in a Laser Diode with a Ridge by Selective Re-Growth (RiS-LD)," *Physica status solidi (a),* vol. 192, p. 329, April 20, 2002 2002.

[96] K. B. Nam, J. Li, M. L. Nakarmi, J. Y. Lin, and H. X. Jiang, "Unique optical properties of AlGaN alloys and related ultraviolet emitters," *Applied Physics Letters,* vol. 84, p. 5264, 2004.

[97] H. Yoshida, M. Kuwabara, Y. Yamashita, Y. Takagi, K. Uchiyama, and H. Kan, "AlGaN-based laser diodes for the short-wavelength ultraviolet region," *New Journal of Physics,* vol. 11, p. 125013, 2009.

[98] R. Banal, M. Funato, and Y. Kawakami, "Optical anisotropy in [0001]-oriented AlxGa1−xN/AlN quantum wells (x > 0.69)," *Physical Review B,* vol. 79, 2009.

[99] C. Kim, I. K. Robinson, J. Myoung, K. Shim, M. C. Yoo, and K. Kim, "Critical thickness of GaN thin films on sapphire(0001)," *Applied Physics Letters,* vol. 69, pp. 2358-2360, Oct 14 1996.

[100] J. W. Matthews and A. E. Blakeslee, "Defects in epitaxial multilayers," *Journal of Crystal Growth,* vol. 27, pp. 118-125, 1974.

[101] A. Fischer, H. Kuhne, and H. Richter, "New Approach in Equilibrium-Theory for Strained-Layer Relaxation," *Physical Review Letters,* vol. 73, pp. 2712-2715, Nov 14 1994.

[102] R. People and J. C. Bean, "Calculation of critical layer thickness versus lattice mismatch for GexSi1−x/Si strained-layer heterostructures," *Applied Physics Letters,* vol. 47, p. 322, 1985.

[103] D. Holec, "Multi-scale modelling of III-nitrides: from dislocations to the electronic structure," Ph.D., Department of Materials Science and Metallurgy, University of Cambridge, 2008.

[104] D. Holec, P. M. F. J. Costa, M. J. Kappers, and C. J. Humphreys, "Critical thickness calculations for InGaN/GaN," *Journal of Crystal Growth,* vol. 303, pp. 314-317, May 1 2007.

[105] B. Monemar, "III-V nitrides - important future electronic materials," *Journal of Materials Science-Materials in Electronics,* vol. 10, pp. 227-254, Jun 1999.

[106] D. Gogova, A. Kasic, H. Larsson, B. Pécz, R. Yakimova, B. Magnusson, B. Monemar, F. Tuomisto, K. Saarinen, C. Miskys, M. Stutzmann, C. Bundesmann, and M. Schubert, "Optical and Structural Characteristics of Virtually Unstrained Bulk-Like GaN," *Japanese Journal of Applied Physics,* vol. 43, pp. 1264-1268, 2004.

[107] D. Gogova, A. Kasic, H. Larsson, C. Hemmingsson, B. Monemar, F. Tuomisto, K. Saarinen, L. Dobos, B. Pécz, P. Gibart, and B. Beaumont, "Strain-free bulk-

like GaN grown by hydride-vapor-phase-epitaxy on two-step epitaxial lateral overgrown GaN template," *Journal of Applied Physics,* vol. 96, p. 799, 2004.

[108] Z. Q. Li, Z. M. S. Li, and J. Piprek, "Simulations of laser diodes with nonpolar InGaN multi-quantum-wells," *physica status solidi (c),* vol. 7, pp. 2259-2261, 2010.

[109] J. R. Chen, T. S. Ko, P. Y. Su, T. C. Lu, H. C. Kuo, Y. K. Kuo, and S. C. Wang, "Numerical Study on Optimization of Active Layer Structures for GaN/AlGaN Multiple-Quantum-Well Laser Diodes," *Journal of Lightwave Technology,* vol. 26, pp. 3155-3165, Sep-Oct 2008.

[110] R. A. Abdullah and K. Ibrahim, "InGaN MQW violet laser diode performance with quaternary AlInGaN blocking layer," *Optics Communications,* vol. 282, pp. 4755-4758, 2009.

[111] K. A. Bulashevich, M. S. Ramm, and S. Y. Karpov, "Effects of electron and optical confinement on performance of UV laser diodes," *physica status solidi (c),* vol. 6, pp. 603-606, 2009.

[112] X. Jin, B. Zhang, S. Jobe, J. DeLeon, J. Flickinger, T. Dai, G. Zhang, E. Heller, and L. Chen, "Two-dimension simulation of gallium nitride-based laser diode," *Nusod '07: Proceedings of the 7th International Conference on Numerical Simulation of Optoelectronic Devices,* pp. 37-38, 2007.

[113] A. Venkatachalam, P. D. Yoder, B. Klein, and A. Kulkarni, "Nitride band-structure model in a quantum well laser simulator," *Optical and Quantum Electronics,* vol. 40, pp. 295-299, Apr-May 2008.

[114] P. Karbownik and R. P. Sarzała, "Structure optimisation of short-wavelength ridge-waveguide InGaN/GaN diode lasers," *Opto-Electronics Review,* vol. 16, pp. 27-33, 2008.

[115] B. Witzigmann, M. Tomamichel, S. Steiger, R. G. Veprek, K. Kojima, and U. T. Schwarz, "Analysis of gain and luminescence in violet and blue GaInN-GaN quantum wells," *Ieee Journal of Quantum Electronics,* vol. 44, pp. 144-149, Jan-Feb 2008.

[116] M. Grupen and K. Hess, "Simulation of carrier transport and nonlinearities in quantum-well laser diodes," *IEEE Journal of Quantum Electronics,* vol. 34, pp. 120-140, 1998.

[117] D. Schroeder, *Modelling of interface carrier transport for device simulation*. Wien: Springer-Verlag, 1994.

[118] K. Kawano and T. Kitoh, *Introduction to optical waveguide analysis : solving Maxwell's equations and the Schrödinger equation*. New York: J. Wiley, 2001.

[119] M. Koshiba, *Optical waveguide theory by the finite element method*. Tokyo Dordrecht ; Boston: KTK Scientific; Kluwer Academic, 1992.

[120] M. M. Satter, H. J. Kim, Z. Lochner, J. H. Ryou, S. C. Shen, R. D. Dupuis, and P. D. Yoder, "Design and Analysis of 250-nm AlInN Laser Diodes on AlN Substrates Using Tapered Electron Blocking Layers," *Ieee Journal of Quantum Electronics,* vol. 48, pp. 703-711, May 2012.

[121] H. Hirayama, T. Yatabe, N. Noguchi, and N. Kamata, "Development of 230-270 nm AlGaN-Based Deep-UV LEDs," *Electronics and Communications in Japan,* vol. 93, pp. 24-33, Mar 2010.

[122] U. Schwarz, "Ultraviolet laser diodes - Indium-free success," *Nature Photonics,* vol. 2, pp. 521-522, Sep 2008.

[123] M. E. Levinshte**n, S. L. Rumyantsev, and M. Shur, *Properties of advanced semiconductor materials : GaN, AIN, InN, BN, SiC, SiGe*. New York ;: Chichester : John Wiley & Sons, 2001.

[124] W. H. Fan, S. M. Olaizola, T. Wang, P. J. Parbrook, J. P. R. Wells, D. J. Mowbray, M. S. Skolnick, and A. M. Fox, "Carrier capture times in InGaN/GaN multiple quantum wells," *physica status solidi (b),* vol. 240, pp. 364-367, 2003.

[125] H. Zhao, G. Liu, R. A. Arif, and N. Tansu, "Current injection efficiency induced efficiency-droop in InGaN quantum well light-emitting diodes," *Solid-State Electronics,* vol. 54, pp. 1119-1124, 2010.

[126] Y.-C. Lu, C.-Y. Chen, H.-C. Wang, C. C. Yang, and Y.-C. Cheng, "Carrier trapping effects on photoluminescence decay time in InGaN⁄GaN quantum wells with nanocluster structures," *Journal of Applied Physics,* vol. 101, p. 063511, 2007.

[127] U. Ozgur, H. O. Everitt, S. Keller, S. P. DenBaars, L. He, and H. Morkoc, "Ultrafast carrier relaxation in group III-nitride multiple quantum wells," *Ultrafast Phenomena in Semiconductors and Nanostructure Materials Viii,* vol. 5352, pp. 158-168, 2004.

[128] D. Holec, Y. C. Zhang, D. V. S. Rao, M. J. Kappers, C. McAleese, and C. J. Humphreys, "Equilibrium critical thickness for misfit dislocations in III-nitrides," *Journal of Applied Physics,* vol. 104, pp. -, Dec 15 2008.

[129] Z. M. Lochner, "Heterojunction bipolar transistors and ultraviolet-light-emitting diodes based in the III-nitride material system grown by metalorganic chemical vapor deposition," Ph.D., ECE, Georgia Institute of Technology, Atlanta, 2013.

[130] Y. C. Shen, G. O. Mueller, S. Watanabe, N. F. Gardner, A. Munkholm, and M. R. Krames, "Auger recombination in InGaN measured by photoluminescence," *Applied Physics Letters,* vol. 91, p. 141101, 2007.

[131] M. M. Satter, Z. Lochner, J. H. Ryou, S. C. Shen, R. D. Dupuis, and P. D. Yoder, "Polarization Matching in AlGaN-Based Multiple-Quantum-Well Deep Ultraviolet Laser Diodes on AlN Substrates Using Quaternary AlInGaN Barriers," *Journal of Lightwave Technology,* vol. 30, pp. 3017-3025, Sep 15 2012.

[132] L. S. McCarthy, P. Kozodoy, M. J. W. Rodwell, S. P. DenBaars, and U. K. Mishra, "AlGaN GaN heterojunction bipolar transistor," *Ieee Electron Device Letters,* vol. 20, pp. 277-279, Jun 1999.

[133] Y.-S. Liu, "Ultraviolet emitters grown by metalorganic chemical vapor deposition," MS, ECE, Georgia Institute of Technology, Atlanta, 2013.

[134] H. Tanaka, Y. Kawamura, and H. Asahi, "Room-temperature operation of MBE-grown InGaP/InGaAlP MQW visible laser diodes," *Electronics Letters,* vol. 22, p. 707, 1986.

[135] G. E. Dialynas, G. Deligeorgis, M. Zervos, and N. T. Pelekanos, "Influence of polarization field on the lasing properties of III-nitride quantum wells," *Physica E: Low-dimensional Systems and Nanostructures,* vol. 32, pp. 558-561, 2006.

[136] S. Mogg and J. Piprek, "Optimization of the barrier height in 1.3 mu m InGaAsP multiple-quantum-well active regions for high temperature operation," *Physics and Simulation of Optoelectronic Devices Ix,* vol. 4283, pp. 227-237, 2001.

[137] J. H. Davies, *The Physics of Low-dimensional Semiconductors: An Introduction*: Cambridge University Press, 1997.

[138] S. H. Ha, S. L. Ban, and J. Zhu, "Intersubband absorption in strained AlGaN/GaN double quantum wells," *Physica B: Condensed Matter,* vol. 406, pp. 3640-3645, 2011.

[139] M. A. Caro, S. Schulz, S. B. Healy, and E. P. O'Reilly, "Built-in field control in alloyed *c*-plane III-N quantum dots and wells," *Journal of Applied Physics,* vol. 109, p. 084110, 2011.

[140] M. M. Satter, Z. Lochner, J.-H. Ryou, S.-C. Shen, R. D. Dupuis, and P. D. Yoder, "AlGaN-Based Lateral Current Injection Laser Diodes Using Regrown Ohmic Contacts," *IEEE Photonics Technology Letters,* vol. 25, pp. 313-316, 2013.

[141] K. Oe, Y. Noguchi, and C. Caneau, "Gainasp Lateral Current Injection-Lasers on Semiinsulating Substrates," *Ieee Photonics Technology Letters,* vol. 6, pp. 479-481, Apr 1994.

[142] R. Quay, *Gallium nitride electronics*. Berlin: Springer, 2008.

[143] Y. N. Saripalli, L. Pei, T. Biggerstaff, S. Ramachandran, G. J. Duscher, M. A. L. Johnson, C. Zeng, K. Dandu, Y. Jin, and D. W. Barlage, "Transmission electron microscopy studies of regrown GaN Ohmic contacts on patterned substrates for metal oxide semiconductor field effect transistor applications," *Applied Physics Letters,* vol. 90, p. 204106, 2007.

[144] G. W. Li, R. H. Wang, J. Guo, J. Verma, Z. Y. Hu, Y. Z. Yue, F. Faria, Y. Cao, M. Kelly, T. Kosel, H. L. Xing, and D. Jena, "Ultrathin Body GaN-on-Insulator Quantum Well FETs With Regrown Ohmic Contacts," *Ieee Electron Device Letters,* vol. 33, pp. 661-663, May 2012.

[145] J. P. Liu, J. H. Ryou, D. Yoo, Y. Zhang, J. Limb, C. A. Horne, S. C. Shen, R. D. Dupuis, A. D. Hanser, E. A. Preble, and K. R. Evans, "III-nitride heterostructure field-effect transistors grown on semi-insulating GaN substrate without regrowth interface charge," *Applied Physics Letters,* vol. 92, p. 133513, 2008.

[146] S. M. Eichfeld, D. Won, K. Trumbull, M. Labella, X. Weng, J. Robinson, D. Snyder, J. M. Redwing, T. Paskova, K. Udwary, G. Mulholland, E. Preble, and K. R. Evans, "Dual temperature process for reduction in regrowth interfacial charge in AlGaN/GaN HEMTs grown on GaN substrates," *physica status solidi (c),* vol. 8, pp. 2053-2055, 2011.

[147] L. A. Coldren and S. W. Corzine, *Diode lasers and photonic integrated circuits*. New York ; Chichester: Wiley, 1995.

[148] F. Bertazzi, M. Goano, and E. Bellotti, "A numerical study of Auger recombination in bulk InGaN," *Applied Physics Letters,* vol. 97, p. 231118, 2010.

[149] N. N. Akram, "Lateral current injection (LCI) multiple quantum-well 1.55 mu m laser with improved gain uniformity across the active region," *Optical and Quantum Electronics,* vol. 36, pp. 827-846, Jul 2004.

[150] D. A. Suda, H. Lu, T. Makino, and J. M. Xu, "An Investigation of Lateral Current Injection-Laser Internal Operation Mechanisms," *Ieee Photonics Technology Letters,* vol. 7, pp. 1122-1124, Oct 1995.

[151] E. H. Sargent, D. A. Suda, A. Margittai, F. R. Shepherd, M. Cleroux, G. Knight, N. Puetz, T. Makino, A. J. SpringThorpe, G. Chik, and J. M. Xu, "Experimental study of LCI lasers fabricated by single MOCVD overgrowth followed by

selective dopant diffusion," *Ieee Photonics Technology Letters,* vol. 10, pp. 1536-1538, Nov 1998.

[152] T. Okumura, M. Kurokawa, M. Shirao, D. Kondo, H. Ito, N. Nishiyama, T. Maruyama, and S. Arai, "Lateral current injection GaInAsP/InP laser on semi-insulating substrate for membrane-based photonic circuits," *Optics Express,* vol. 17, pp. 12564-12570, Jul 20 2009.

[153] T. Okumura, H. Ito, D. Kondo, N. Nishiyama, and S. Arai, "Continuous Wave Operation of Thin Film Lateral Current Injection Lasers Grown on Semi-Insulating InP Substrate," *Japanese Journal of Applied Physics,* vol. 49, p. 040205, 2010.

[154] T. Okumura, M. Kurokawa, D. Kondo, H. Ito, N. Nishiyama, and S. Arai, "Lateral Current Injection Type GaInAsP/InP DFB Lasers on SI-InP Substrate," *2009 Ieee 21st International Conference on Indium Phosphide & Related Materials (Iprm),* pp. 178-181, 2009.

[155] M. M. Satter, Z. Lochner, T.-T. Kao, Y.-S. Liu, X.-H. Li, S.-C. Shen, R. D. Dupuis, and P. D. Yoder, "AlGaN-Based Vertical Injection Laser Diodes Using Inverse Tapered p-Waveguide for Efficient Hole Transport," *IEEE Journal of Quantum Electronics,* vol. 50, pp. 166-173, 2014.

[156] S.-N. Lee, J. Son, T. Sakong, W. Lee, H. Paek, E. Yoon, J. Kim, Y.-H. Cho, O. Nam, and Y. Park, "Investigation of optical and electrical properties of Mg-doped p-InxGa1−xN, p-GaN and p-AlyGa1−yN grown by MOCVD," *Journal of Crystal Growth,* vol. 272, pp. 455-459, 2004.

[157] K. B. Nam, M. L. Nakarmi, J. Li, J. Y. Lin, and H. X. Jiang, "Mg acceptor level in AlN probed by deep ultraviolet photoluminescence," *Applied Physics Letters,* vol. 83, p. 878, 2003.

[158] K. Kumakura, T. Makimoto, and N. Kobayashi, "Mg-acceptor activation mechanism and transport characteristics in p-type InGaN grown by metalorganic vapor phase epitaxy," *Journal of Applied Physics,* vol. 93, p. 3370, 2003.

[159] T. Katsuno, Y. Liu, D. Li, H. Miyake, K. Hiramatsu, T. Shibata, and M. Tanaka, "n-type conductivity control of AlGaN with high Al mole fraction," *physica status solidi (c),* vol. 3, pp. 1435-1438, 2006.

[160] B. Cheng, S. Choi, J. E. Northrup, Z. Yang, C. Knollenberg, M. Teepe, T. Wunderer, C. L. Chua, and N. M. Johnson, "Enhanced vertical and lateral hole transport in high aluminum-containing AlGaN for deep ultraviolet light emitters," *Applied Physics Letters,* vol. 102, p. 231106, 2013.

[161] K. Kim, J. Choi, S. C. Jeon, J. S. Kim, and H. M. Lee, "Photonic crystal effect on light emission from InGaN/GaN multi-quantum-well structures," *Applied Physics Letters,* vol. 90, p. 181115, 2007.

[162] S. P. DenBaars, D. Feezell, K. Kelchner, S. Pimputkar, C.-C. Pan, C.-C. Yen, S. Tanaka, Y. Zhao, N. Pfaff, R. Farrell, M. Iza, S. Keller, U. Mishra, J. S. Speck, and S. Nakamura, "Development of gallium-nitride-based light-emitting diodes (LEDs) and laser diodes for energy-efficient lighting and displays," *Acta Materialia,* vol. 61, pp. 945-951, 2013.

[163] H. X. Jiang and J. Y. Lin, "Hexagonal boron nitride for deep ultraviolet photonic devices," *Semiconductor Science and Technology,* vol. 29, p. 084003, 2014.

VITA

MD. MAHBUB SATTER

Md. Mahbub Satter received his B.Sc. and M.Sc. degrees in Electrical and Electronic Engineering from the Bangladesh University of Engineering and Technology (BUET) in 2005 and 2008, respectively. He additionally served as a Lecturer for the Department of Electrical and Electronic Engineering, BUET between 2005 and 2009. He is currently working toward his Ph.D. degree at the Georgia Institute of Technology in the area of semiconductor photonic devices under the guidance of Professor Douglas Yoder. Recently, he completed an eleven month curricular practical training as a graduate technical intern in the Silicon Photonics Solutions Group (SPSG) at Intel Corporation, Santa Clara, California.